Investigations of phonon-drag phenomena in low-dimensional electron structures

Kershaw, Yvonne

Award date:
1996

Awarding institution:
University of Bath

Investigations of phonon-drag phenomena in low-dimensional electron structures

Submitted by Yvonne Kershaw
for the degree of Ph.D
of the University of Bath
1996

ProQuest LLC
789 East Eisenhower Parkway
P.O. Box 1346
Ann Arbor, MI 48106-1346

Abstract

The electron-phonon interaction in low-dimensional electron systems has been investigated using the phonon-drag effect. This effect makes use of the fact that when a phonon interacts with an electron, a transfer of momentum occurs, causing the electron to move in the direction of motion of the phonon. An electric field opposing the electron motion is then set up, which can be measured as an external voltage. Two types of samples were used for these experiments: two-dimensional electron gases (2DEGs) formed at the interface of GaAs/AlGaAs modulation-doped heterostructures; and three-dimensional electron gases (3DEGs) formed by epitaxial growth of a 2μm thick silicon-doped GaAs layer on the semi-insulating substrate. Both types of sample are shown to give qualitatively the same results.

Spatially resolved phonon-drag measurements show features due to the phonon focussing within the samples, and also new features attributed to the finite detector geometry. Theoretical modelling of the phonon-drag effect, by equating it to the setting up of a local charge dipole and solving the 2D Poisson equation over the whole sample geometry has been performed. Comparison of the theoretical results with the experimentally obtained images shows excellent agreement, proving the strength of the model in describing the experimental situation.

Frequency resolved measurements using superconducting tunnel junctions as generators of quasi-monochromatic acoustic phonons have also

been performed. The results of these measurements were subject to some discussion, since they appear not to be consistent with theoretical expectations, and these points will be discussed.

Contents

Chapter 1

Introduction

The electron-phonon interaction in semiconductors has long been an area of intense experimental and theoretical study due to its importance in determining a number of macroscopic properties, such as electrical and thermal conductivity. Recently, the development of low dimensional electronic devices has led to the interest being concentrated on the interaction of phonons with electrons confined to a two (or lower) dimensional layer. The rapid growth in the semiconductor industry has stimulated a large amount of research into the properties of gallium arsenide (GaAs). Gallium arsenide has two main advantages over silicon: i) it has a *direct* band gap of $1.4eV$ at 300 K, which makes it more suited for optoelectronic applications, and ii) devices can be made with higher electron mobilities than found in silicon devices (low temperature mobilities in GaAs structures have reached values of $> 1 \times 10^7 cm^2/Vs$,

whereas mobilities in silicon have a maximum of about $50000 cm^2/Vs$). These factors mean that GaAs is very important for high frequency applications, especially for frequencies above 1 GHz, for example as HEMTs (High Electron Mobility Transistors) as amplifiers in satellite receivers. The optical properties are exploited, for example, in laser diodes in CD players.

A large amount of the research work has focussed on the study of low-dimensional electron systems. If electrons are confined in their motion in one direction, and therefore only free to move in a plane, the system is referred to as a two-dimensional electron gas (2DEG). If further degrees of freedom are restricted, then a one-dimensional electron gas (1DEG) or a zero-dimensional electron system (0DES) respectively, will be formed. Although the electrical properties of these materials and devices are well known, the electron-phonon interaction is not so well understood, or so extensively researched, even though this has important consequences for the dynamic and thermal properties of the semiconductor. Due to the constant miniaturisation of semiconductor devices, the energy dissipated per unit volume increases, which can only be removed by vibrations of the crystal lattice, i.e. by the emission of various types of phonons. A detailed knowledge of the transport properties of phonons in semiconductors is therefore necessary for future technological developments. It is also interesting to investigate the interaction of three-dimensional phonons with electrons which are confined in their motion to two or less dimensions.

For a long time, the only method of studying phonons with frequencies above 10 GHz was through measurements of thermal conduction (for example, see Eisenstein et.al. [1]). This method averages over all the phonon frequencies and wave vectors and does not allow any 'spectroscopy', in contrast to the analogous techniques available in optics. The first step beyond this limitation was made by von Gutfeld and Nethercot [2], who generated phonons using a short heat pulse, and detected the ballistic phonons on the other side of the sample with a superconducting bolometer. Using such a bolometer, with response times $\sim 40ns$, and a box-car gate to separate out the temporal signals, they could study the signal as a function of time. Using this 'time-of-flight' spectroscopy they could identify the different phonon modes, since they have different velocities and therefore arrive at different times. The requirements for these experiments are very pure, defect-free samples and low temperatures, in order that the phonon scattering remains low: i.e. the mean free path of the phonons must be larger than the sample dimensions.

The next advance was made by Eisenmenger and Dayem [3], who used superconducting tin tunnel junctions as phonon detectors and generators. Here they were able to show that ballistic transport of high frequency phonons ($\geq$ 200 GHz) over macroscopic distances ($\sim$ 1cm) is possible. Most relevant to the work presented in this thesis was the discovery by Taylor, Maris and Elbaum [4] that the relative amplitude of the measured phonon pulse has a large dependence on the direction

of propagation. This 'phonon focussing' phenomenon can be explained by considering the anisotropy of the crystal. Hensel and Dynes [5] generated phonons using a laser beam focussed onto a metal film, and this same technique was employed by Northrop and Wolfe [6], who used the focussed laser beam as a movable phonon generator, and developed techniques to map the two dimensional phonon focussing images by scanning the laser beam across the sample. This scanning technique is applied to a large extent within this work. Another very nice example of a direct demonstration of phonon focussing was shown in an experiment by Eisenmenger [7], in which the surface of a silicon crystal was covered with a film of superfluid helium. The areas of the film where phonons are incident increase in thickness due to the fountain pressure, and this increase in film thickness can be observed and photographed under oblique illumination. Focussing of dispersive phonons (i.e. high frequency phonons, where the frequency is no longer linearly dependent on the magnitude of the wave-vector) was first observed by Dietsche, Northrop and Wolfe [8].

Two-dimensional electron gases (2DEGs) were first used as detectors in phonon-drag experiments by Karl et.al. [9]. In these experiments a 2DEG was situated on one side of the sample, and an aluminium film on the other. The aluminium film was illuminated with a laser beam, which was raster scanned across the whole sample surface, thereby creating phonons which traversed the sample, before interacting with the 2DEG. This interaction leads to the exchange of momentum and en-

ergy: the transfer of energy causes a temperature rise in the 2DEG, whereas the transfer of momentum drags the electrons in the direction of the incoming phonons. This is known as the phonon-drag effect, and leads to the setting up of a voltage, known as the phonon-drag voltage. This voltage can then be measured as a function of laser position to give spatially resolved images of phonon-drag focussing patterns. Essential to these experiments was a 2DEG detector which could be assumed to be a point detector, otherwise spatial resolution cannot be achieved. For this reason the 2DEG was patterned into a structure consisting of a small bridge between two contact areas. It will be shown that such a structure cannot be assumed to be a point detector, and that the geometry of the detector plays a very important role in these phonon-drag imaging experiments.

A further extension of the phonon-drag work was carried out by Lega et.al. [10] who used superconducting tunnel junctions as sources of quasi-monochromatic phonons. In contrast to the measurements of [9], the measurements of [10] provide little spatial resolution, but are instead frequency dependent measurements. These then provide detailed information about the electronic properties of the 2DEG and its interaction with the phonons.

In the work described in this thesis, the technique used by Karl et.al. [9] is applied extensively, and in addition to the results obtained previously, some novel results were obtained where the geometry of the entire sample is seen to play a very important role. In order to explain

these new results a theoretical model was developed, which takes into account the finite geometry of the sample, and which explains the new results with remarkable accuracy, for a number of different sample geometries.

In the next chapter of this thesis an introduction is given to the background theory of 2DEGs and phonons. Since the 2DEG is basically used as a detector in this work, the theory of the 2DEG will be kept to a minimum, with the accent being on any features of the 2DEG which will affect the phonon propagation and detection. The section on phonon theory will discuss the scattering of phonons, ballistic transport and the factors that give rise to phonon focussing. A section on phonon generation by laser excitation of a superconducting metal film, or by the use of superconducting tunnel junctions, and a discussion of the phonon spectra thus obtained will also be included. The electron-phonon interaction will be dealt with in more detail by considering the matrix element of the interaction, the different types of coupling due to the piezoelectric interaction and the deformation potential, and the effects of conservation of both energy and momentum. The restrictions on the electron-phonon interaction due to the the $2k_F$ cut-off and the form factor will also be discussed. In addition, the theory of the phonon-drag effect will be outlined. In chapter 3, a theoretical model is developed to describe the phonon-drag imaging results. In this model the phonon-drag effect is approximated by a local charge dipole, which is solved over the total sample geometry. Chapter 4 will present some

of the experimental details, including the sample preparation.

In chapter 5 the spatially resolved imaging experiments are described and the novel phonon-drag images that were obtained are presented. Included in this chapter are also some experimental results obtained from phonon-drag measurements on a three-dimensional electron layer, which show qualitatively the same effects as the results on 2DEGs. The phonon-drag images described in these sections show some features which were not seen in [9], which are assumed to be due to the detector (2DEG/3DEG) geometry. The lack of the theoretically predicted frequency dependence in the images, and the possible reasons for this will also be discussed. Chapter 6 describes the frequency resolved measurements, based on the experiments of [10] which use superconducting tunnel junctions as generators of monochromatic acoustic phonons. A description and discussion of the results obtained from these measurements will also be given.

Chapter 7 presents the main part of this work, where the theoretical results obtained from the simulation of the phonon-drag images are shown, along with a discussion of their agreement with the relevant experimental images. Some new experimental images will also be presented, which serve to show the extent to which the theory is capable of describing the experimental situation. Chapter 8 gives a summary of the work included in this thesis. In Appendix A, more detailed information about the simulations performed will be presented, and in Appendix B, a short description of the use of normal state tunnel junc-

tions as generators of quasi-monochromatic phonons will be given.

This work has led to the much more complete understanding of some experiments which were performed for the first time in 1988. It would be possible to extend this work by using other materials as detectors, for example hole gases, where the measured signal should be larger, since the hole-phonon interaction is stronger than the electron-phonon interaction. However, since the bulk of the sample is the same, it would not be expected that different focussing structures could be seen, unless the holes interact more or less strongly with a specific phonon mode. The experimental and theoretical analysis presented here gives a complete description of the phonon-drag images when using 2DEG/3DEGs as detectors, and could easily be applied to the explanation of other images obtained using, for example, hole gases as detectors. This work also shows that phonon-drag images can be very complicated, depending on the geometry of the detector, and that it is not sufficient just to consider the detector to be a point, but rather that by taking the detector geometry into account even the most complicated images can be explained.

Chapter 2

Theoretical Background

In this section, a basic introduction to the theory of low-dimensional electron systems will be given. In the experiments that follow, the 2DEG is used as a detector, and for this reason, the description of the 2DEG will be restricted to those properties which influence the measurements performed. A more complete description of the electronic properties of 2DEGs can be found in [11]. After a description of the 2DEG, the properties of phonons will be discussed, which will include a section on phonon scattering within the crystal, anisotropic phonon transport and phonon focussing, and interface effects. Phonon generation by laser excitation of a superconducting film, as well as from superconducting tunnel junctions, and the phonon spectra thus generated will also be addressed. This is followed by a section on the electron-phonon interaction which will discuss the absorption probability of phonons, and the

features which dominate the absorption (the form factor and the $2k_F$ cut-off). The deformation potential and the piezoelectric interaction will be described, including a discussion of their relative importance in the electron-phonon interaction. The chapter ends with a description of the phonon-drag effect, the phenomenon that is used extensively in the measurements presented here.

2.1 Properties of GaAs and $Al_xGa_{(1-x)}As$

GaAs is a III/V semiconductor, with zinc-blende structure and a direct energy gap. When Al is added into the ternary alloy $Al_xGa_{(1-x)}As$, the energy gap increases from a value of $\sim$ 1.4eV for zero Al content ($x = 0$), to $\sim$ 2.2eV for $x = 1$. The two materials (GaAs and $Al_xGa_{(1-x)}As$) are brought together and a heterojunction is formed. In this system, where the wide-gap material ($Al_xGa_{(1-x)}As$) is selectively n-doped, and the narrow gap material (GaAs) is essentially free of impurities, electrons from the donor levels of $Al_xGa_{(1-x)}As$ are transferred to the GaAs layer (under equilibrium conditions) in order to create a uniform Fermi energy throughout the sample. In the case of GaAs/$Al_xGa_{(1-x)}As$, the GaAs conduction band at the interface lies below the Fermi level, and an inversion layer is formed, as can be seen in Figure 2.1.1. This leads to confinement of the electrons in the GaAs layer at the interface, and produces a two dimensional electron gas (2DEG). Such structures (where the donor

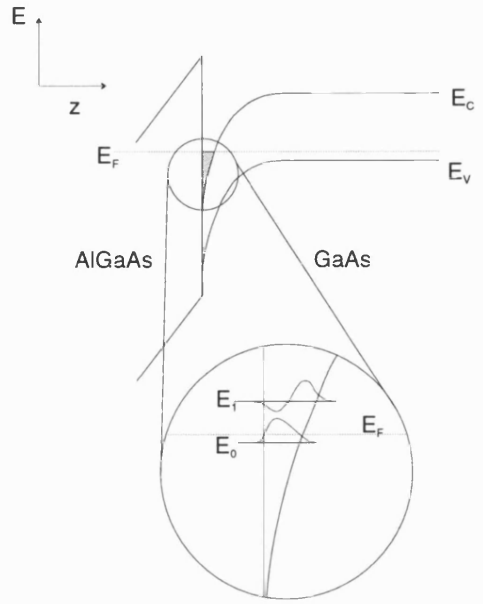

Figure 2.1.1: *Energy band diagram of the $GaAs/Al_xGa_{(1-x)}As$ heterostructure, showing the existence of an inversion layer, which is shown in more detail, with the subbands labelled, in the inset.*

electrons are spatially separated from their parent impurity atoms) are called modulation-doped heterostructures [12]. This spatial separation and the inclusion of a thin undoped spacer layer of $Al_xGa_{(1-x)}As$, leads to a large reduction in the impurity scattering and hence to very high mobilities ($> 10^7 cm^2 V^{-1} s^{-1}$ at 0.3K, [13]). In the next section a more theoretical description of the 2DEG is given.

2.2 The 2DEG

The term 2DEG is used to describe systems where the electron gas is confined to a very thin layer. The co-ordinates are chosen so that the electron system lies in the $x-y$ plane. An effective potential V, which depends only on z, leads to the confinement of the electrons in the layer. The eigenstates of the electrons can be obtained from the wave-function

$$\Psi_{i,k_{||}}(x,y,z) = e^{i\vec{k}_{||}\vec{r}_{||}}\Phi_i(z)\frac{1}{\sqrt{L_xL_y}} \tag{2.2.1}$$

where $\vec{r}_{||}$ and $\vec{k}_{||}$ are vectors in the $x-y$ plane of real space and k-space respectively. $\Phi_i(z)$ is the subband wave-function with the subband index i, and L_xL_y gives the extent of the 2DEG in the $x-y$ plane. The energy eigenvalues are given by

$$E(i,k_{||}) = E_i + \frac{\hbar^2k_{||}^2}{2m^*} \tag{2.2.2}$$

where E_i is the subband energy and m^* is the conduction band electronic mass. In GaAs this has a value of about 6.7% of the mass of a free electron. The density of states (DOS) is constant for each subband (if m^* is constant) and is given by

$$D(E) = \theta(E-E_i)\frac{m^*}{\pi\hbar^2} \tag{2.2.3}$$

as shown in Figure 2.2.1. The term θ is the Heavyside step function. At T= 0K, with only one subband occupied, all states up to the Fermi

energy are filled, and the Fermi energy is given by

$$E_F = E_0 + N_e \frac{\pi \hbar^2}{m^*} \tag{2.2.4}$$

where N_e is the carrier concentration per unit area. In two dimensions the Fermi surface is a circle of radius k_F (the Fermi wave vector) where

$$k_F = (2\pi N_e)^{1/2}. \tag{2.2.5}$$

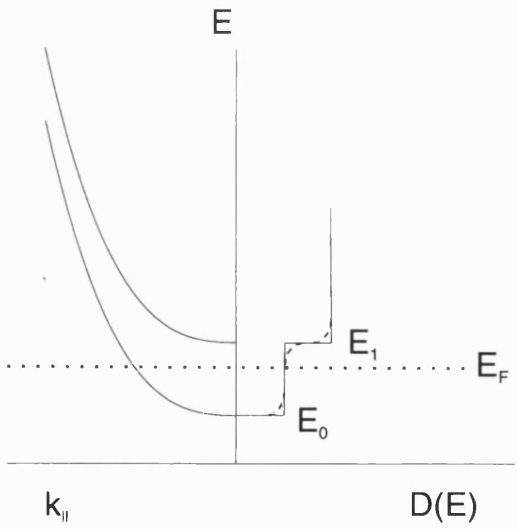

Figure 2.2.1: *Schematic diagram showing two lowest subbands, and the corresponding density of states. On the right side (the density of states) the solid line shows the ideal situation ($T = 0K$), whereas the dashed line shows the real case with lifetime broadening.*

2.3 Phonon theory

Phonons are the quantised vibrations of the crystal lattice. For every wave vector in q-space there are $3p$ normal phonon modes, where p is the number of atoms in the crystal basis. Three of the $3p$ branches are acoustic; i.e. they describe lattice vibrations with frequencies which vanish linearly with q in the long-wavelength limit. The other $3(p-1)$ branches are optical; i.e. their frequencies do not vanish in the long-wavelength limit. The dispersion curves for the phonon modes in GaAs are shown in Figure 2.3.1, obtained from neutron scattering measurements [14]. This work will concentrate only on the acoustic modes. It can be seen that for the acoustic branches, close to the Γ point, there is a linear relationship between the frequency and the wave vector. For frequencies larger than 1THz, the acoustic branches then flatten out towards the zone edge. This leads to a reduction of the group velocity of the acoustic branches towards the zone edge. The acoustic phonon modes are described by the terms longitudinal (LA) and transverse (TA) acoustic phonons; longitudinal modes oscillate parallel to their direction of propagation, whereas transverse modes oscillate perpendicular to their propagation direction. There are also two types of transverse modes: slow transverse (STA) and fast transverse (FTA) which differ from each other by their group velocities.

In most phonon experiments, the phonons must travel across the crystal substrate between source and detector. Therefore in assessing

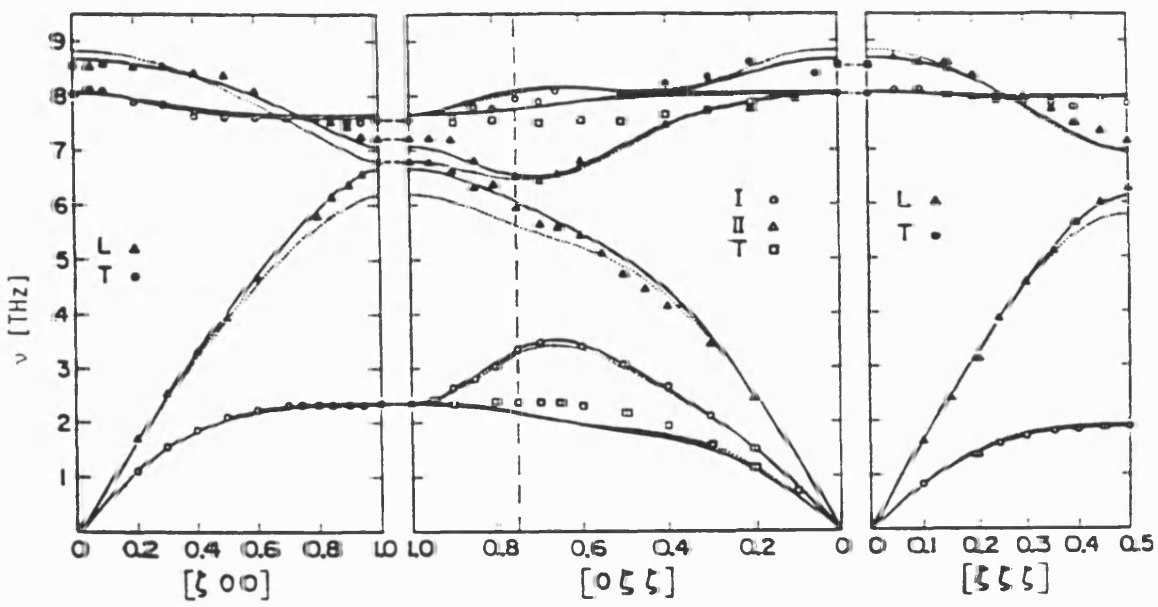

Figure 2.3.1: *Phonon dispersion relations for GaAs for different crystallographic directions.*

the data, intrinsic substrate effects must be considered. The most important such effects are isotope scattering, anharmonic decay, phonon focussing, and interface effects.

2.3.1 Scattering of phonons

Whether phonons are able to travel ballistically through the crystal or not depends on their mean free path. If this is large compared to the dimensions of the crystal then the phonon transport will be ballistic; if

not, the phonons will undergo scattering. The most important scattering mechanisms for acoustic phonons in GaAs at low temperatures are elastic isotope scattering, and inelastic anharmonic decay.

Isotope scattering

If an element of the crystal possesses different isotopes, the perfect periodicity of the crystal lattice is disrupted. This leads to scattering of the phonons at the local mass variations within the crystal, which increases as the fourth power of the phonon frequency. The scattering rate for a given phonon frequency is proportional to the variation in the mass of the isotopes, and is given by

$$(\tau^{is})^{-1} \propto \sum_i D(i)\left(\frac{\delta m_i}{\bar{m}}\right)^2 \tag{2.3.1}$$

where $D(i)$ is the relative amount of the isotope i, $\bar{m}$ is the mean mass of the element and δm_i is the deviation of the mass of i from this value. In GaAs, As is isotopically pure but Ga has two isotopes, ^{69}Ga and ^{71}Ga, and these are responsible for the isotope scattering in GaAs. Tamura [15] calculated the scattering rate in GaAs for the long wavelength acoustic limit to be

$$(\tau^{is})^{-1} = 7.38 \times 10^{-42}\nu^4 sec^3 \tag{2.3.2}$$

i.e. for 1THz phonons this gives a scattering rate in GaAs due to isotope scattering of $(\tau^{is})^{-1} = 7.38 \times 10^6 s^{-1}$. Isotope scattering is an elastic

scattering process, which reduces the mean free path of the phonons but does not alter their energy spectrum.

Anharmonic decay

Since the lattice potential is not perfectly harmonic, it is also possible for phonons to decay, under the conservation of energy and momentum. Tamura [16] has shown that the dominant decay process is that of a LA phonon decaying into two TA phonons, and he gives the decay rate, for GaAs, to be

$$(\tau^{ah})^{-1} = (0.77...1.35) \times 10^{-54} \nu^5 sec^4 \qquad (2.3.3)$$

depending on the values of the elastic constants used. For 1THz phonons this then gives decay rates of between $0.77 \times 10^6 s^{-1}$ and $1.35 \times 10^6 s^{-1}$. From equations (2.3.2) and (2.3.3) it can be seen that for frequencies of 1THz, the dominant scattering process is isotope scattering. However, because of the higher power dependence of the anharmonic decay on frequency, at higher frequencies ($\geq$ 6THz) the latter will dominate over isotope scattering. Anharmonic decay processes will obviously alter the frequency spectrum of the phonons, as opposed to isotope scattering. Taking the scattering rate in GaAs for 1THz phonons to be $7.38 \times 10^6 s^{-1}$ this gives a phonon mean free path of $\sim 0.4mm$. This value is larger than the sample thickness used in these experiments, therefore it can be assumed that the phonons travel ballistically between generator and detector.

2.3.2 Anisotropic phonon transport

In real crystals the elastic properties are direction dependent, a fact which has important consequences for phonon transport. In general, the phonon group velocity $\vec{v}_g$ and the q-vector are not co-linear, which results in a channeling or 'focussing' of phonon energy along certain preferred crystal directions [4].

To understand focussing in detail it is easiest to start with a detailed description of elastic wave motion in an anisotropic medium. In the long-wavelength or continuum approximation (where the phonon wavelength is large compared to the inter-atomic spacing) the stress and strain fields associated with a phonon are represented by second rank tensors. At small strains the two are related by the generalised Hooke's law, as

$$T_{i,j} = C_{i,j,l,m} S_{l,m}. \tag{2.3.4}$$

$T_{i,j}$ is the stress tensor, $S_{l,m}$ is the strain tensor, $C_{i,j,l,m}$ is the fourth rank elastic tensor of the crystal material and each index represents a cartesian axis. Summation over repeated indices is assumed. The strain tensor is described in terms of the displacement $\vec{u}$ of an elemental volume $dx_1 dx_2 dx_3$ from its equilibrium position:

$$S_{i,j} = \frac{1}{2}\left(\frac{\partial u_i}{\partial x_j} + \frac{\partial u_j}{\delta x_i}\right). \tag{2.3.5}$$

The equation of motion is then

$$\rho \ddot{u}_i = \frac{\partial T_{ij}}{\partial x_j} = C_{i,j,l,m} \frac{\partial^2 u_l}{\partial x_m \partial x_j} \tag{2.3.6}$$

where ρ is the material density. Equation 2.3.6 has the wave solution $\vec{u} = \vec{\epsilon}e^{i(\vec{q}.\vec{r}-\omega t)}$ (where $\vec{\epsilon}$ is the polarisation vector and ω is the angular frequency), which upon substitution, yields a set of linear equations,

$$(C_{i,j,l,m}q_j q_m - \rho\omega^2\delta_{il})\epsilon_l = 0. \tag{2.3.7}$$

Defining the wave normal $\vec{n} = \vec{q}/|\vec{q}|$ and phase velocity $v = \omega/|\vec{q}|$ this becomes

$$(D_{il} - v^2\delta_{il})\epsilon_l = 0 \tag{2.3.8}$$

where $(D_{il} = (1/\rho)(C_{i,j,l,m}n_j n_m)$ is the Christoffel tensor [17]. Since D_{il} is independent of $|\vec{q}|$ the phase velocity is a function of direction only and for a given wave vector $\vec{q} = (q, \theta_q, \phi_q)$ the angular frequency is

$$\omega = v(\theta_q, \phi_q)q. \tag{2.3.9}$$

Setting the determinant of equation (2.3.8) to zero yields a cubic expression in v^2 with three roots corresponding to the three possible phonon modes (one longitudinal and two transverse). For each root, v_s, there is a polarisation vector $\vec{\epsilon}_s$, where $s = 0, 1, 2$ and defines the LA, ST and FT modes respectively. For a given $\vec{q}$ vector, the three polarisation vectors will be mutually orthogonal, however in general none will be either parallel or perpendicular to $\vec{q}$.

The associated energy flux is parallel to the group velocity which can be obtained by vector differentiation of equation (2.3.8), as

$$\vec{v}_g = \frac{\partial\omega}{\partial\vec{q}}. \tag{2.3.10}$$

The most revealing way of plotting these results is as a constant frequency surface in k-space, see Figure 2.3.2a. Such a plot is known as a

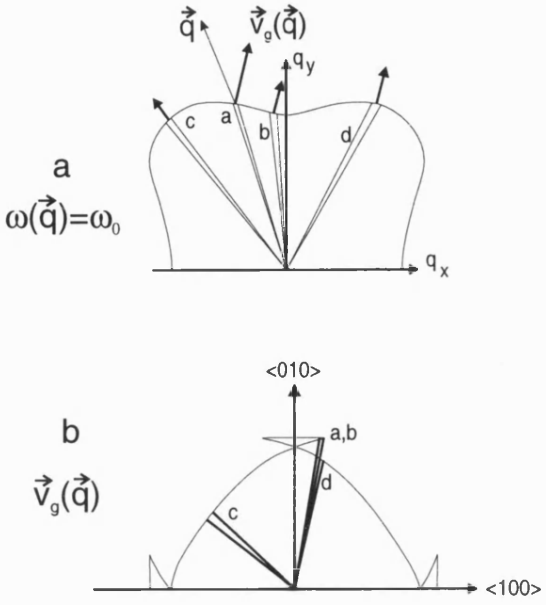

Figure 2.3.2: *(a) Surfaces of constant energy for GaAs. It can be seen that $\vec{q}$ and $\vec{v}_g(\vec{q})$ are not necessarily parallel. (b) The respective group velocity vectors in real space showing the directions of preferred energy flux.*

slowness surface since its radius is inversely proportional to the phase velocity. It can be seen that the group velocity is perpendicular to the slowness surface, and that this gives rise to directions in the crystal with a channeling of phonon energy, which is known as phonon focussing. This should not be thought of as being equivalent to focussing as is known from optics, since the phonons are not focussed, but rather they experience a 'bunching' in certain crystallographic directions, leading to

a larger phonon flux in some directions than in others. This can be seen more clearly in Fig. 2.3.2b, where the group velocity vectors are shown in real space. It is easy to see that when the curvature of the slowness surface is slight, states within a large angle propagate in virtually the same direction in real space. It can be shown that at regions of zero curvature (inflexion points) there is an infinite (but integrable) phonon flux, and similarly, regions with large curvature produce small phonon flux. It can also be seen that the state given by (d) propagates in the same direction as (a) and (b), but with a lower velocity: i.e. a given group velocity vector direction may correspond to more than one $\vec{q}$ vector. It is also to be remembered that pure transverse or longitudinal phonon modes only occur in isotropic crystals: in the general case the phonon modes will possess parts of both polarisations.

Using the elastic constants and the density of the crystal it is possible to calculate the position-dependent energy flux incident on the detector side of the crystal, which is given by

$$e(\vec{r}_{||}) = \sum I(\vec{r}_{||}, q, s)\hbar\omega(q, s) \qquad (2.3.11)$$

where $\vec{r}_{||}$ is the two dimensional position vector on the detector side of the sample and s is the phonon mode. $I(\vec{r}_{||}, q, s)$ gives the position dependent phonon flux for a given mode s and state q. Fig 2.3.3 shows the calculated energy flux through the (100) plane of a GaAs crystal. The diagonals give the position of the (010) and the (001) axes. A square structure in the centre of the image (around the $\langle 100 \rangle$ axis)

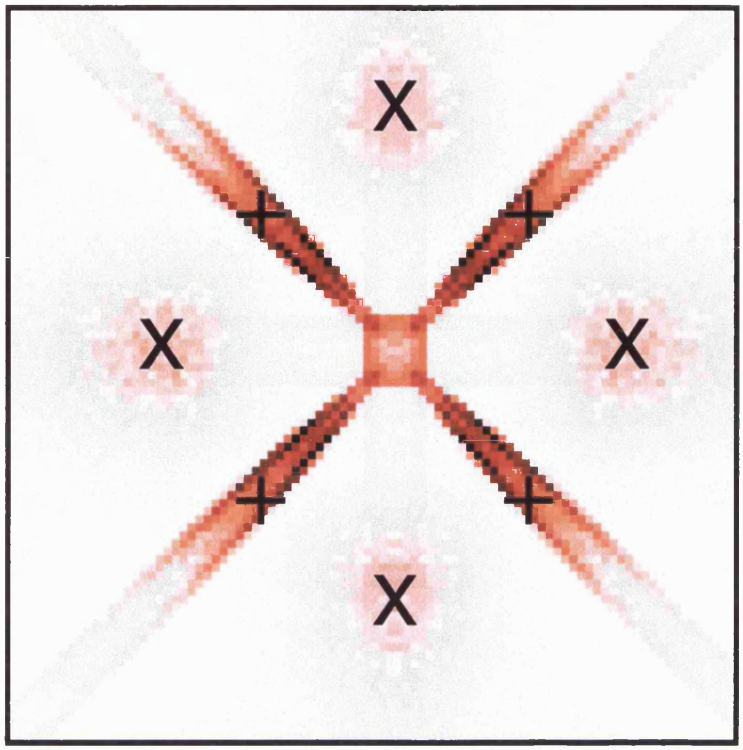

Figure 2.3.3: *Energy focussing image for the (100) surface in GaAs: the* $\langle 111 \rangle$ *points are depicted by X, the* $\langle 100 \rangle$ *points by +.*

opposite the phonon source is clearly visible, which is due to the STA phonons. The weak stripes emanating from the centre towards the $\langle 111 \rangle$ points (marked by X) are also due to the STA phonons, whereas the stripes along the diagonals are due to the FTA phonons. The signal at the points marked with X is due to the focussing of longitudinal (LA) phonons.

The momentum flux that reaches the detector is also largely depen-

dent on direction and is given by

$$\vec{P}(\vec{r}_{||}) = \sum_{q,s} I(\vec{r}_{||}, q, s)\hbar\vec{q}. \tag{2.3.12}$$

The result of the calculation of the momentum flux is shown in Fig. 2.3.4. Here it can be seen that the strong focussing signal that was in the

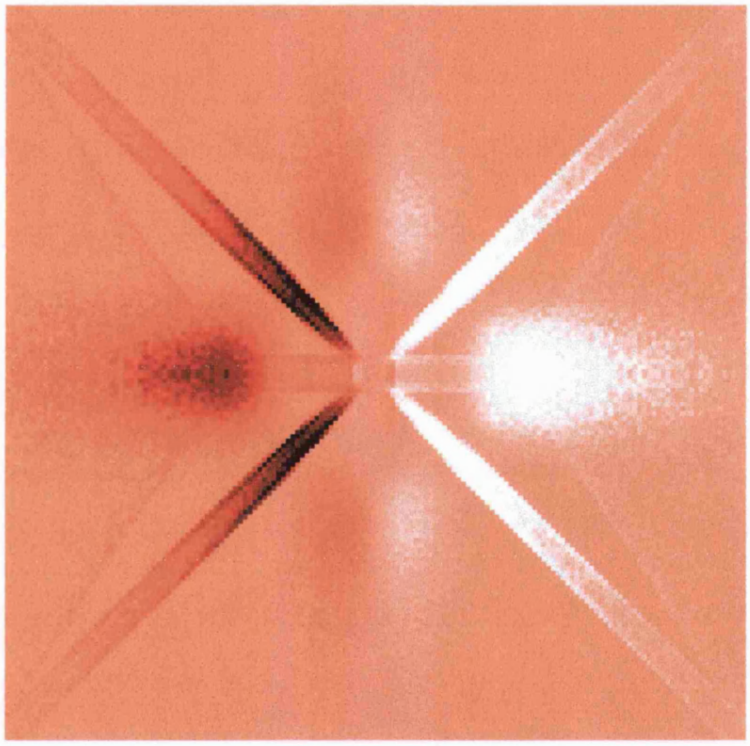

Figure 2.3.4: *Quasi-momentum focussing image for the* (100) *surface in GaAs: bright and dark regions depict areas of large positive and negative signals respectively.*

centre of Fig. 2.3.3 is reduced in this image. The reason for this is that in the momentum focussing patterns only the components of momentum

parallel to the $x - y$ plane are important, and this component is very small for phonons arriving with a small angle of incidence. In this work, the detectors used (2DEGs/3DEGs) are sensitive to this momentum flux [9].

Interface effects

The final point to be considered is that in the experiments presented here the phonons are generated in a metal film (either a thin aluminium film, or a superconducting tunnel junction). This means that before the phonons enter the substrate they have to be transmitted through the metal-substrate interface, and this will affect their propagation. It is to be expected that the interface between the metal and the substrate is not ideal; the films are evaporated in high vacuum, and not ultra-high vacuum, and although the samples undergo an external cleaning process, followed by a short in-situ cleaning process within the vacuum chamber this will not be sufficient to ensure that the surface is free from all contamination. The other point to remember is that the surface will not be atomically flat. A lot of research work has been done in the area of interface and surface phonons, ranging from studies of the Kapitza effect [18] (where the experimentally found transmission coefficient between the crystal surface and liquid helium is found to be much larger than would be predicted from acoustic mismatch theory

[19]) to studies of phonon transmission across different interfaces[1]. The Kapitza effect is thought to be largely influenced by the quality of the surface, with atomically flat surfaces showing the expected transmission coefficients [21]. It has also been shown [22] that the transmission of phonons across an interface is not isotropic, but the phonon transmission is instead peaked along certain wave-vector directions. However, these latter effects are only to be seen for very smooth interfaces, and are therefore not to be expected here, where the substrates undergo no special preparation procedure. The effect of the roughened surface present in our samples will be to slightly reduce the intensity of the ballistic phonons, to increase the number of diffuse phonons, to reduce the sharpness of the focussing structures, and to possibly cause a certain amount of down-conversion of high-frequency phonons.

2.4 Phonon generation

There are numerous methods of generating acoustic phonons, and in this work two methods are used: laser excitation of a superconducting film producing a Planckian spectrum peaked around the temperature of the excited film, and superconducting tunnel junctions producing quasi-monochromatic acoustic phonons with energies of $eV_o - 2\Delta$, where V_o

[1] At interfaces between metal films and crystals, the experimentally found transmission is much less than that expected from mismatch theory [20].

is the bias voltage across the junction, and 2Δ is the energy gap of the superconductor.

2.4.1 Laser excitation of a superconducting film

In some of the experiments presented here, a laser beam is focussed onto an aluminium film, thereby locally heating the film. It is this local heating effect that creates the non-equilibrium phonons used in the experiments. The phonons produced have a Planckian frequency spectrum, the peak frequency of which is related to the temperature of the hot-spot (the heater), and it is therefore useful to be able to estimate this temperature. The temperature of such heaters has been extensively studied [19],[23],[24]. The energy absorbed from the laser beam will first be transferred to the electrons in the aluminium film, and then to the phonons. The phonons thus generated in the film travel to the boundary between the substrate and the film, where they are either reflected, transmitted, or undergo mode conversion, as mentioned above. The resulting thermal boundary resistance is calculated using acoustic mismatch theory [19], and is dependent on the density of the two materials and the values of the group velocities within the materials, and has, in theory, no frequency dependence. If T_0 is the temperature of the substrate, which is assumed not to be influenced by the transmitted energy, then the heater temperature, T_1, is given by [23]

$$T_1^4 = T_0^4 + \frac{120\hbar^3}{\pi^2 k_B^4}\frac{P_L}{A}\left(\frac{e_L^{(1,0)}}{c_L^2} + \frac{2e_T^{(1,0)}}{c_T^2}\right)^{-1} \tag{2.4.1}$$

where A is the area of the film which is heated by the laser (i.e. the area of the laser focus) and P_L is the absorbed laser power. c_L and c_T are the longitudinal and transverse group velocities in the first material (the metal film), and $e_L^{(1,0)}$ and $e_T^{(1,0)}$ are the half space emissivities [2] from the film to the semiconductor, with the indices (0) and (1) denoting the metal film and the semiconductor respectively. If we take the value of A to be $100\mu m^2$ [25], and using the values given by Rösch[3] [24], of $e_L^{(1,0)} = 0.891$, $e_{ST}^{(1,0)} = 0.635$ and $e_{FT}^{(1,0)} = 0.795$ and the sound velocity in aluminium of $c_L = 6260ms^{-1}$ and $c_T = 3080ms^{-1}$, the heater temperature is then given by

$$T_1 = \sqrt[4]{T_0^4 + 2.23 \times 10^7 P_L}, \tag{2.4.2}$$

where P_L is the absorbed laser power in watts. For an assumed absorbed laser power of $1mW$, and a bath temperature of 1.1K this gives a value of $T_1 \sim 12K$. This can be related to the dominant frequency in a

[2]The emissivity is the ratio of the total phonon power actually emitted into material (1) to the same power under perfect matching conditions: i.e. for a black body emitter, $e^{(1,0)} = 1$.

[3]These values are for a germanium/aluminium interface, but will be used as an approximation for GaAs. The elastic constants of GaAs lie within about 10% of those for germanium, and this will give results which are within the order of the other errors in the approximation.

Planckian spectrum using

$$\nu_d = \frac{2.8 k_B T_1}{h}, \tag{2.4.3}$$

which on substitution gives a dominant frequency of around 715GHz. For bath temperatures of 4.2K, the respective peak frequency is very similar ~720GHz, since the effect of the bath temperature is small.

2.4.2 Superconducting tunnel junctions.

Monochromatic phonons may be produced (and also detected) by tunnel junctions [3]. Generally, superconducting tunnel junctions (SCTJ) have been used, but the development of normal state tunnel junctions (NSTJ) which enable phonon spectroscopy in high magnetic fields has also been successfully achieved [26]. The tunnel junctions, both normal state and superconducting, consist of two metal films which are separated by an insulating oxide layer (see Figure 2.4.1).

In the following section only superconducting junctions will be considered; a brief description of the normal state tunnel junction, which was developed during this work, will be given in Appendix B. For the case of superconducting tunnel junctions at temperatures below the critical temperature the films are superconducting and the Cooper pairs formed obey Bose statistics and occupy the ground state of the system. An energy gap, $E_g = 2\Delta$, separates the superconducting ground state from the first excited state. Above the energy gap, the Cooper pairs

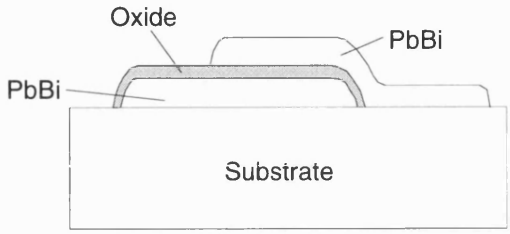

Figure 2.4.1: *Schematic diagram of the tunnel junctions: an oxide layer (the tunnelling barrier) is sandwiched between two metal films.*

are no longer bound, and quasi-particles can exist. Under an applied bias across the tunnel junction, these quasi-particles are able to tunnel through the oxide. Figure 2.4.2 shows the energy density of states for a superconducting tunnel junction under different bias conditions. In (a) the applied bias is less than $2\Delta/e$, but there is a small amount of tunnelling at finite temperature due to thermally excited quasi-particles. When the bias voltage exceeds $2\Delta/e$, (b), there is a sudden increase in the tunnelling current. This is because quasi-particles on the left now have access to empty states on the right, and therefore the probability of tunnelling increases. As the bias voltage is increased further, (c), the tunnelling current increases linearly. The current-voltage characteristic for such a tunnel junction is shown in Figure 2.4.2(d).

Once the quasi-particles have tunnelled through the barrier they have excess energy, which they lose by emitting phonons. There are two parts to the process in which the quasi-particles relax. In the first part, they relax by transitions towards the gap edge. This results in a broad band relaxation spectrum of emitted phonons, which exhibits a

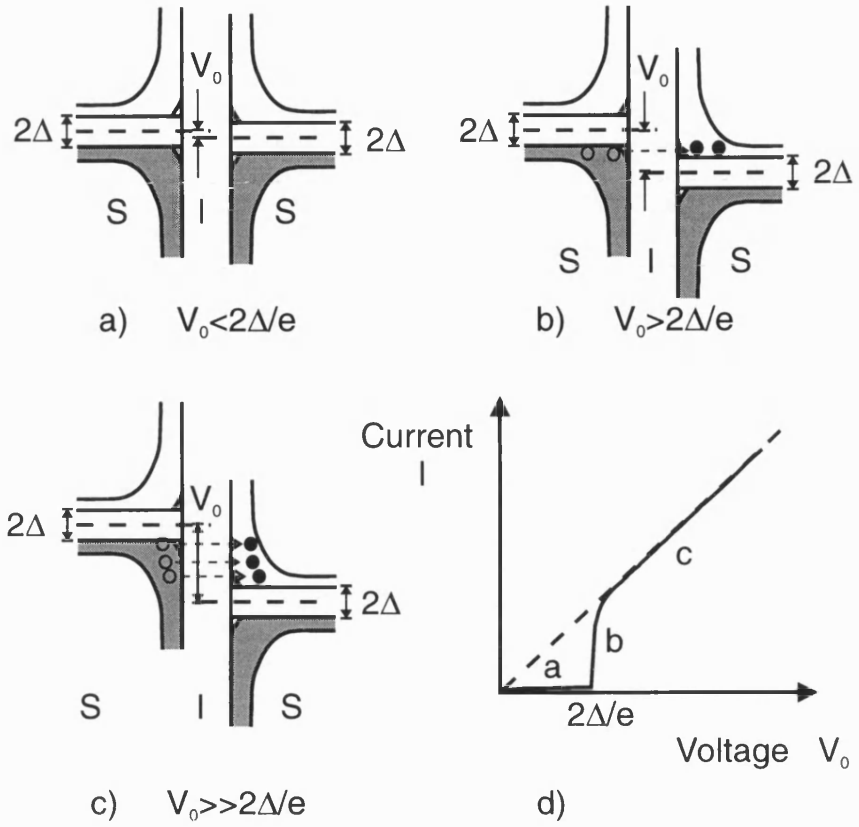

Figure 2.4.2: *Schematic diagram of the energy density of states for a superconducting tunnel junction (for a description see the text).*

discontinuous cut-off at the frequency given by $eV_0 - 2\Delta$, where V_0 is the applied bias. This maximum frequency corresponds to the transition from the top of the injected distribution down to the gap edge in a single step. In the second process, the quasi-particles recombine into the pair condensate. This step is usually slower because it depends on the availability of partners. The resulting recombination spectrum consists of phonons with energies of 2Δ or higher. By modulation of the bias

voltage on the tunnel junction a quasi-monochromatic source of phonons can be produced [27]. This arises because the discontinuous cut-off in the relaxation spectrum is dependent on bias voltage. In Figure 2.4.3a the tunnelling characteristic is shown, with an operating point V_0 indicated. Figure 2.4.3b shows the corresponding (total) emitted phonon spectrum. If the operating point is now shifted to $V_0 + \delta V$, the cut-off frequency shifts accordingly. The difference of the two spectra is given by the hatched area. This difference can be detected alone when δV is a time varying voltage, and the phonon detector is operated at the modulation frequency. Thus a tunable source of quasi-monochromatic phonons can be produced, the frequency of which is dependent on the bias voltage.

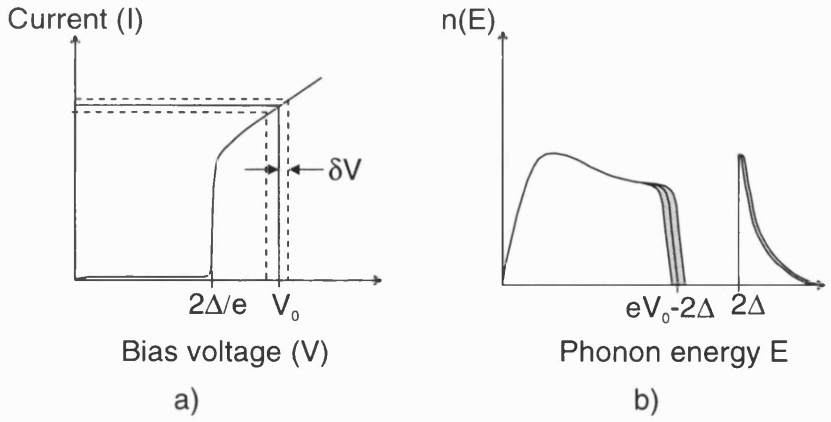

Figure 2.4.3: *Diagram showing the modulation method of producing monochromatic phonons.*

2.5 Phonon absorption by a 2DEG

In the situations described in this thesis, the 2DEG is enclosed within a crystal lattice. This means that there will be a continuous exchange of energy and momentum between the electron system and the lattice via the emission and absorption of phonons. This process is important since it is the dominant mechanism by which a heated electron system loses its energy and cools to thermal equilibrium with the lattice. In the following section the basic theory of phonon absorption by a 2DEG is presented.

The absorption of a phonon of energy $\hbar\omega$, (at 0K) scatters an electron from an occupied state $|\vec{k}_i| \leq k_F$, to an unoccupied state $|\vec{k}_f| > k_F$, subject to conservation of momentum in the plane, $\vec{k}_f = \vec{k}_i + \vec{q}_{||}$, and conservation of energy $E(\vec{k}_f) = E(\vec{k}_f) + \hbar\omega_q$, where $\vec{q}_{||} = \vec{q}\sin\theta$ and θ is the angle between the q-vector and the normal to the 2DEG, as shown in Fig. 2.5.1. The transition rate is given, using Fermi's Golden Rule, as

$$\Gamma(\vec{q}) = \frac{2\pi}{\hbar}\sum_{i,f}|M|^2|\langle i|e^{i\vec{q}\cdot\vec{r}}|f\rangle|^2\delta(E_i+\hbar\omega_q-E_f)f(E_i)[1-f(E_f)] \quad (2.5.1)$$

where $f(E_i)[1-f(E_f)]$ gives the probability of the initial electron state being occupied, and the final state being empty. $|M|^2|\langle i|e^{i\vec{q}\cdot\vec{r}}|f\rangle|^2$ is the matrix element of the interaction which will be considered in more detail in Section 2.6. The conditions for the conservation of momentum can

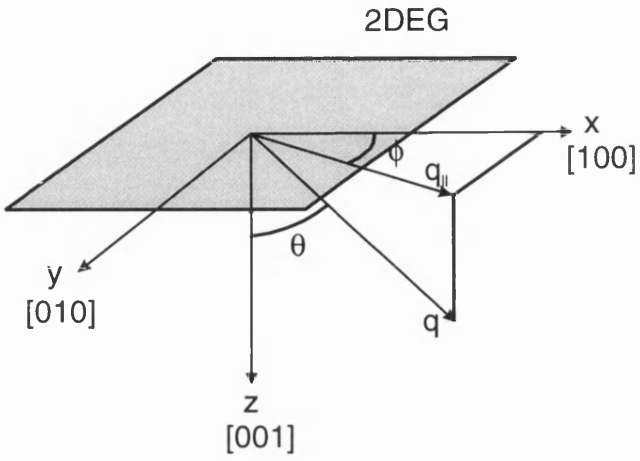

Figure 2.5.1: *Definition of the angles θ and ϕ.*

be obtained by substitution of the wave function into $\langle i|e^{i\vec{q}\cdot\vec{r}}|f\rangle$. The wave function used is

$$\Psi_{i,k_{||}}(x,y,z) = e^{i\vec{k}_{||}\vec{r}_{||}}\Phi_i(z)\frac{1}{\sqrt{L_x L_y}}. \tag{2.5.2}$$

Substitution of this then leads to

$$\langle i|e^{i\vec{q}\cdot\vec{r}}|f\rangle = F(q_z)\delta_{\vec{k}_i+\vec{q}_{||},\vec{k}_f} \tag{2.5.3}$$

where $\vec{k}_i$ and $\vec{k}_f$ describe the initial and final wave vectors and $\vec{q}_{||}$ gives the component of the absorbed phonon in the plane of the 2DEG. $|F(q_z)|^2$ is known as the form factor and is defined by

$$|F(q_z)| = \int dz|\Phi_0(z)|^2 e^{iq_z z}. \tag{2.5.4}$$

As a good approximation, the wave-function often used is the Fang-Howard wave-function [28] which is given by

$$\Phi_0(z) = \begin{cases} (\frac{1}{2a^3})^{1/2} z e^{-z/2a} & z > 0 \\ 0 & z \leq 0 \end{cases} \tag{2.5.5}$$

where a is a measure of the extent of the 2DEG in the z-direction. Substitution of the Fang-Howard wave function into equation (2.5.4) gives

$$|F(q_z)|^2 = \frac{1}{(1 + q_z^2 a^2)^3}. \tag{2.5.6}$$

This is a result of the uncertainty principle allowing the exchange of out-of-plane momentum, p_z, provided $p_z \leq 2\pi\hbar/\Delta z$, where Δz is the extension of the electron wave-function in the z-direction, even though, since the electron motion is strictly two dimensional, there should be no out-of-plane absorption. This means that the greater the confinement in the z-direction, the less strict the limitation on out-of-plane absorption, so that in practice, the momentum component of phonon absorption in the z-plane is not restricted when $q_z a \ll 1$. The form factor has a maximum value of 1, rolls off with increasing q_z, with its half maximum occurring at $q_z a \sim 0.51$, and goes to zero for $q_z a \gg 1$. Figure 2.5.2 shows the form factor for different values of the thickness parameter a.

The δ-function in equation (2.5.3), $\delta_{\vec{k}_i + \vec{q}_{||}, \vec{k}_f}$, gives the condition for conservation of momentum in the $x - y$ plane: i.e. $\hbar\vec{k}_f = \hbar\vec{k}_i + \hbar\vec{q}_{||}$.

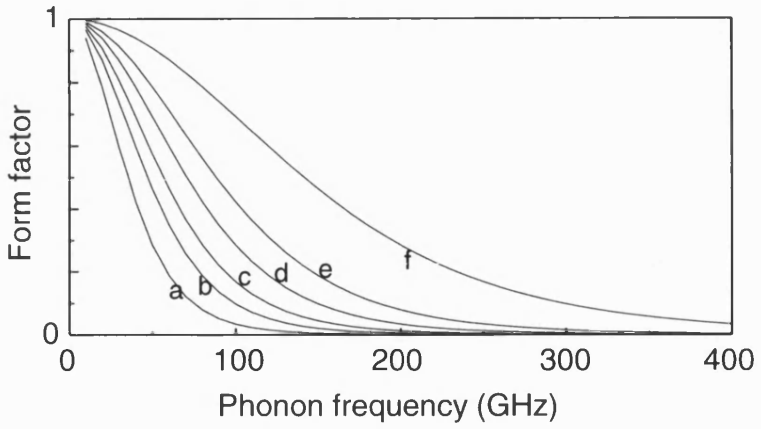

Figure 2.5.2: *The form factor as a function of phonon frequency for different values of a. The values of a used are: a) 20nm, b) 15nm, c) 12.5nm, d) 10nm, e) 8nm, f) 5nm. The angle, θ, for all curves is 55^o. It can be seen that as the lateral extent of the 2DEG decreases, the restriction on out-of-plane momentum becomes more relaxed.*

This means that $\vec{k}_i$ and $\vec{k}_f$ can differ by a maximum of $2k_F$ [4], i.e.

$$|\vec{k}_i - \vec{k}_f| \leq 2k_F. \tag{2.5.7}$$

This is due to scattering being quasi-elastic, which means that the initial and final states of the scattering process must lie on the Fermi surface at T=0K, and within $\pm k_B T$ of the Fermi surface at higher temperatures. This is because the electron gains only small amounts of energy by absorbing a phonon. This limits the absorption of phonons to those

[4]This is not strictly correct, since the momentum change will be slightly larger than $2k_F$, since the final electron state must lie slightly above the Fermi surface.

where

$$\hbar|q_{||}| \leq 2\hbar k_F. \tag{2.5.8}$$

This is known as the $2k_F$ cut-off and is shown schematically in Figure 2.5.3.

Going back to equation (2.5.1) the formula for the absorption rate

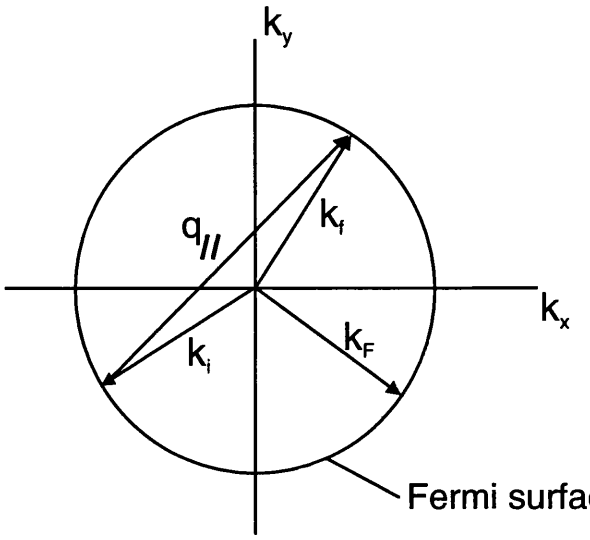

Figure 2.5.3: *The $2k_F$ cut-off. It can be seen that the maximum momentum change that can occur in a scattering process is $2\hbar k_F$.*

is given by

$$\Gamma(\vec{q}) = \frac{2\pi}{\hbar} \sum_{i,f} |M|^2 |\langle i|e^{i\vec{q}\cdot\vec{r}}|f\rangle|^2 \delta(E_i + \hbar\omega_q - E_f) f(E_i)[1 - f(E_f)]. \tag{2.5.9}$$

In order to calculate this explicitly the sum must be converted into an integral. The integration is made easier by the fact that the matrix element $M\langle i|e^{i\vec{q}\cdot\vec{r}}|f\rangle$ and the density of states can be taken out of the

integral. This integral has been performed by Hensel et.al. [29] to give an absorption rate of

$$(\tau_{e-p})^{-1} = \frac{2\pi}{\hbar} G(q_{||}, \theta) L_x L_y |M|^2 |F(q_z)|^2. \tag{2.5.10}$$

$G(q_{||}, \theta)$ is obtained by the integration of $f(1-f)$ under conservation of momentum, and is given by the following equation:

$$G(q_{||}, \theta) \simeq \begin{cases} (k_F^2 - k_0'^2)^{1/2} - (k_F^2 - k_0^2)^{1/2} & 0 \leq \frac{1}{2}q_{||} < k_F - \frac{m^* s}{\hbar} \\ (k_F^2 - k_0'^2)^{1/2} & k_F - \frac{m^* s}{\hbar} \leq \frac{1}{2}q_{||} < k_F + \frac{m^* s}{\hbar} \\ 0 & \frac{1}{2}q_{||} \geq k_F + \frac{m^* v}{\hbar} \end{cases} \tag{2.5.11}$$

where

$$k_0' = \frac{q_{||}}{2} - \frac{m^* s}{\hbar}, \tag{2.5.12}$$

$$k_0 = \frac{q_{||}}{2} + \frac{m^* s}{\hbar} \tag{2.5.13}$$

and

$$s = \frac{v_s}{\sin\theta}. \tag{2.5.14}$$

This is the mathematical description for the $2k_F$ cut-off that was described earlier and which is shown in Figure 2.5.4 as a function of phonon frequency (at $T = 0K$) for different values of sheet density n_s.

As can be seen, the limit due to the $2k_F$ cut-off is a strong function of electron sheet density n_s(since $k_F \propto n_s^{1/2}$), and suggests that the absorption should be limited more to the normal to the 2DEG as the electron density decreases. Both the $2k_F$ cut-off and the form factor

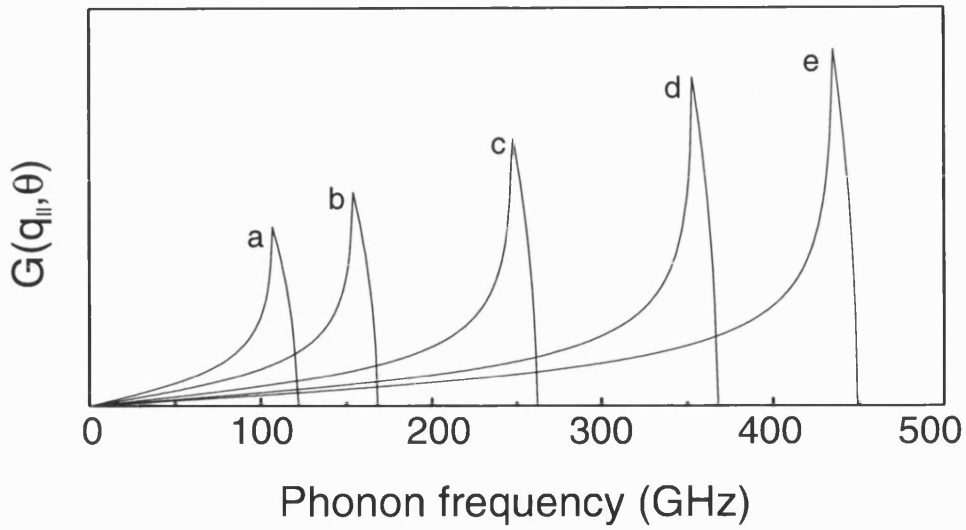

Figure 2.5.4: *$G(q_{||}, \theta)$ as a function of phonon frequency for 5 different values of sheet density n_s. a) 5×10^{10}; b) 1×10^{11}; c) 2.5×10^{11}; d) 5×10^{11}; e) $7.5 \times 10^{11} cm^{-2}$. For all curves $\theta = 55^o$.*

also vary, through $\vec{q}$, on the angle of absorption. Figures 2.5.5 and 2.5.6 show the form factor and the factor $G(q_{||}, \theta)$ as a function of absorption angle θ.

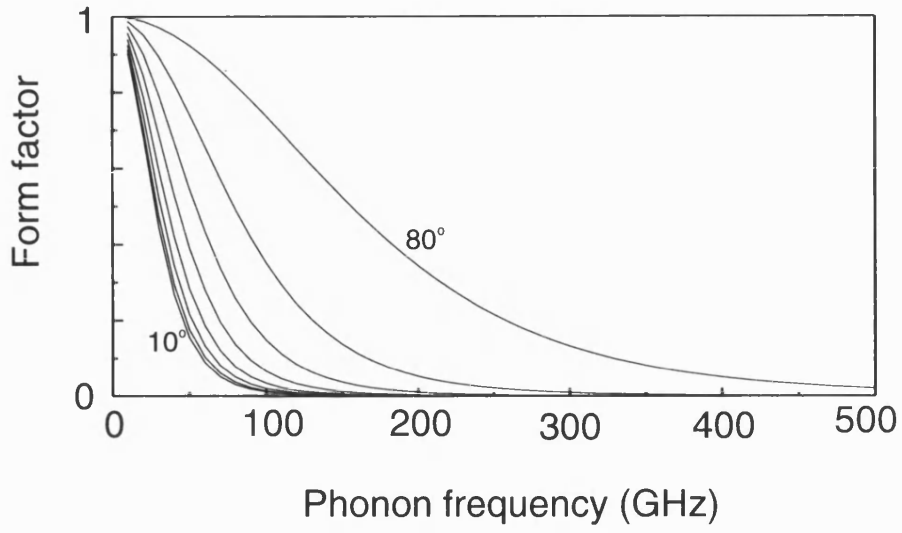

Figure 2.5.5: *Form factor plotted as a function of absorption angle θ for angles from 10^o to 80^o in steps of 10^o. The parameter a is 15nm for all curves.*

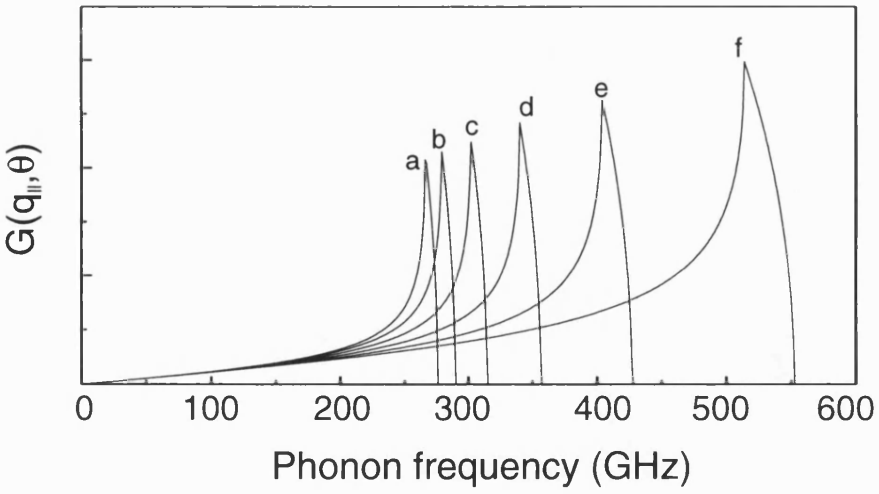

Figure 2.5.6: *$G(q_{||}, \theta)$ plotted as a function of absorption angle θ. a) 80^o; b) 70^o; c) 60^o; d) 50^o; e) 40^o; f) 30^o. The carrier concentration used is $4.1 \times 10^{11} cm^{-2}$.*

2.6 Matrix element

The matrix element contains information about the dominant type of interaction that takes place. Acoustic phonons can couple to the electrons in the 2DEG through either the deformation potential or the piezoelectric interaction. In the next sections, brief descriptions of these interactions will be given.

2.6.1 Deformation potential

The deformation potential arises because of the detailed band structure of solids. In the presence of a crystal potential, which arises from the atoms in the lattice, the electronic energy levels fall into distinct energy bands. When an acoustic wave propagates through the solid the atoms are displaced from their equilibrium positions. Because of this displacement, the crystal potential in which the electrons move is deformed, as are the electronic energy levels which arise from the potential.

The energy change, ΔE, of the electronic energy levels is given by

$$\Delta E = \sum_{i,j} \Xi_{i,j} S_{i,j} \tag{2.6.1}$$

where $\Xi_{i,j}$ is the component of the deformation potential tensor, and $S_{i,j}$ is the component of the strain tensor:

$$S_{i,j} = \frac{1}{2}\left(\frac{\partial u_i}{\partial x_j} + \frac{\partial u_j}{\partial x_i}\right). \tag{2.6.2}$$

The vector $\vec{u}$ describes the displacement of a volume element from its equilibrium position. For the Γ-point in GaAs the deformation potential tensor is diagonal and the diagonal elements are given by Ξ_d. Equation (2.6.1) then simplifies to

$$\Delta E = \Xi_d \nabla . \vec{u}. \tag{2.6.3}$$

When a phonon passes through the crystal it produces an oscillating strain, which is caused by the mechanical displacement $\vec{u}(r)$:

$$\vec{u}(r) = \left(\frac{\hbar}{2\rho V \omega_{\vec{q}_s}}\right)^{\frac{1}{2}} (\hat{a}_{q_s} e^{i\vec{q}_s \cdot \vec{r}} + \hat{a}^{\dagger}_{q_s} e^{-i\vec{q}_s \cdot \vec{r}}) \epsilon_{qs}. \tag{2.6.4}$$

Here, q_s is the phonon wave vector for the phonon mode s, ϵ_{q_s} is the polarisation vector of the phonon with mode s, ω_{q_s} is the angular frequency of the phonon, V is the volume, and ρ is the density. $\hat{a}$ and $\hat{a}^{\dagger}$ are the annihilation and creation operators.

Putting equation (2.6.4) into equation (2.6.3) gives the deformation potential which is given by

$$M_{def} = \left(\frac{\hbar}{2\rho\omega_{q_s} V}\right)^{\frac{1}{2}} i\Xi_d \vec{q}_s \epsilon_{q_s} \left(\hat{a}_{q_s} e^{i\vec{q}_s \cdot \vec{r}} - \hat{a}^{\dagger}_{q_s} e^{-i\vec{q}_s \cdot \vec{r}}\right). \tag{2.6.5}$$

2.6.2 Piezoelectric interaction

Since GaAs is a polar crystal without inversion symmetry, a strain or displacement can also lead to an electric field, due to the piezoelectric

effect. The vector components of the electric lattice polarisation P can be given by the following strain:

$$P_i = \sum_{k,l} e_{ikl} S_{kl} \tag{2.6.6}$$

where e_{ikl} are the components of the piezoelectric tensor and S_{kl} are the usual components of the strain tensor. For the zinc-blende structure of GaAs it is only necessary to consider one element of the piezoelectric tensor (e_{14}). Using this, the piezoelectric interaction is given by

$$\begin{aligned} \Delta E_{piezo} &= \left(\frac{e e_{14}}{\epsilon_o \epsilon_r}\right)\left(\frac{\hbar}{2\rho V \omega_{q_s}}\right)^{\frac{1}{2}} 2i\Big(\epsilon_{q_s,x} q_y q_z + \epsilon_{q_s,y} q_x q_z + \epsilon_{q_s,z} q_x q_y\Big) \\ &\quad \times \frac{1}{q^2}\Big(- \hat{a}_{q_s} e^{i\vec{q}_s \cdot \vec{r}} + \hat{a}^{\dagger}_{q_s} e^{-i\vec{q}_s \cdot \vec{r}}\Big), \end{aligned} \tag{2.6.7}$$

At higher phonon energies the piezoelectric interaction decreases, whereas the interaction via the deformation potential increases. For this reason, the piezoelectric interaction will be the dominant one at low phonon energies and low temperatures.

In GaAs the deformation potential only allows for coupling to the LA mode: for the piezoelectric potential the situation is more complicated. The piezoelectric coupling disappears for all phonon modes in the ⟨100⟩ direction, for the ⟨110⟩ direction couples only to transverse modes, and for the ⟨111⟩ direction only to longitudinal modes. However, it is important to remember that the polarisation of the modes is not exact, i.e. that the modes are not purely longitudinal or transverse,

and for this reason all phonon modes will couple, to a larger or smaller extent, with both forms of interaction.

2.7 Phonon drag: the 2DEG as a phonon detector

In a system of two or more subsystems of interacting quasi-particles, a directed flow appearing in either of these systems will bring about a partial transfer of momentum to the other one. This leads to a directed flow of quasi-particles in the second subsystem. This process, when it occurs between electrons and phonons is known as the phonon-drag effect, and was first predicted by Gurevich in 1946, and first experimentally demonstrated by Frederikse [30] in 1953. A detailed description of many aspects of phonon-drag can be found in Ref. [31] and references therein.

The measurements presented here use the interaction of the ballistic acoustic phonons with the electrons in the 2DEG as a direct measurement of the phonon intensity. The electrons in the 2DEG are defined by the distribution function $\tilde{f}$. In the case of electrons without the influence of phonons, this is simply the Fermi-function, f. When a phonon interacts with an electron, it transfers its energy and momentum to the electron. Due to electron-electron interactions, this 'excited' electron then transfers its gained energy and momentum, within a very short

time (a few hundred fs), to all of the electrons in the 2DEG, and therefore changes $\tilde{f}$. The transfer of energy causes a rise in temperature of the 2DEG, whereas the momentum transfer leads to an electric field, or an electric current; this is because the transfer of momentum leads to the Fermi circle being shifted in the same direction as the incoming phonons: i.e. the exchange of momentum causes a current to flow until an opposing electric field is established, which can be measured as a voltage across the terminals of the device. This effect is shown in Figure 2.7.1, and is known as the phonon-drag effect. The electric field or current so set up can then be measured as either a current or a voltage. Although the measurement of a current is, in principle, slightly different from that of a voltage, it will be shown that both methods produce qualitatively the same results.

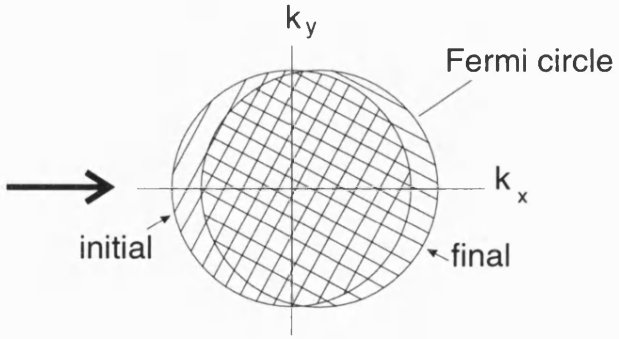

Figure 2.7.1: *The origin of phonon drag: the phonons are incident along the direction of the arrow, and cause the Fermi-surface to be shifted in that direction.*

Chapter 3

Theoretical investigation

The spatially resolved experimental results to be presented in Chapter 5 show features which cannot be explained using a simple theory of phonon focussing which assumes that a constriction within the 2DEG acts as a point detector. It is also obvious from some of the geometries to be used, that the assumption of a point detector is no longer valid. Therefore it is necessary to develop a theory which takes the finite extent of the detector geometry into account. The next section describes the attempts to theoretically model the experimental results obtained, and will show that very good agreement can only be achieved when the complete sample geometry is considered.

3.1 Simple theoretical model

All previous explanations of phonon-drag imaging have assumed a point detector and a point source. On occasions when an extended detector has been assumed, this was only done to the extent that the detector was split into a large number of point detectors, and the contribution from all these detectors was then summed [32]. This is a very simplistic model, and assumes that when phonons are incident on the 2DEG there will be a uniformly weighted signal, when they are incident elsewhere, the signal will be zero. A simulation of this type has been performed for a sample with a small square constriction (A2), the exact geometry of which is shown in Fig. 3.1.1, and which is equivalent to the experimental sample geometry A1 (shown in Figure 4.3.1). The sample was simulated

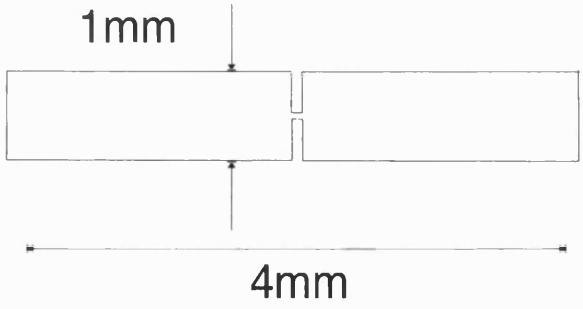

Figure 3.1.1: *Sample geometry A2: the constriction is* $50 \times 50 \mu m^2$.

using a 400 × 100 site lattice, where the 2DEG was defined by regions of a signal of +1, and the outside regions were defined by a signal of zero. The focussing image for the piezoelectric interaction (shown in Fig. 2.3.4) is then convoluted with this response function, and integrated

over the whole sample area.

Obviously when the complete focussing image is incident on the 2DEG, the positive and negative parts of the image will cancel out, giving zero signal. It is therefore only going to give a non-zero signal, when parts of the focussing image are incident on areas where no 2DEG exists. The result is then an image of the voltage across the sample as a function of laser position, which can be seen in Fig. 3.1.2A.

When this image is compared to the experimental image obtained (Fig. 3.1.2B), then it can be seen that there is very little agreement between this type of simulation and the experiment. For this reason it has been necessary to develop a slightly more complex model [33], which will be described in the following section.

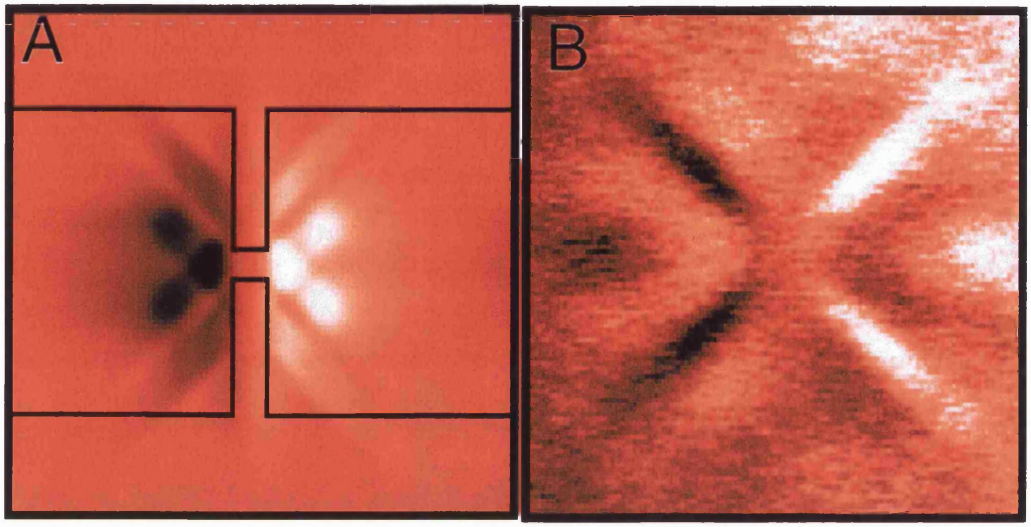

Figure 3.1.2: *A) Results of the simple simulation, assuming a uniform response of the 2DEG to the incoming phonons. Bright and dark regions correspond to areas of large positive and negative signals respectively. Here just the central portion of the image is shown, and the respective part of the geometry is superimposed onto the image. B) Experimental image for sample geometry A1. It can be seen, by comparison of the two images, that this simple simulation does not accurately reproduce the experimental results.*

3.2 Theoretical model of phonon-drag imaging

The model is based on the fact that the incoming phonon flux induces a voltage across the sample, due to the phonon-drag effect as described in Section 2.7. To obtain this voltage one needs to solve the 2D Poisson equation for the phonon flux, using the relevant boundary conditions. Since it is impossible to find a solution of the 2D Poisson equation which satisfies the boundary conditions for a broad beam phonon flux with arbitrary weighting at any position on the detector, a Greens function approach to the problem has been adopted. The Poisson equation is solved for a point phonon source, subject to the given boundary conditions, to obtain a response function. This can then be integrated over the entire area of the detector after it has been weighted to take account of the magnitude of the phonon flux at a given point.

The assumption that is made when setting up this model is that, when in equilibrium (i.e. no phonon flux), the 2D system is assumed to be charge neutral and represents an equipotential: this is justified if it is assumed that the ionised donors and the free electrons co-exist: i.e. the ionised donors are projected onto the plane of the 2DEG, thus making the 2D system net charge neutral [34]. Screening is also neglected in this model, but the excellent agreement between the calculation and the experimental results indicates that these assumptions are valid.

By considering the phonon flux in terms of the phonon-drag effect, where the incoming phonons cause the electrons to move in one direc-

tion, it is easy to see that the phonon flux at a point $\vec{r}_o$ can be modelled by a 'local charge dipole' centred at the point $\vec{r}_o - \vec{d}/2$, with a length $\vec{d}$. The differential equation which governs this situation is then of the form

$$\nabla^2\phi(\vec{r},\vec{r}_o) = \frac{\delta(\vec{r}-\vec{r}_o) - \delta(\vec{r}-(\vec{r}_o-\vec{d}))}{|\vec{d}|\epsilon_o\epsilon_r}. \qquad (3.2.1)$$

This equation has to be solved for a point phonon source at an arbitrary point in the detector. The method used to solve this is a finite difference method, which is an approximate method, but one which will be shown to give good agreement to the experimental results. The 2DEG detector is represented as a finite element array, with the charge dipole positioned at a point $\vec{r}_o$ (see Fig 3.2.1). For simplicity, the positive end of the dipole is defined to be at the point $(\vec{r}_o)$ and the negative end at $(\vec{r}_o - \vec{d})$. The calculation is performed independently for dipoles directed parallel to the x-axis, and parallel to the y-axis. The array used is a 400 × 100 element array, which represents a 4mm × 1mm sample: i.e. the real separation, d, of each element in the array is 10μm. The charge dipole therefore has a real length of 10μm, which is similar to the experimental resolution obtained. This value of d will be shown to give very good agreement to the experimental results. Separating $\vec{r}$ into its x and y components, equation 3.2.1 can be reduced to

$$\nabla^2\phi_{(i,j)} \simeq \frac{1}{|\vec{d}|^2}(4\times\phi_{(i,j)} - \phi_{(i+1,j)} - \phi_{(i-1,j)} - \phi_{(i,j+1)} - \phi_{(i,j-1)}). \qquad (3.2.2)$$

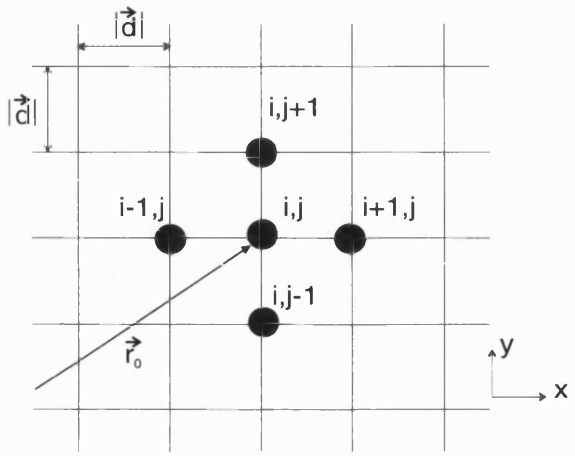

Figure 3.2.1: *Basis for finite element calculation. In the calculation the value of the potential at* (i, j) *is set to* $\Phi_{(i,j)} = +1$*, the value at* $(i-1, j)$ *is set to* $\Phi_{(i-1,j)} = -1$.

For all points except the charge dipole and the boundaries, equation (3.2.2) can be equated to zero, and then further simplified to

$$\phi_{(i,j)} = \frac{(\phi_{(i+1,j)} + \phi_{(i-1,j)} + \phi_{(i,j+1)} + \phi_{(i,j-1)})}{4} \tag{3.2.3}$$

i.e. the potential at one point is the mean value of the potential at the four neighbouring points. Assuming an initial form of $\phi_{(i,j)}$ i.e. $\phi_{(i,j)} = 0$, equation (3.2.3) is then solved iteratively at every site in the lattice *except* the dipole source and the boundary until convergence is reached. The condition for convergence is that the variation in voltage between the ends of the sample over an interval of 10000 iterations is less than 0.05%. The boundary condition is such that current cannot

flow across the etched boundary, $J_\perp = \sigma E_\perp = 0$, i.e. that there can be no electric field component perpendicular to the boundary. This is achieved by setting the potential at the boundary to the same value as that at the adjacent site in the perpendicular direction, (see Fig 3.2.2a) i.e.

$$\phi_{(i,j)} = \phi_{(i,j\pm1)} \qquad or \qquad \phi_{(i,j)} = \phi_{(i\pm1,j)}. \tag{3.2.4}$$

At outside corners the corner value is set to the mean value of the two neighbouring points, (see Fig. 3.2.2b) i.e.

$$\phi_{(i,j)} = \frac{1}{2}(\phi_{(i+1,j)} + \phi_{(i,j-1)}). \tag{3.2.5}$$

The inside corners are rounded off by one site, see Fig. 3.2.2c. This is a simplification which is valid since the etched corners in the real samples are not exactly right-angled. The boundary conditions can be set anywhere within the finite element array to produce arbitrary sample geometries.

The solution of equation 3.2.1 for single charge dipoles positioned at various points within the sample geometry are shown in Appendix A, where slightly more detail is given about the method of the simulation.

Once the potential has converged over the whole structure, the equivalent of the measured voltage is calculated. This is done by taking the difference of the average potential at each end of the geometry, i.e. $\Delta V = \bar{V}_2 - \bar{V}_1$, where $\bar{V}_2$ is the average potential at the right end of the sample, and $\bar{V}_1$ that at the left end. Once this has been calculated, the dipole is moved to the next lattice site, and the process repeated.

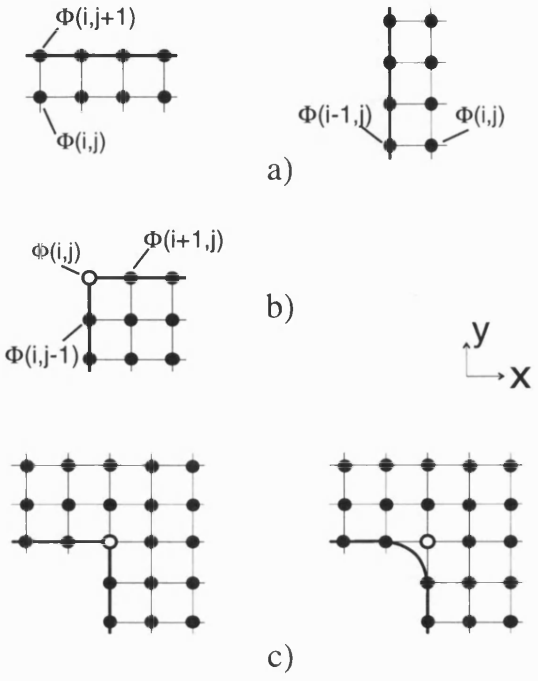

Figure 3.2.2: *The boundary conditions and corners for the model: a) shows the boundary conditions used to define the sample geometry:* $\phi_{(i,j)} = \phi_{(i,j\pm1)}$ *or* $\phi_{(i,j)} = \phi_{(i\pm1,j)}$. *b) shows the condition used for external corners:* $\phi_{(i,j)} = \frac{1}{2}(\phi_{(i+1,j)} + \phi_{(i,j-1)})$. *c) shows the treatment of the internal corners, where the corner is rounded off by one point.*

This gives a form of response function $\Delta V_{(i,j)}$ for dipole positions (i, j), which is used later in the calculation. This calculation is performed separately for dipoles directed in the $x-$ and $y-$directions.

The next step is to calculate the phonon focussing pattern for the samples used. This has been extensively studied theoretically [32],[9] and is achieved using a Monte-Carlo simulation (the program used for

this was developed by Walter Backes and Ralf Wichard [35]). In this program, the q-vectors are produced randomly, and for all q-vectors the group velocity and phase velocity are calculated. The incidence point of all q-vectors on the 2DEG is then calculated and from this the contribution to the phonon-drag voltage. This gives an image of the theoretical phonon-drag for a point source and a point detector. This was done separately for the piezoelectric interaction and the deformation potential, and for the $x-$ and $y-$components. The results of this calculation for the piezoelectric interaction are shown in Figure 3.2.3, and the results for the deformation potential are shown in Figure 3.2.4. The real position of the phonon source is given by the centre of the image.

The final step of the calculation to is convolute the focussing im-

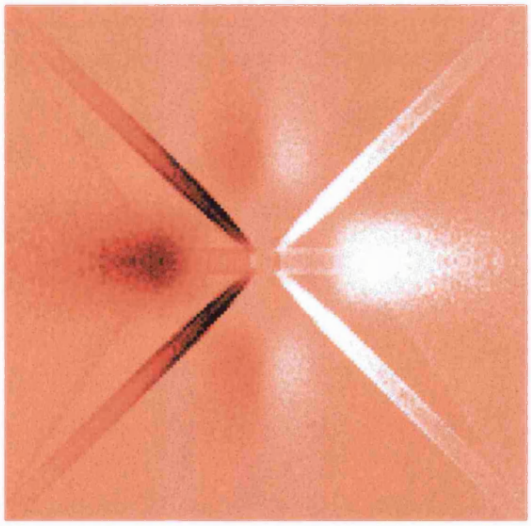

Figure 3.2.3: *The result of the phonon focussing calculation for the piezoelectric interaction for the (100) surface of GaAs.*

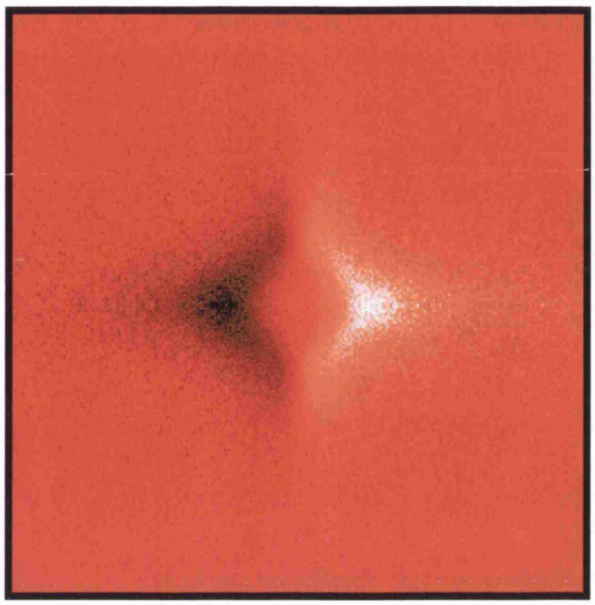

Figure 3.2.4: *The result of the phonon focussing calculation for the deformation potential for the (100) surface of GaAs.*

age with the response function. This is done by taking the results of the phonon focussing image, moving the source point over the whole sample, and weighting each electron-phonon interaction with the voltage between sample ends which occurs for the local dipole situated at that point: i.e. initially one phonon source point will be taken, for each point where phonons are incident on the 2DEG (given by the focussing image) the voltage due to a dipole at that point together with the intensity from the focussing image give the voltage measured. This is integrated for all phonons and for all source positions. This convolution was performed separately for the $x-$ and $y-$components, and then added to give the final result. This then gives an image of the voltage

difference between the ends of the sample as a function of the position of the source of the phonons. The calculation was performed for various sample geometries as will be described in Section 7.

Chapter 4

Samples

In this chapter the preparation and processing of the samples will be described. There will also be a short discussion of the sample geometry used, although this will be covered in more detail in Section 7. This section introduces the following two chapters where the two main experiments performed are described.

4.1 2DEG Samples

The 2DEG samples used in this work are modulation doped gallium arsenide/ aluminium gallium arsenide (GaAs/AlGaAs) heterostructures grown by Molecular Beam Epitaxy (MBE). In such heterostructures there is an interface between two semiconductors with different values

of band gap, and a donor layer close to the interface. The growth procedure for high mobility 2DEGs by molecular beam epitaxy (MBE) is well documented in the literature, [36],[37],[38] and will not be discussed here. However, the properties of the structures, and the processing steps that are necessary for the experiment will be discussed.

4.1.1 Sample characteristics

The structure of a typical MBE grown sample (# 8045) is shown in Figure 4.1.1. It was grown on a semi-insulating (SI) GaAs substrate of approximately 350μm thickness. First 610 periods of alternate monolayers of Ga and As are grown, which serve to bury the impurities from the substrate, and to prevent their diffusion to the active regions of the device. This is used instead of the normal GaAs/AlAs short period superlattice since it does not influence the phonon properties. This is followed by 2μm of undoped GaAs, called the buffer, on top of which is grown an undoped $Al_xGa_{1-x}As$ layer, known as the spacer. This is in turn followed by silicon-doped $Al_xGa_{1-x}As$, on top of which is a layer of GaAs, which protects the reactive $Al_xGa_{1-x}As$ from the environment. The aluminium content is approximately 30% ($x = 0.3$). In order for the Fermi energy to be the same throughout the system, the Si donors become ionised, and the carriers diffuse to the interface between the GaAs and the $Al_xGa_{(1-x)}As$. This in turn causes band-bending, which results in the GaAs conduction band at the interface being below the

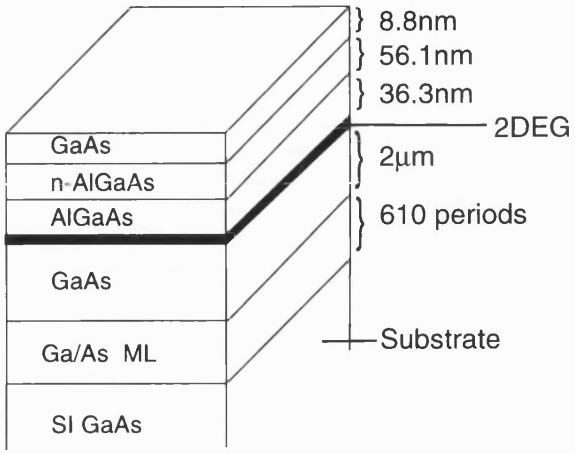

Figure 4.1.1: *Schematic diagram of the structure of the GaAs/AlGaAs heterostructures used in these experiments. The 2DEG is found at the interface between the GaAs and the AlGaAs layers. The electronic band structure of such a device is shown in Fig.2.1.1.*

Fermi energy. This allows free carriers to exist at the interface even at low temperatures, thus making the 2DEG. These carriers are spatially separated from their ionised donors, which results in a high mobility, since this is dominated by the scattering from ionised donors at low temperatures. A more detailed description of the electronic properties of the 2DEG has already been given in Section 2. Figure 2.1.1 in Section 2 shows the energy band diagram for such a heterostructure. The samples used here had carrier concentrations of $4.1 \times 10^{11} cm^{-2}$ and mobilities of $1 \times 10^{6} cm^{2}/Vs$, measured under illumination at 4.2K.

4.2 Sample processing

The samples are processed using conventional techniques of photo-lithography, etching and metallisation. Initially 5mm×10mm samples are cleaved from the wafer using a diamond scriber. The chips undergo an elaborate cleaning process which includes washing in acetone in an ultrasonic bath, and subsequent rinsing in iso-propanol. This cleaning process is repeated many times during the preparation. The samples are then coated with photo-resist (Shipley S1805, unthinned) with a spin speed of approximately 4500 rpm, for 30 seconds, which leads to a resist thickness of 350-400nm, and then baked for 25 minutes at 85^{o}C. The resist is then exposed to UV light through a mask which is in contact with the sample. The exposure time is approximately 12 seconds. After exposure the resist is developed using a mixture of 1:4 Shipley developer:water, for approximately 60 seconds. After development, during which the exposed resist is removed from the surface, the sample is etched to produce the desired pattern. The structure is wet-etched using a solution of H_2O:H_2O_2:H_2SO_4 in the ratio 1000:8:1, which has an etch rate of approximately 1.3nm per second. The samples are etched to a depth of 120nm, with the 2DEG being approximately 100nm under the surface. The cleaning, resist coating, and exposure steps are then repeated to define the contact pads, with an exposure time of approximately 25 seconds. After exposure the samples are soaked for 10 minutes in chlorobenzene (C_6H_5Cl) and then left to stand in air for 2

hours. This treatment produces a thin, hard crust on the resist surface which dissolves more slowly than the resist underneath, thus producing an 'undercut' which is important for the lift-off process after the evaporation of the metal.

The contacts consist of a 100nm layer of a Au/Ge alloy, followed by 40nm of Ni, both thermally evaporated in a vacuum system. The excess metal is removed by lift-off in acetone, whereby the photo-resist regions that still exist under the unwanted areas of metal are dissolved, simultaneously removing the layer of metal from everywhere except the contact areas. The electrical contacts to the 2DEG are formed by annealing the sample at 450^{o}C for 2 minutes in a N_2/H_2 atmosphere. The cleaning, resist and exposure steps are repeated once more to make the bonding contacts of 30nm Cr followed by a 200nm Au layer. Once again, the excess metal is removed by lift-off in acetone. The sample is then mounted in a sample holder, and bonded using 25μm diameter gold wire. Specific to this work is the fact that after bonding, the reverse side of the sample still needs to be accessible for evaporating the aluminium film or tunnel junction. For this purpose, special sample holders were developed where the sample is mounted face down on the holder, such that the bond pads are still accessible (see Fig. 4.2.1). After the 2DEG has been bonded, the aluminium film or tunnel junction can then be evaporated from the rear.

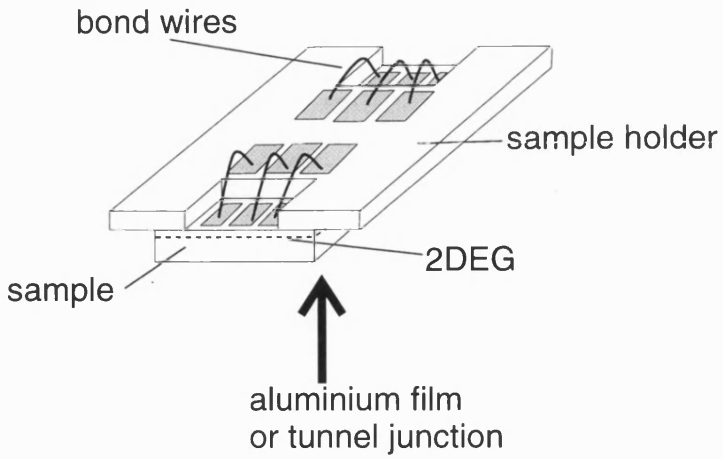

Figure 4.2.1: *Design of the sample holder, which enables both the 2DEG and the tunnel junction or aluminium film to be accessed.*

4.3 Sample geometry

Based on the results of previous experiments, [39,40] it was decided to use the 2DEG geometry shown in Fig. 4.3.1. The important features of this geometry are i) the constriction in the centre, and ii) the large distance between the contact pads and the constriction. These were chosen for a number of reasons. It had been concluded from previous work, that the constriction in the centre of the sample acts as the 'sensitive' region, and that in the imaging experiments, the signal from this region dominates, giving a spatially well defined phonon-drag focussing structure. It had also been concluded that for the phonon-drag imaging experiments it is important that the contacts are a large distance away from the constriction since a large thermal voltage is generated

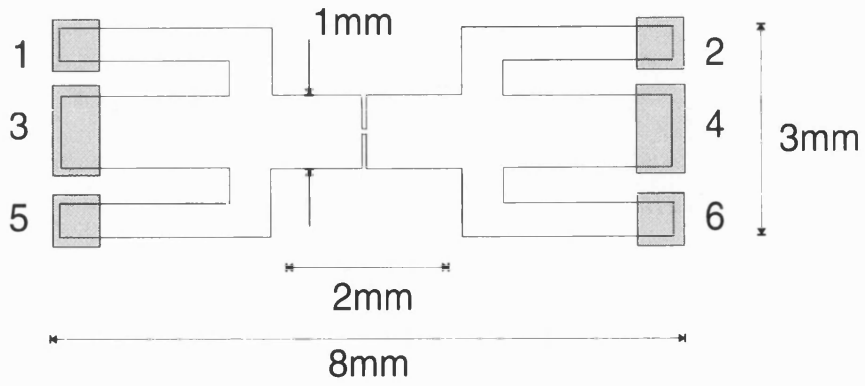

Figure 4.3.1: *Sample geometry (A) used for the phonon-drag experiments. The central constriction has an area of 50μm×50μm.*

at the contacts which is much larger than the phonon-drag signal to be measured, and therefore swamps the drag signal. These assumptions will later be shown to be invalid, and a more in-depth discussion of the role of the sample geometry will be given in Section 7. However for the initial measurements, the geometry shown in Fig.4.3.1, and hence referred to as geometry A, was used.

4.4 3DEG Samples

Experiments were also performed on three-dimensional electron gases (3DEGs). These samples consisted of a 2μm thick epitaxial layer of silicon-doped GaAs grown onto a SI substrate. The samples were pro-

cessed in the same manner as the 2DEG samples, except that the large etch depth (at least 2μm) that was necessary to isolate the structure required the use of a different etchant, since the usual etchant was too slow. For this reason an etchant with the following composition was used [41]: 50 weight percent citric acid aqueous solution ($C_3H_4(OH)(COOH)_3 \cdot H_2O$) to 30 weight percent hydrogen peroxide solution ($H_2O_2 \cdot H_2O$) in the ratio 5:1. The resulting solution had an etch rate of $\sim 2.5\mu$m min^{-1} at 50^oC under continuous stirring. The sample was etched into geometry A3 (see Fig. 5.3.1), which differs from geometry A1 only in the width of the hall bar; the size of the constriction remains the same ($(50\mu\text{m})^2$). The samples had a carrier concentration of $2.25 \times 10^{18} cm^{-3}$ and a mobility of $2237 cm^2/Vs$, measured under illumination at 77K.

Two different sets of experiments were performed on the 2DEG samples: the first set of experiments were spatially resolved imaging experiments, where the phonon-drag voltage at the 2DEG was measured as a function of position, similar to the experiments performed by Karl et.al. [9]. The 3DEG samples were also used for these experiments. The other measurements were frequency resolved experiments using superconducting tunnel junctions as generators of monochromatic acoustic phonons, where the phonon-drag voltage set-up in the 2DEG was measured as a function of phonon frequency, similar to the experiments performed by Lega et.al. [10]. The spatially resolved experiments will be described in the next section, and the frequency resolved experiments using su-

perconducting tunnel junctions as generators of quasi-monochromatic phonons in Section 6.

Chapter 5

Phonon-drag imaging experiments

In this section, the phonon-drag imaging experiments will be described. These experiments use a scanned laser beam to heat a metal film, thereby producing a local source of non-equilibrium phonons. The laser is scanned over the surface of the film, and by detecting the phonon signal as a function of laser position, a two-dimensional map of the phonon signal can be built up, a technique which was first demonstrated by Northrop and Wolfe [42],[43]. The electron-phonon interaction is detected by means of the phonon-drag effect, and was first applied in this way by Karl [9]. Measurements of the voltage at the 2DEG as a function of the laser position produce two-dimensional images of the phonon focussing, convoluted with the absorption probability.

5.1 Experimental details

In the next sections a description will be given of the experimental set-up for the phonon-drag imaging experiments performed. This will include a description of the film evaporation, and the apparatus used, as well as the measurement techniques applied.

5.1.1 Film evaporation

The aluminium film is thermally evaporated in a Univex evaporation system. The aluminium wire is placed in a tantalum metal boat which is resistively heated. Before evaporation the sample is cleaned in-situ using one minute of glow discharge in an oxygen atmosphere. The film is defined by evaporation through metal masks which are placed approximately 50μm away from the surface. The films were evaporated at a rate of 5Å per second to a thickness of 2000Å, at room temperature. The base pressure during evaporation was always less than 1×10^{-5}mbar.

5.1.2 Experimental set-up

After evaporation of the aluminium film, the sample was inserted into the cryostat and orientated such that the aluminium film was optically accessible with the laser beam. The measurements were performed at

1.1K, at which temperature the aluminium film is superconducting.[1] The optical set-up for the scanning of the laser beam is shown in Fig. 5.1.1. The set-up is built on a ferromagnetic metal table which, with the use of 'magnetic feet' for the optical components, allows the exact positioning of all parts.

The laser beam from the 5mW solid state laser is initially chopped

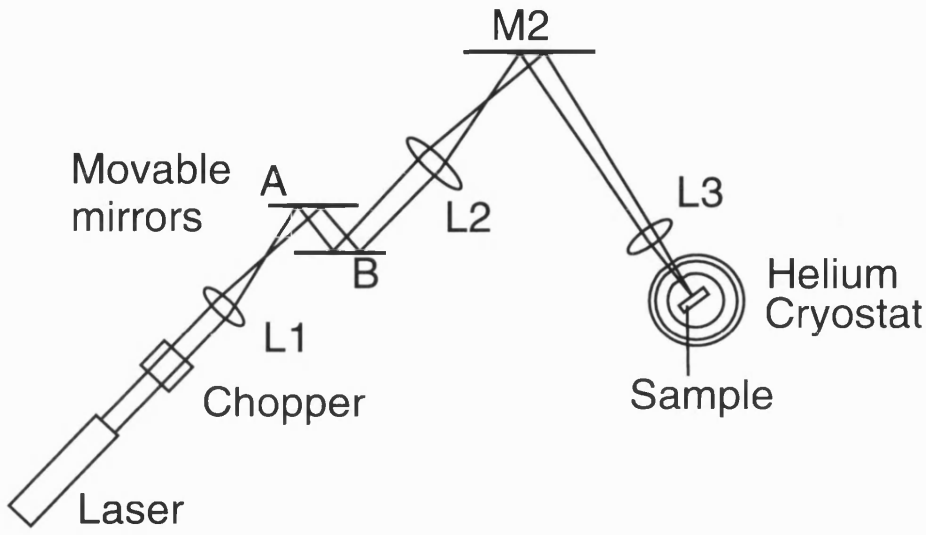

Figure 5.1.1: *Schematic diagram of the experimental set-up (not to scale).*

using a beam chopper, at a frequency of approximately 780Hz. The beam then passes through the lens L1 which, together with L2, pro-

[1]It will later be shown that similar results can also be obtained when the film is in the normal state.

duces a parallel beam. After L1, the beam is diverted using two movable mirrors, A and B. The mirrors are computer controlled, and allow the beam to be moved in two orthogonal axes, thereby allowing the whole of the sample surface to be scanned. After the mirrors, the beam passes through lens L2, and is directed into the cryostat using mirror M2. The focal lengths of the lenses are: L1:300mm; L2:150mm; L3:100mm. This set-up allows an area of $1cm^2$ to be scanned, with an accuracy of approximately $50\mu m$. The last lens, L3 focuses the laser beam onto the sample surface, to a spot diameter of between $10\mu m$ and $50\mu m$ [25].

A schematic diagram of the measurement set-up is shown in Fig.5.1.2. The laser beam is chopped, and the reference signal from the chopper is sent to the lock-in amplifier, which also receives the signal from the 2DEG (after amplification with a 1:100 transformer, or a $\times 1000$ pre-amplifier). The computer controls the scanning process, and also reads in the signal value for each point of the scan [2].

Using this method a picture can be built up of the voltage measured as a function of laser position. The images were usually obtained with a lock-in time constant of 100ms which was always less than the time that the laser spent at each point and which, for standard images of 256×256 pixels gives a measurement time of just under two hours per image. This time constant proved suitable for all but the noisiest measurements, where a time constant of 1s was required.

[2]The scanning software was developed by Ralf Wichard.

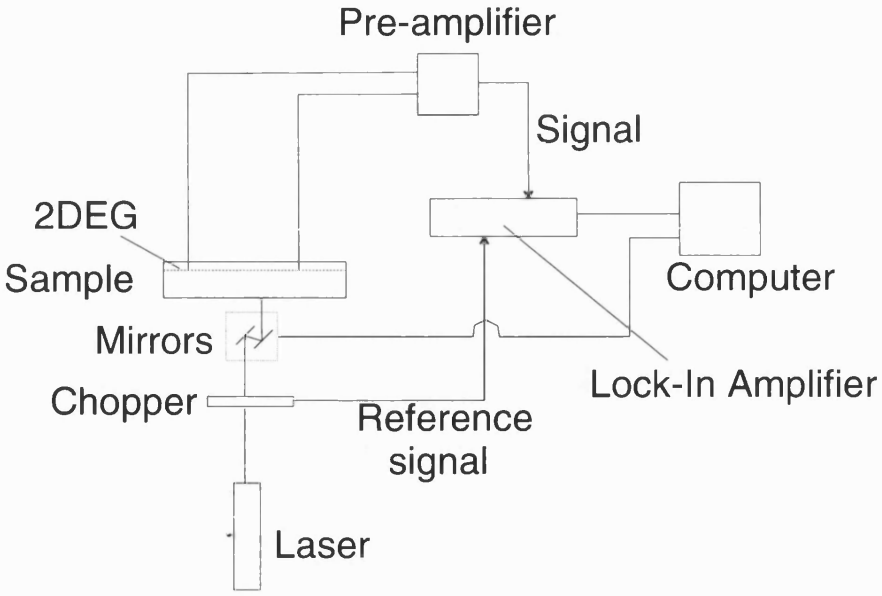

Figure 5.1.2: *Schematic diagram of the measurement set-up.*

5.2 Experimental results

Typical results of the phonon-drag imaging experiment are shown in Fig. 5.2.1A, where the phonon-drag voltage is shown as a function of laser position for sample geometry A (the geometry is shown in Fig. 4.3.1), with the voltage measured between contacts 3 and 4. The bright and dark regions depict areas of large positive and negative voltages respectively. The maximum voltage signal is $\sim \pm 50$nV. The lower part of the figure shows a line-scan across the image from $A - A'$. As can be seen, there are intense voltage signals along the [110] directions due to the strong focussing of the FTA phonons in this direction. When

the image is compared with the theoretical focussing image for a point source and a point detector, shown in Fig. 5.2.1B the agreement is seen to be quite good.

However, there are a few features of the experimental image which

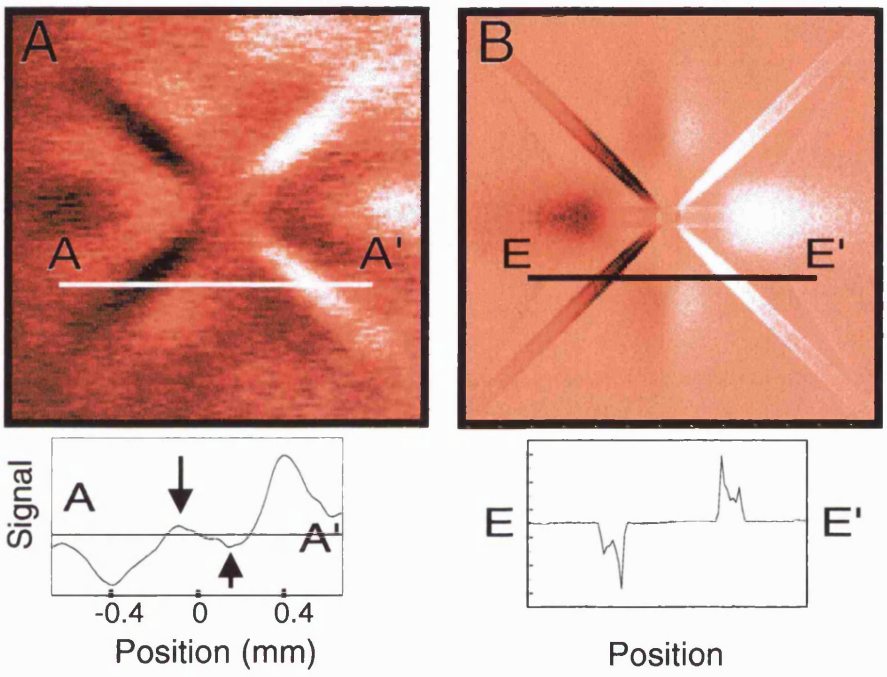

Figure 5.2.1: *A) Phonon drag image measured from a sample with geometry A. The lower part of the figure shows a line-scan from points A to A′: arrows show the position of the 'shadows' (as discussed in the text). B) Phonon drag image produced for a point source and point detector. Again, a line-scan is shown from points E – E′, showing the lack of any shadows.*

are not observed in the theoretical image. The most noticeable one is that alongside the main diagonals in the experimental image, 'shadows'

of the opposite sign occur, as can be seen more clearly in the line-scan, where these shadows are indicated by arrows. This feature does not occur in the theoretical images, as can be seen by comparing Fig. 5.2.1A with Fig. 5.2.1B.

Figure 5.2.2 shows the image measured from a sample with different sample geometry (geometry B). The geometry is shown in the lower part of the figure and consists of a hall-bar sample, width 100μm, and a circular bulge in the centre with a diameter of 1000μm. As can be seen, the image is rather complicated, and not explainable using the normal simple theory of phonon focussing. It would also appear to consist of more than one focussing structure superimposed, with displaced geometric origins.

These measurements indicate that the phonon-drag images cannot be explained by simply adopting phonon focussing theory and assuming a point detector and a point source as has been done previously. Obviously, the sample geometries, especially sample B, cannot be thought of as point detectors. In fact we show that the whole of the 2DEG is sensitive to the phonons, and will contribute significantly to the signal measured. This means that a local description of the phonon drag effect is not possible: in order to simulate the phonon-drag images seen in experiment, a model is required which takes the whole 2DEG geometry into account. This model has been described in Section 3, and the results will be described in Section 7.

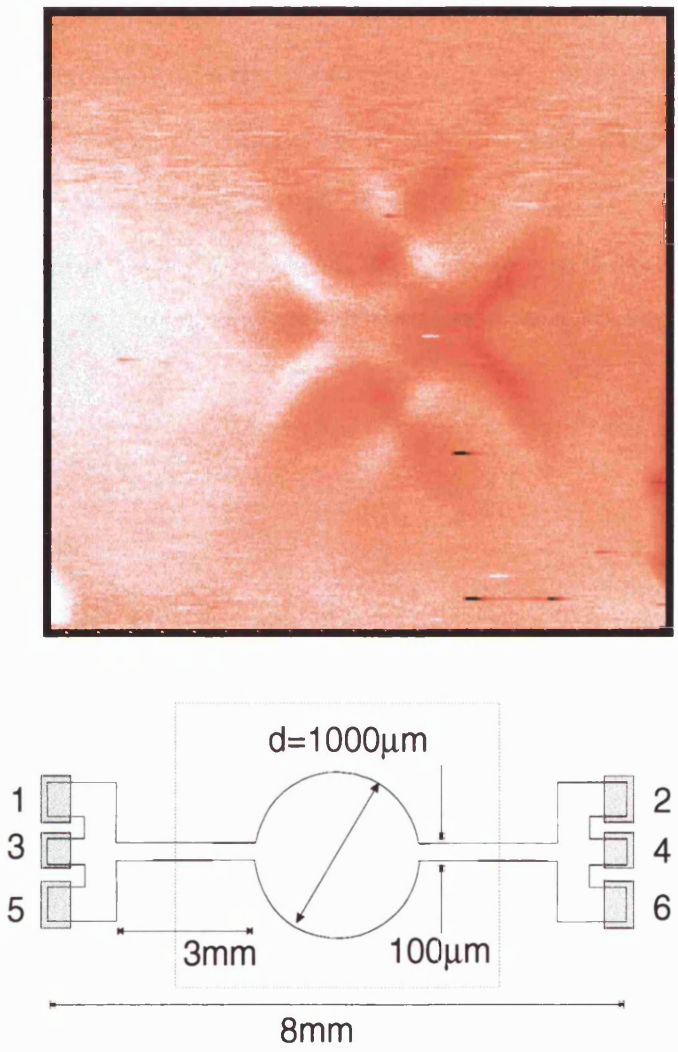

Figure 5.2.2: *Phonon drag image measured from a sample with geometry B. The lower part of the figure shows the sample geometry. The circular bulge has a diameter of* $1000\mu m$*, and the hall bar itself a width of* $100\mu m$*. The dotted square shows the experimentally scanned region.*

In addition to the measurements where the laser beam was focussed onto an aluminium film, imaging experiments have also been performed with no film on the reverse side of the sample: i.e. where the laser beam is focussed directly onto the GaAs substrate surface. Figure 5.2.3 shows such an image, measured for sample geometry A1.

Comparison of this image with the image obtained when an alu-

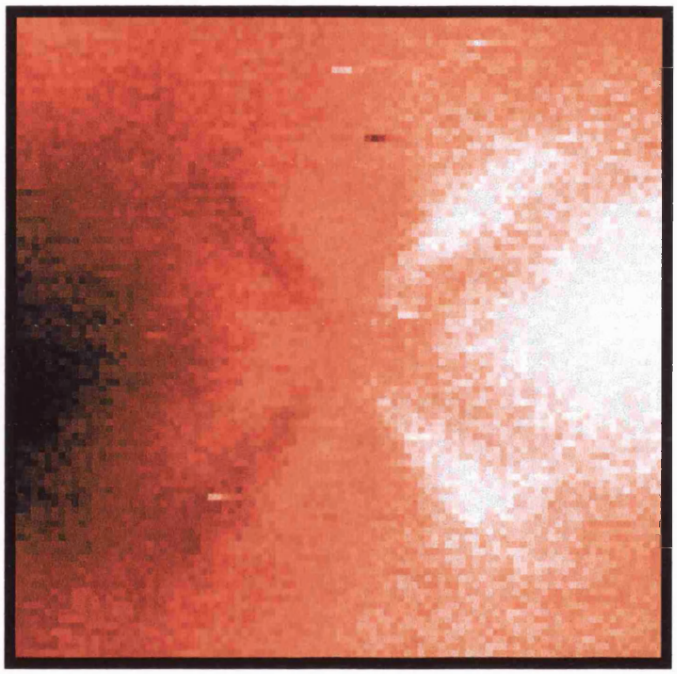

Figure 5.2.3: *Experimental image for sample geometry A1, with the laser beam focussed directly onto the GaAs substrate, and not onto an aluminium film. The main features of the previous image (Fig. 5.2.1A) can also be seen here.*

minium film was present (Fig. 5.2.1A), shows very similar features. The image from the pure GaAs surface is slightly less well focussed, and the

structures appear to be slightly more diffuse than for those with the aluminium film, which can be explained by the fact that optically excited electrons diffuse over distances of many tens of microns, thus making a larger source. Apart from the more diffuse structures, no other differences can be determined, which shows that the interface effects (at the interface between the aluminium film and the GaAs substrate) mentioned in Section 2 play only a minor role.

Although most of the measurements were performed at 1.1K when the aluminium film is in its superconducting state, Fig. 5.2.4 shows the image obtained for a measurement performed at 4.2K.

Comparison of this image with that obtained at 1.1K (Fig. 5.2.1A),

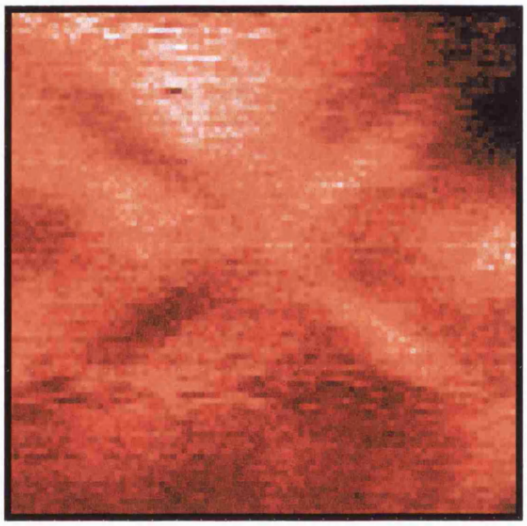

Figure 5.2.4: *Experimental image for sample geometry A, measured at 4.2K. Comparison of this image with Fig. 5.2.1A shows no qualitative differences.*

shows no qualitative differences. The noise in the measurement at 4.2K is larger than that at 1.1K since the helium is no longer superfluid, and any bubbles present will deflect the laser beam, and reduce its intensity.

Measurements were also made of the change in resistance of the samples; for these measurements, a current of 10μA was passed through the sample, between contacts 1 and 2 (see Fig. 4.3.1), and the voltage measured, as usual, between contacts 3 and 4. The resulting image is shown in Fig. 5.2.5, where the direction of current flow is indicated by the arrow. Theoretically it is to be expected that this image shows different features to those where a static voltage is measured due to the acousto-electric effect [44]. This effect means that an acoustic wave undergoes attenuation for electron drift velocities which are lower than the acoustic wave velocity, but that when the drift velocity exceeds the acoustic velocity then the acoustic wave is amplified. The current required in order that the drift velocity in the present samples is larger than the acoustic velocity is $\sim 130\mu A$. Since the current used in this measurement is only $10\mu A$ acoustic amplification is not to be expected, but instead the acoustic flux should be attenuated. Also, it would be expected that the image shows some asymmetry, since for the phonons travelling in one direction they are travelling *with* the electrons, in the other direction, however, they are travelling in the *opposite* direction to the electrons. Some asymmetry is visible in the image, for example, the two points marked with an asterix should show approximately the

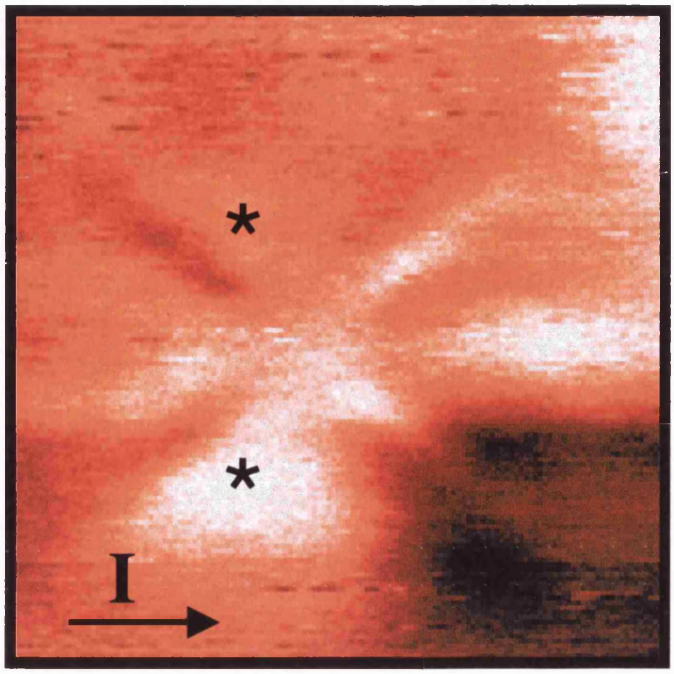

Figure 5.2.5: *Experimental image for sample geometry A, measured with a current of 10μA flowing in the direction of the arrow. No differences could be seen between this image, and those where either no current was flowing, or where the current flow was in the opposite direction.*

same voltage value, but they can be seen to be quite different, however this symmetry is not connected with the current flow, since this effect is at 90^o to the direction of current flow, but is instead probably due to optical reflections of the laser beam. No other asymmetry can be determined. The cause of the large signal at one corner of the image is not known.

5.3 Measurements on three-dimensional electron gases (3DEGs)

In addition to the measurements on 2DEGs, phonon-drag imaging was also performed on three-dimensional electron gases (3DEGs). As for the 2DEG samples, after processing, an aluminium film was evaporated onto the reverse side of the sample, and then illuminated with a laser beam. The resulting phonon-drag image is shown in Figure 5.3.1, with the voltage measured between contacts 3 and 4 (see lower part of the figure), and the area scanned indicated by the dotted square.

As can be seen, this image appears to show multiple structures: a relatively sharply focussed one is visible in the centre, and various other more diffuse structures to the left and the right of the central image. It is difficult to separate all structures and identify their origin, but when the dimensions of the image are compared to the dimensions of the sample, then it is possible to argue that the left and right structures appear to be centred around the part of the structure where the voltage probes join the main Hall bar, at the positions marked by + on the diagram. This shows conclusively that areas other than the constriction also detect phonons, and contribute to the phonon-drag signal. This means that the geometry of the sample plays a much more critical role than had previously been assumed.

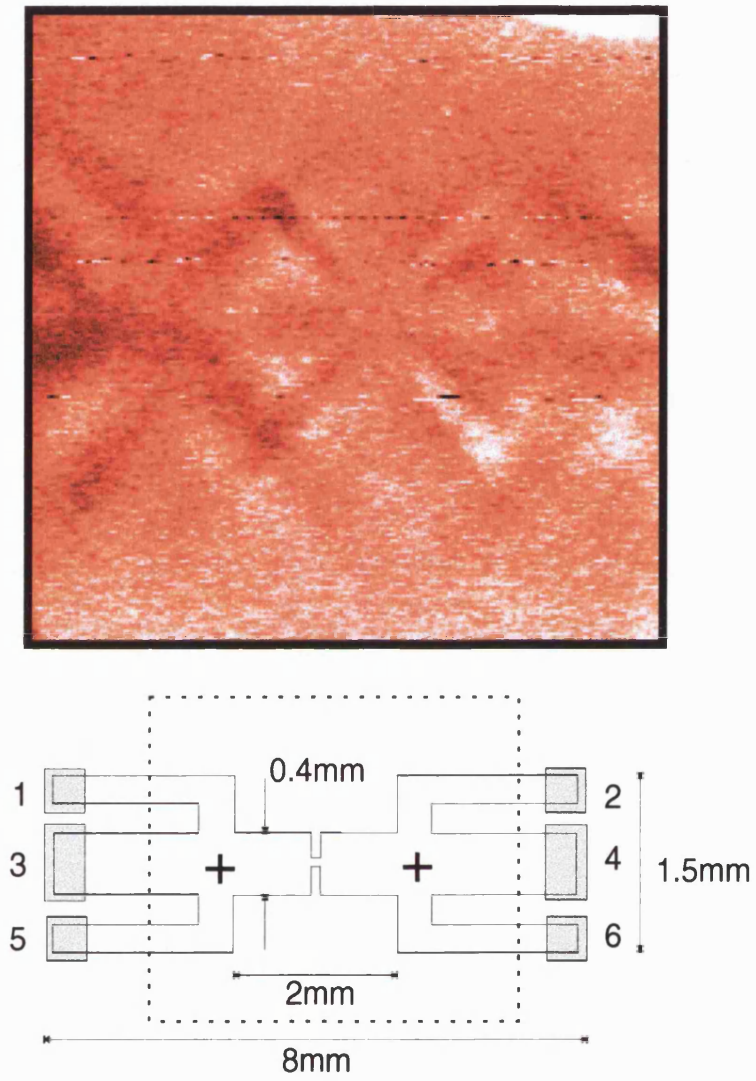

Figure 5.3.1: *Measured phonon-drag focussing image for a 3DEG sample with geometry A3, imaged over the area of the sample shown by the dotted square.*

Additional structures were seen at various positions of the geometry when the voltage was measured between different pairs of contacts. For clarity these measurements were later performed on a sample without a central constriction. Fig. 5.3.2 shows the image obtained when the voltage was measured between contacts 1 and 5. The sample geometry used is shown in the lower part of the figure, with the area scanned indicated by the dashed square. Here a large signal can be seen at the region of the contacts which will be discussed in Section 7, but in addition to this there are also extra focussing structures. Again, there appear to be multiple focussing structures with different co-ordinate origins, superimposed on one another. By comparing the dimensions of the image with the dimensions of the sample, it is possible to argue that these images are centred around the parts of the sample marked with X.

When a different pair of voltage contacts is used, the structures can be seen elsewhere on the sample. Figure 5.3.3 shows the image obtained by measuring the voltage between contacts 5 and 6 (the sample geometry and scanned area are shown in the lower part of the figure). Once again, by comparing the dimensions of the sample and the image it can be deduced that the images are centred around the areas marked by $*$. In this image it is interesting to note that the change in polarity in these phonon-drag structures occurs in the y-direction, although the voltage is measured in the x-direction.

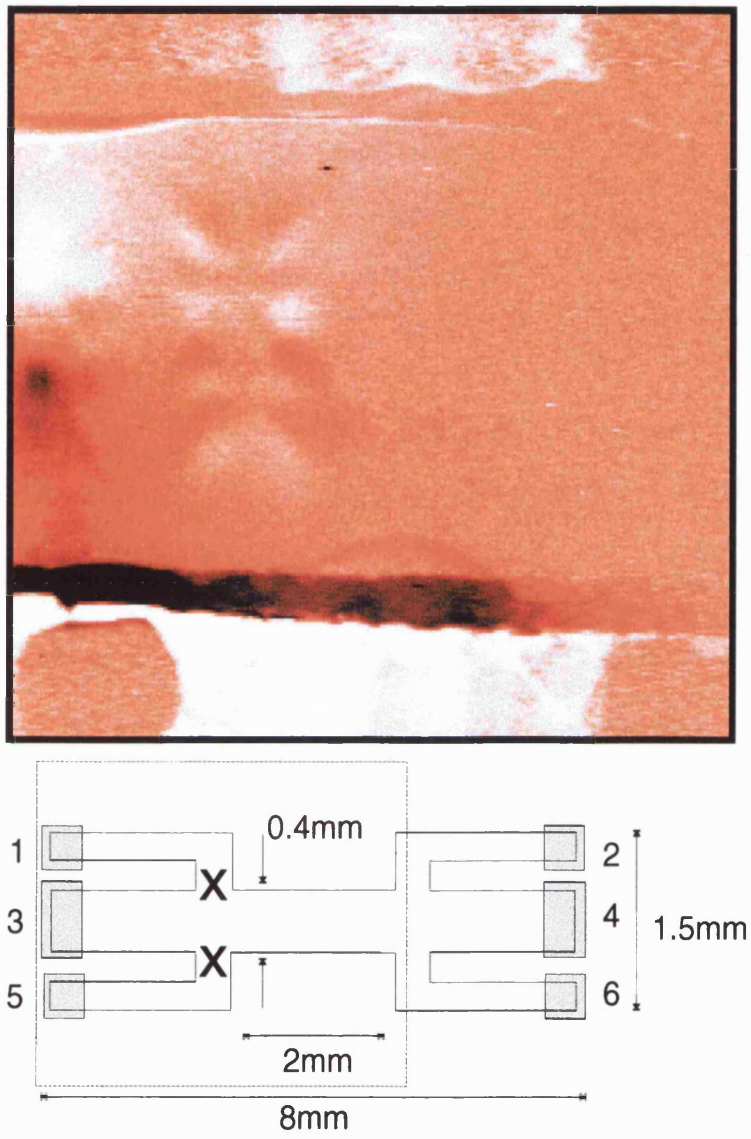

Figure 5.3.2: *Phonon drag image measured from a 3DEG sample with geometry A4, voltage measured between contacts 1 and 5. The sample geometry is shown in the lower part of the figure, with the scanned area indicated by the dashed square. X shows the possible co-ordinate origins of the focussing structures.*

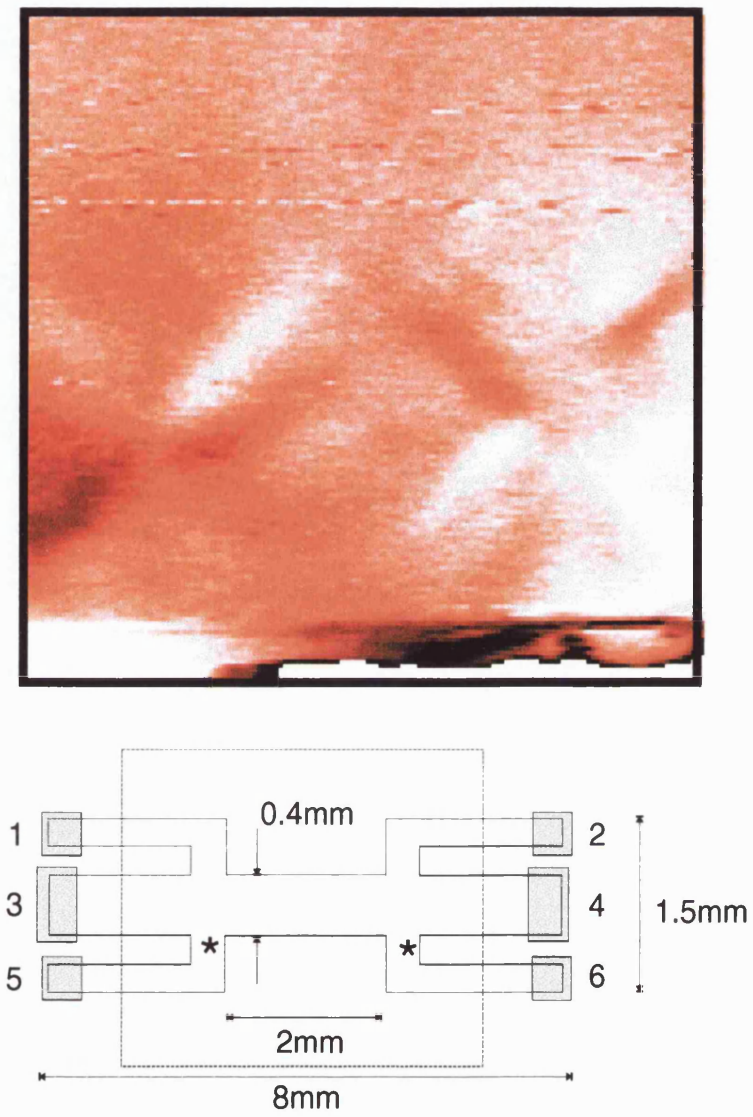

Figure 5.3.3: *Phonon drag image measured from a 3DEG sample with geometry A4, voltage measured between contacts 5 and 6. The sample geometry and the area scanned are shown in the lower part of the figure. * shows the possible co-ordinate origins of the focussing structures, obtained by comparing the dimensions of the image with those of the sample geometry.*

Such structures were not seen in the measurements on the 2DEGs which is assumed to be due to the slightly wider Hall bar used in these measurements: the Hall-bar for the 2DEG measurements had a width of 1mm, whereas for the 3DEG measurements it had a width of 0.4mm, and the voltage probes were also narrower for the 3D samples.

As these results show, the geometry of the sample can be seen to play a much more major role in the production and detail of phonon-drag images than had previously been assumed. In order to theoretically describe these images, the simple theory of phonon focussing has been modified to take the finite extent of the detector geometry into account [33]. This model has been described in Section 3, and the results of the simulations and their agreement with the experimental results will be described in Section 7.

5.4 Frequency dependence of the images.

Theoretical studies [32] have shown that the focussing images should be strongly dependent on frequency. It has previously been argued [25],[32] that the frequency spectrum of the phonons emitted from a superconducting film is peaked around the frequency of the energy gap. In the case of aluminium this would give phonons with frequencies around 120GHz. When the experimental images are compared with those theoretically obtained for frequencies of 120GHz, the agreement is reasonable [32], bearing in mind the differences outlined up till now. However, the image shown here produced at higher temperature, where the aluminium is no longer superconducting (Fig. 5.2.4) shows no qualitative differences to those obtained at low temperature by illuminating the superconducting film, although differences would be expected due to the different phonon spectra produced. One possible reason for this is that the phonon spectrum from a superconducting film is not peaked around the energy gap frequency: the assumption that the spectrum should be peaked around the superconducting energy gap arises from experiments performed by Narayanamurti and Dynes [45], where they showed that when phonons are generated by a constantan heater, and then transmitted through a superconducting film, the frequency spectrum of the phonons is peaked around a value corresponding to the energy gap. However, in the experiments presented here, the phonons are generated directly in the superconducting film, and therefore there

is no direct comparison between the experimental situations, and no reason to assume that the phonons generated in the superconductor are emitted with frequencies peaked around the energy gap.

The images obtained by direct illumination of the GaAs surface also show no difference to those obtained by illumination of the metal film, although here it is also to be expected that the phonon spectra would be different due to the different generation mechanisms involved. In the case of illumination of the metal film, there is direct excitation of the electrons in the film, which relax by the emission of acoustic phonons with a Planckian spectrum. However, when the surface of GaAs is illuminated directly this causes excitation of electron-hole pairs, which then relax by the emission of optical phonons, which decay into acoustic phonons. This leads to a phonon spectrum containing a larger proportion of high frequency phonons than obtained by illumination of the metal film [46].

More evidence for the lack of a frequency dependence can be seen in the images obtained from the 3DEG samples. As has already been stated, apart from the occurrence of extra structures, the focussing structures themselves show very little difference to those obtained from the 2DEG samples. This can be seen more easily in Fig. 5.4.1, where just the central portion of Fig. 5.3.1 is shown. Theoretically, it would be expected that this image shows different features to that from the 2DEG due to the limiting effect of the form factor. In the case of the 2DEG, the uncertainty principle causes the occurrence of the form fac-

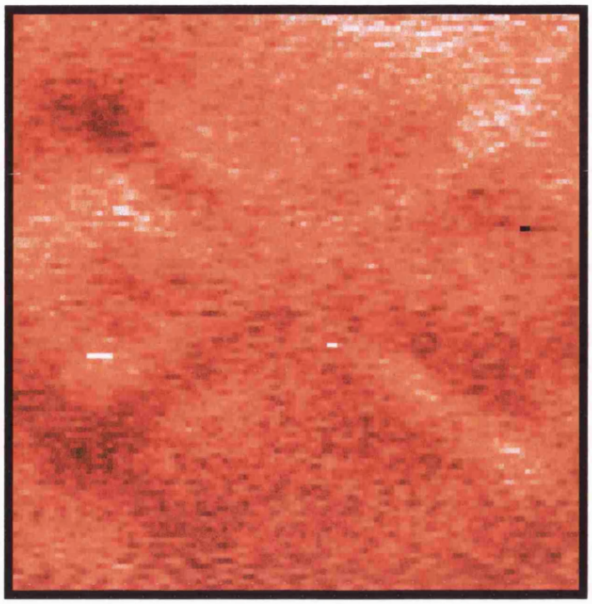

Figure 5.4.1: *Central portion of Fig. 5.3.1 showing just the phonon-drag focussing structure centred around the constriction. Although only weakly focussed, the positive and negative signals along the diagonals can still be identified.*

tor which limits phonon absorption to phonons where $q_z a \ll 1$. The absorption is also limited by the $2k_F$ cut-off which means that the parallel component of q ($q_{||}$) must be less that $2k_F$. In the case of the three-dimensional samples, the form factor no longer applies, and in this case both the parallel and perpendicular components of the wave-vector will be limited by the $2k_F$ cut-off. The value of $2k_F$ in the 3D samples leads to a maximum phonon frequency of $\sim$ 650GHz, whereas in the 2DEG samples, the form factor limits q_z to frequency values less than $\sim$80GHz, and the parallel component $q_{||}$ to frequency values less

than ~250GHz. This means that the absorption of phonons by the 2DEG is limited to those with an incident angle θ of less than $\sim 72^o$, whereas the absorption of phonons by the 3DEG can occur for all incident angles $0^o \leq \theta \leq 90^o$. Due to this difference in the limits on phonon absorption, it would be expected that there would be differences in the phonon-drag images. It would be possible that the focussing structures measured on the 3DEG samples are larger, since the phonon absorption is not limited to smaller angles of incidence, and therefore phonons with large incident angles could be absorbed.

The lack of any frequency dependence of the images is assumed to be due to the very broad phonon spectrum that is emitted by local laser excitation of the aluminium film or GaAs surface, which is too broad to resolve frequency dependent features. However, this is not completely understood.

Chapter 6

Frequency resolved phonon-drag measurements

Using superconducting tunnel junctions as generators of quasi-monochromatic acoustic phonons, as described in Section 2, it is possible to perform phonon-drag spectroscopy on 2DEGs [10]. In this section the details of such experiments will be described, along with the experimental results which were obtained.

6.1 Preparation of superconducting tunnel junctions

The superconducting tunnel junctions are prepared by thermal evaporation of the metal films in high vacuum. Metal masks are used which

are placed within 50μm of the substrate in order to define the film areas. These are magnetically controlled, which enables the masks to be changed without breaking the vacuum. The tunnel junctions consist of two metal films, one over the other, which are separated by a layer of insulating oxide, of approximately 10-20Å thickness. The metal used in these experiments is a mixture of 10:1 lead: bismuth, although tunnel junctions can also be made from aluminium, tin, or indium. The mixture of lead and bismuth is used because the addition of bismuth reduces the occurrence of 'whiskers' penetrating the oxide which is a problem in pure lead junctions, and has the advantage of a much sharper energy gap than pure lead junctions [47]. The metal is evaporated from tungsten boats, under a base pressure of approximately 1×10^{-5} mbar. The thickness of the films and the rate of evaporation is determined using a quartz crystal monitor. The PbBi films are evaporated with a rate of 50Å/s to a thickness of 1500Å. After evaporation of the first film, the vacuum chamber is opened to air, the sample removed and placed in an oven at $\sim 57^{o}$C for 30 minutes in order to form the oxide layer. The sample is then returned to the vacuum chamber, pumped down to the required pressure, and the second film is evaporated, using the same rate and thickness as for the first film. The geometry of the tunnel junctions used is shown in Fig. 6.1.1.

The energy gap of the tunnel junctions prepared by this method is $\sim$ 3meV, and the active junction area is designed to be $\sim 0.2 \times 0.2$ mm^2. The contacts to the tunnel junction are made using miniature

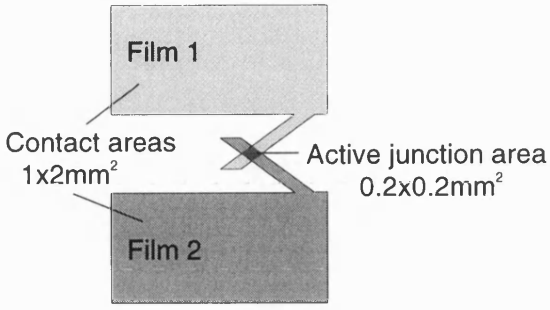

Figure 6.1.1: *Geometry of the superconducting tunnel junctions used.*

copper/beryllium springs, which are coated with indium to produce a superconducting contact, and pressed onto the contact areas of the tunnel junction. This means that a two-point contact geometry is sufficient, although a four-point geometry has also been used. The contacting of the superconducting tunnel junction does however give rise to some problems. As was mentioned earlier, in this work it is necessary to make contacts to both the 2DEG and the tunnel junctions. The 2DEG contacts are made by bonding to the contact pads with gold wire; the contacts to the tunnel junction are made, as mentioned above, by using indium-coated copper/beryllium springs, pressed onto the surface of the films. However, the fact that these contacts are made with a small amount of pressure can lead to damage of the 2DEG, or, if the force is uneven, the sample may move slightly, and the bond wires to the 2DEG will be broken. This makes the successful contacting of both sides of the device rather complicated. In other experiments, where aluminium tunnel junctions have been used, these can be bonded in a

similar fashion to the 2DEG contacts, and the problems are less severe [48].

6.2 Experiment

The tunnel junction is evaporated onto the opposite face of the sample to the 2DEG. The active junction area is displaced from the centre of the sample, as shown in Figure 6.2.1, in order that the phonons travel along the [111] direction towards the central constriction in the sample geometry. The geometry of the 2DEG sample is shown in Figure 4.3.1. The bias on the superconducting tunnel junction is swept up to $\sim 6mV$, and a voltage modulation of $\sim 0.2mV$ is applied onto the DC voltage at a frequency of $\sim$ 70Hz. The phonon signal on the 2DEG is detected with a lock-in amplifier at the frequency of the modulation. A schematic of the experimental set-up is shown in Figure 6.2.2, and is based on the technique first demonstrated by Lega [10].

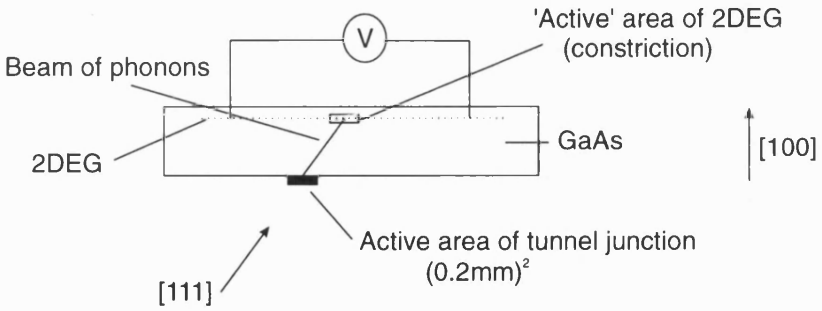

Figure 6.2.1: *Diagram showing position of the superconducting tunnel junction with respect to the active area of the device.*

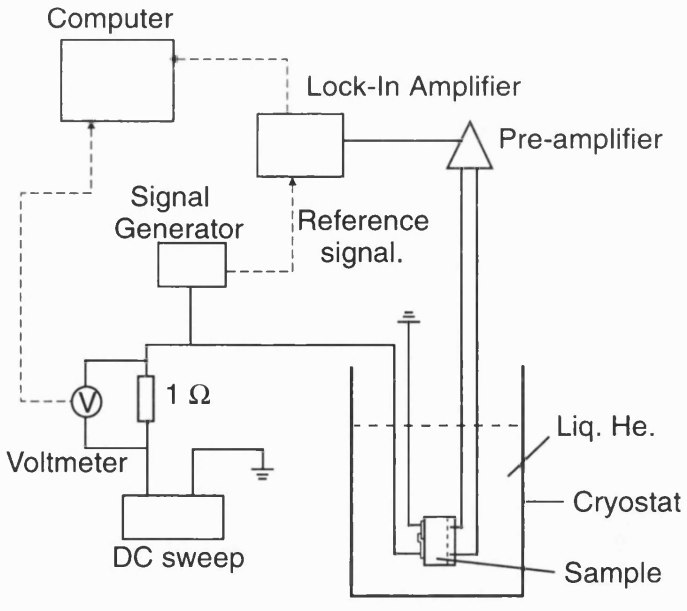

Figure 6.2.2: *Schematic of the experimental set-up.*

6.3 Experimental results

The monochromatic phonons produced by the superconducting tunnel junction travel ballistically across the sample and interact with the 2DEG. This interaction causes a voltage to be set up, due to the phonon drag effect described in Section 2.7, which can then be measured either directly or, with a current flowing, as a change in resistance. By measuring the voltage on the 2DEG as a function of bias voltage on the superconducting tunnel junction, at $\sim$ 1.1K, plots are obtained of the phonon absorption by the 2DEG as a function of phonon frequency. Figure 6.3.1 shows a set of three curves obtained from such a measurement. As can be seen, the signal experiences an initial sharp rise, falls

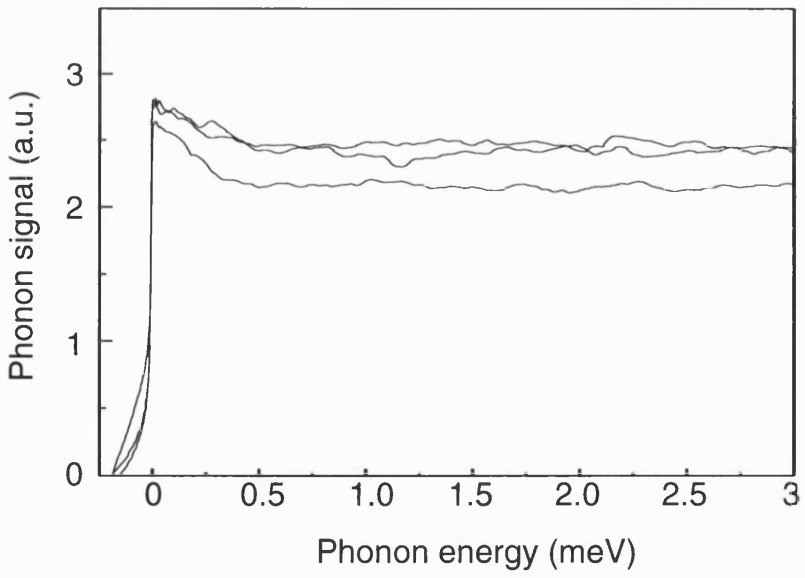

Figure 6.3.1: *Experimental curve measured on #8045/10.*

off slightly, and then remains constant to higher frequencies. A roll-off due to the form factor, or a reduction in the signal due to the $2k_F$ cut-off cannot be determined. Figure 6.3.2 shows another set of curves measured from the same sample, with the same superconducting tunnel junction. As can be seen, here there is also an initial increase of the signal, which reaches a maximum around 0.75meV, and then suffers a cut-off. The second set of curves is comparable with those obtained in

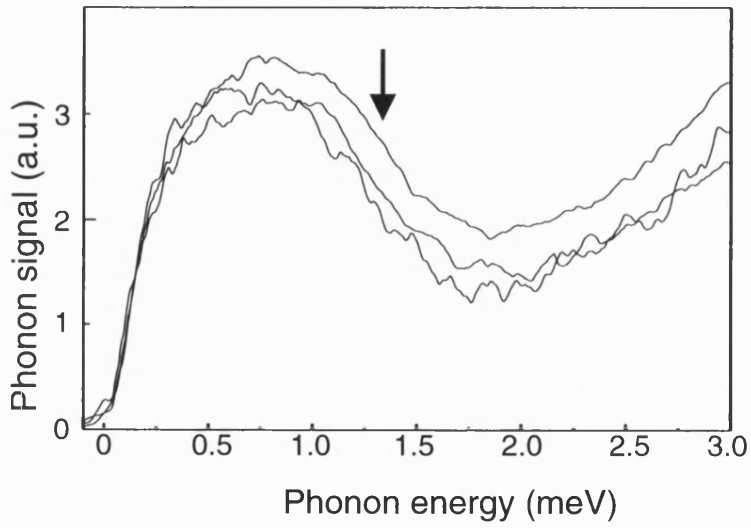

Figure 6.3.2: *Experimental curve measured from #8045/10 showing a cut-off feature at ~1.3meV, indicated by the arrow.*

previous measurements [10], and also with the theoretical predictions [32]. The form of the curves can be explained by the effect of the $2k_F$ cut-off. The value of $2k_F$ for the samples used gives a frequency cut-off value of ~310GHz, which occurs at a phonon energy of ~1.3meV, which is approximately given by the mid-point of the cut-off observed in the

experimental curves. The signal rise that occurs at higher voltages is probably due to broad band phonons which are emitted from the junction along with the monochromatic phonons and was also seen in the previous measurements [10]. However, there remain a large number of unanswered questions. The main point is that the curves shown in Fig. 6.3.2 were only obtained on a few occasions; the majority of the curves had the form shown in Figure 6.3.1. There are a number of possible reasons for this, which will be discussed in the next section.

6.4 Discussion

The first possible reason for these differences is that the signal seen in Fig. 6.3.1 (from now on referred to as Type A) is due to a large cross-talk between the voltage on the tunnel junction and the 2DEG. This would appear to be the most probable explanation, since the sudden increase in phonon signal at low frequencies is too steep to be due to phonons. Further analysis of the curves shown in Fig. 6.3.1 would seem to indicate that there is a phonon signal superimposed onto the cross-talk, which is of opposite sign. By subtracting the cross-talk signal, and changing the sign of the signal, the curve shown in Fig. 6.4.1 is obtained (from one of the curves of Fig. 6.3.1). It would appear that this curve is similar to those shown in Fig. 6.3.2, since the signal increases as the

phonons start to be emitted from the tunnel junction. However, the noise level is too large to allow the determination of a cut-off frequency, and the signal is much smaller than that of Fig. 6.3.2. The other two curves from Fig. 6.3.1 do not result in curves which resemble those of Fig. 6.3.2, even when the signal due to the cross talk is removed. All experimental attempts to reduce this cross-talk remained unsuc-

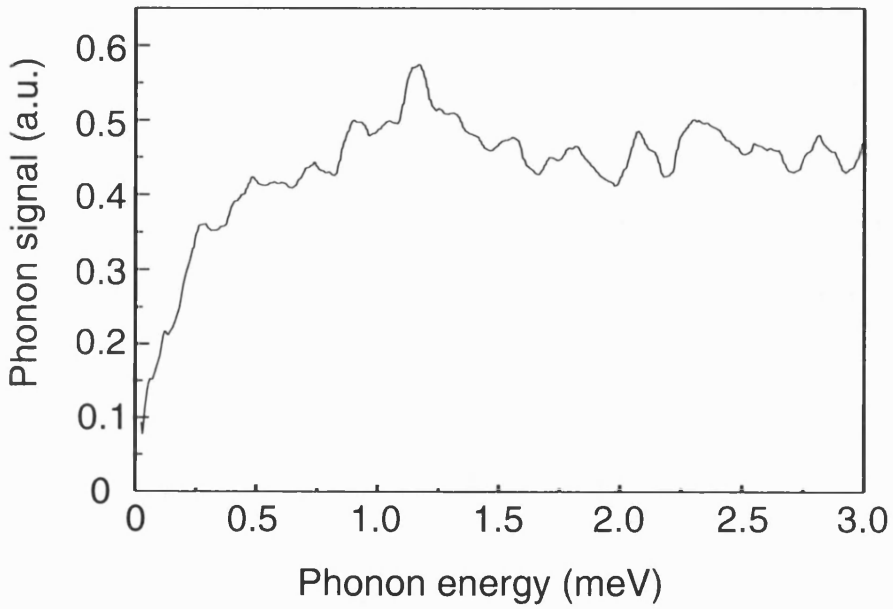

Figure 6.4.1: *Experimental curve measured on #8045/10, with the signal due to the cross talk removed, and the sign of the signal reversed.*

cessful. The other point to bear in mind is that the curves shown in Fig. 6.3.2 (Type B) were obtained using the same experimental set-up as the Type A curves, and there should therefore be no large differences in the amount of cross-talk in the measurements.

The second possible factor is that the positioning of the tunnel junctions so that the phonons travel along the [111] direction to the constriction in the 2DEG is not accurate enough. However, since both types of curve were measured on the same sample, with the same tunnel junction, and therefore the same geometry, this cannot account for these differences. Also, it would then be expected that the signal showing no evidence of the $2k_F$ cut-off would be smaller since here the phonon intensity is reduced. However, the intensities of both types of curve are comparable, and therefore further rule out such an effect.

Another reason could be that the high frequency phonons created at the tunnel junction do not reach the 2DEG. This could be caused by a number of effects. The high frequency phonons could down-convert before reaching the 2DEG, and therefore although high frequency phonons are generated, only low-frequency phonons would reach the detector. However, the experimentally obtained values of the mean-free path of phonons in such samples has been determined to be around 0.4mm for 1THz phonons (see Section 2.1). This value will be much larger for lower frequency phonons and there is therefore no reason why phonons with frequencies around 500 GHz should not reach the detector. Other effects that could stop high frequency phonons from reaching the detector would be reabsorption inside the films of the tunnel junction, or scattering at the film-substrate boundary. The phonon reabsorption mean free path has been measured as being 2100Å for longitudinal phonons and 770Å for transverse phonons in Pb [49] (which will be used as approx-

imate values for PbBi). The thickness of the films used in the present experiments was 1500Å, which would indicate that a large proportion of the longitudinal phonons should be emitted without any reabsorption. The other factor is scattering at the film-substrate boundary. Trumpp and Eisenmenger [50] have studied these features, and have shown that there are large phonon losses at the boundaries, but they do not indicate whether these losses have a pronounced frequency dependence, which would be necessary to explain the effects observed here.

One further point to be considered is the effect of the form factor. As previously stated, the $2k_F$ cut-off should occur for these samples at phonon frequencies of $\sim$ 310GHz. However, if we consider the effect of the form factor, we can see from Fig. 2.5.2 that for a lateral 2DEG thickness of $\sim 12.5nm$, and an incident angle of 55^o the form factor causes the phonon absorption to be reduced to very small values above frequencies of between 150GHz and 200GHz, and that at frequencies around 300GHz the phonon absorption is very small. Therefore at frequencies where it should be possible to observe the $2k_F$ cut-off the signal should already have suffered a roll-off due to the form-factor.

The final point to be considered is whether the modulated phonon spectrum from PbBi tunnel junctions is truly monochromatic. Berberich and Schwarte [51] used the stress-tuned splitting of the acceptors in silicon to study the phonon spectrum emitted from various tunnel junctions. In these experiments, the splitting of the acceptor states in silicon is varied linearly by the application of uniaxial stress. This leads to a

resonant absorption of phonons at the energy of the separation of the states, which is seen as a reduction in the transmitted phonon signal. The measurements use a superconducting tunnel junction as generator of quasi-monochromatic phonons on one side of the crystal, and a detector on the other side. By sweeping the stress applied to the sample, the splitting is linearly increased, and one can obtain curves of phonon transmission as a function of stress. The stress applied can then be linearly related to the energy of the splitting, and thus to the energy of the resonantly absorbed phonons. Their results show that the spectra from PbBi tunnel junctions are to a large extent non-monochromatic, and that there are large signals at subharmonics of the bias voltage. A set of results from their experiments for PbBi tunnel junctions is shown in Fig. 6.4.2. Here it can be seen that at energies lower than the bias voltage there is a large phonon signal, which is also bias dependent (shown by the arrows in the figure). This would mean that in addition to the detection of the signal with an energy corresponding to the bias voltage, a large signal from lower frequency phonons would also be detected.

However, all the features mentioned above could be used to explain why the signal did not show the expected form, but they would then be expected to occur all the time, and can therefore not explain why the signal, on occasion, showed the expected form. As a result of this, it has not been possible to ascertain the reason for the two types of curve measured, and therefore further phonon-drag spectroscopy measurements on other low-dimensional electron systems were not undertaken.

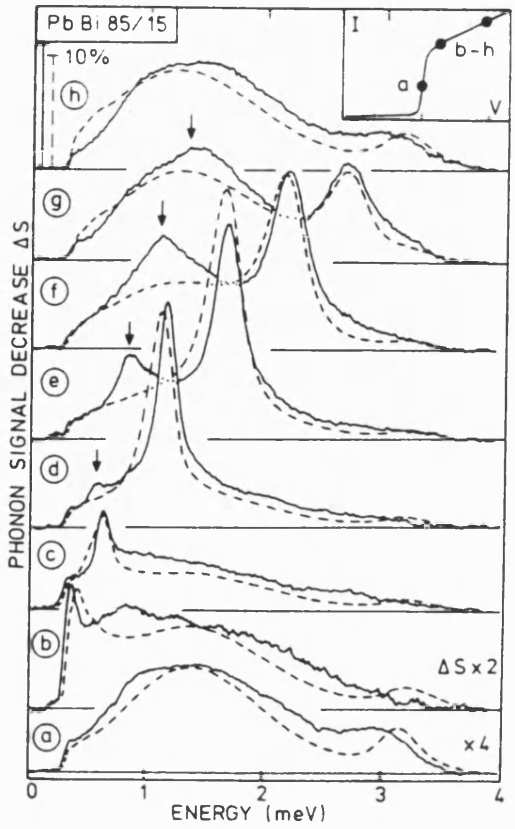

Figure 6.4.2: *Experimental phonon spectrum emitted from a PbBi tunnel junction, measured using the stress-tuned splitting of the acceptor states in silicon. From [51]. The y-axis shows the phonon signal decrease ΔS, which is a representation of the emitted phonon spectrum. The curves are measured for different values of bias voltage on the tunnel junction: a-h: 3.13, 3.53, 3.78, 4.28, 4.78, 5.28, 5.78, 6.28mV The value of the quasi-monochromatic peak then occurs at $eV_0 - 2\Delta$, where $2\Delta \sim 3meV$. The modulation used was δI=8mA.*

Chapter 7

Discussion

In this section the results of the calculations outlined in Section 3 will be discussed together with some new experimental results which illustrate the agreement between model and experiment. The majority of the calculations were performed on a 400×100 site lattice corresponding to real dimensions of 4mm$\times$1mm, where the voltage is measured along the length of the sample. This is in contrast to the samples used for the experiments which were nominally of the same width, but up to 8mm long. This gives rise to some small quantitative differences, but does not affect the extent of the agreement within the experimental errors. The samples for the simulations were made shorter than those used in experiment to make the computer run times acceptable. All constrictions (when present) were positioned in the centre of the sample.

7.1 The response function

The response function $\Delta V_{i,j}$ was defined in Section 3 as being the voltage measured between the ends of the sample as a function of the position of the local charge dipole. The response function was calculated separately for the $x-$ and $y-$components, i.e. for local charge dipoles directed in either the $x-$ or the $y-$ directions. The results of the response function calculation for the geometry A2 is shown in Fig. 7.1.1, for the $x-$component and in Fig. 7.1.2 for the $y-$component [1].

For Fig. 7.1.1, the results for the $x-$component, the co-ordinate gives the position of the local dipole and the colour scale shows the magnitude of the voltage signal between the ends of the sample: in this case, zero signal is denoted by the dark regions, and a strong signal is denoted by white areas. Fig. 7.1.2 shows the result for the $y-$component. Here a large positive signal is denoted by bright regions, and large negative signals by dark regions. The signal here is approximately one order of magnitude smaller than the signal for the $x-$component. If we initially consider the result for the $x-$component, it can be seen that, as had previously been suggested [25], the constriction produces a signal which is much larger than the signal from the remainder of the sample.

[1] The potential distribution for individual charge dipoles is shown in more detail in Appendix A. The images shown here in Figures 7.1.1 and 7.1.2 are obtained directly from the images shown in Appendix A, by calculating the average voltage at each end of the sample, and thereby the voltage difference, for all dipole positions, and plotting this voltage as a function of position.

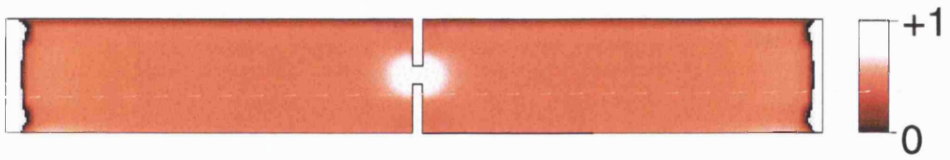

Figure 7.1.1: *Results of the response function calculation for the sample geometry A2, for a local dipole orientated in the x−direction. The coordinate shows the position of the local charge dipole and the colour scale gives the magnitude of the voltage signal measured between the ends of the sample. Large signals are denoted by intense white areas, and small signals by dark regions.*

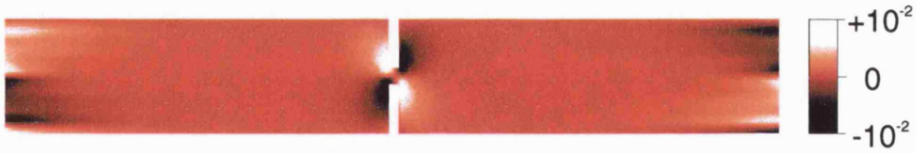

Figure 7.1.2: *Results of the response function calculation for the sample geometry A2, for a local dipole orientated in the y−direction. The coordinate shows the position of the local charge dipole and the colour scale gives the magnitude of the voltage signal measured between the ends of the sample. Large negative signals are denoted by dark areas, and large positive signals by white areas.*

However, the signal extends over an area much larger than just the area of the constriction. It should also be noted that there is a large signal at the ends of the detector, which will be discussed in more detail later. When the $y-$component is considered, it can be seen that around the constriction there is also some fine structure, which changes sign; it will be shown that this fine structure is responsible for the appearance of fine structure in the final phonon-drag images. From these images it can be appreciated that any variations in sample geometry have an effect over a distance of $\sim 250\mu m$, but at larger distances the geometry changes are no longer noticeable. This justifies the fact that the simulated sample geometries were shorter than those used in the experiments; it can be appreciated that if the sample was made twice as long, the difference in the final result would in this case be negligible, since the length is larger than this critical distance of $\sim 250\mu m$. These response function images are then convoluted with the respective phonon focussing image, as described in Section 3, to give the final result. These images will be described in the following section.

7.2 Comparison of simulated and experimental results

Figure 7.2.1A shows the results for a sample with a small rectangular constriction ($(50\mu m)^2$) in the centre (sample A2), using just the con-

tributions from the deformation potential. Only the central part of the image is shown, with the respective part of the sample geometry superimposed onto the image. When this is compared with the experimental image obtained for sample A1, which for convenience is shown in Fig. 7.2.1B, it can be seen that there is very little agreement, confirming that the deformation potential interaction is not predominantly responsible for the electron-phonon interaction in this situation, as has previously been shown [9]. It is for this reason that the contributions from the deformation potential have been neglected in all other calculations.

Figure 7.2.2 shows the results of the calculation for the x-component

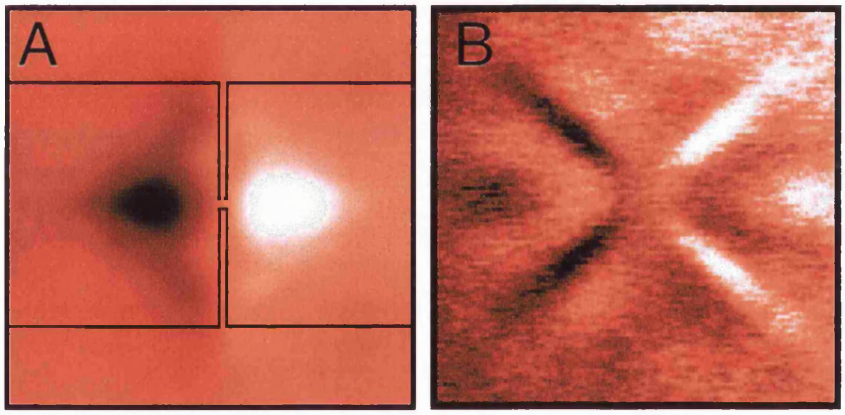

Figure 7.2.1: *A) Results of the simulation for the sample geometry A2, taking only the contribution from the deformation potential into account. The relevant section of the simulated geometry is superimposed onto the image. B) Experimental image for the sample geometry A1. Comparison of the two images shows that the interaction due to the deformation potential cannot explain the experimental images.*

(i.e. dipoles directed parallel to the x-axis), taking just the piezoelectric interaction into account. Just the central portion of the image is shown, depicting the area around the constriction. Figure 7.2.3 shows the corresponding image for the $y-$component. As can be seen, in the image for the y-component, there is a large amount of fine structure around the constriction, but the intensity of the signal is at least one order of magnitude smaller than that for the x-component. To obtain the final result, the images due to the x- and y-components are superimposed.

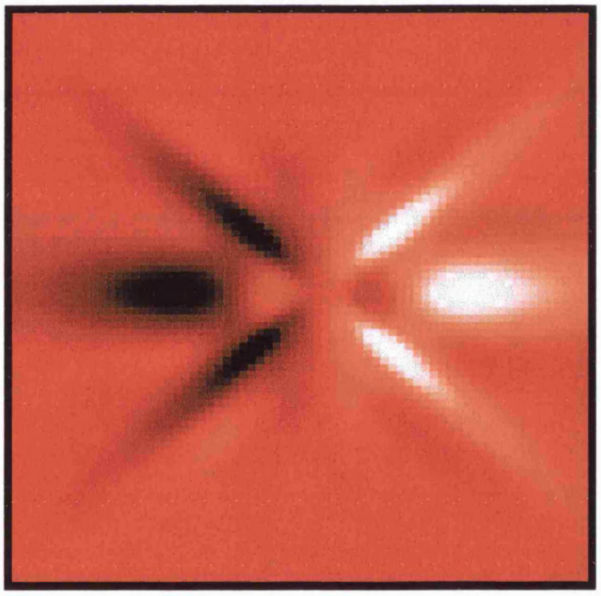

Figure 7.2.2: *Results of the simulation for the sample geometry A2 taking only the piezoelectric interaction into account, for dipoles directed parallel to the x-axis.*

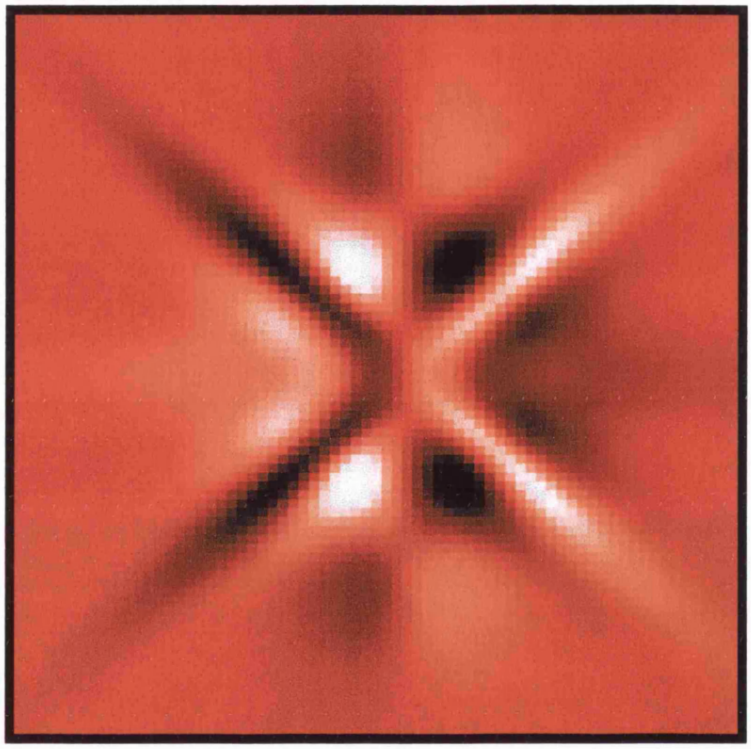

Figure 7.2.3: *Results of the simulation for the sample geometry A2 taking only the piezoelectric interaction into account, for dipoles directed parallel to the y-axis.*

Figure 7.2.4A shows the results of the superposition of the x- and y-components, when just the contributions from the piezoelectric interaction are considered. The experimental image is also shown for ease of comparison (Fig. 7.2.4B).

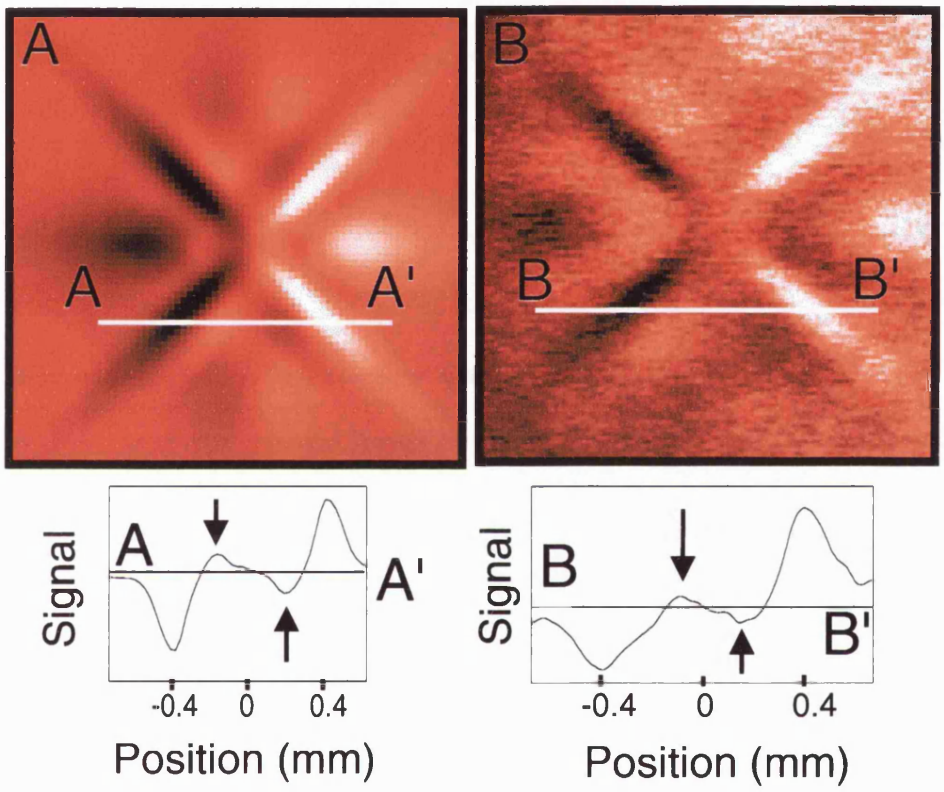

Figure 7.2.4: *A) Results of the simulation for the sample geometry A2 taking only the piezoelectric interaction into account. A line-scan is also shown, through points $A - A'$. B) The experimental image for the same sample, also showing a line-scan through the image from $B - B'$. Comparison of the two images and line-scans shows excellent agreement.*

Here the agreement can be seen to be excellent. Closer comparison of the images shown in Figure 7.2.4 shows that the model reproduces the features of the experimental images exceptionally well. A new feature of this model is that it successfully predicts the occurrence of 'shadows' on either side of the main diagonals, which can be seen more clearly in the line-scan through the calculated image. When this line-scan is compared with that from the experimental image the agreement can be seen to be outstanding. The relative intensities of the main peaks and the shadows also show very good agreement. This effect can not be explained when the finite geometry of the sample is not taken into account.

Fig 7.2.5A shows the simulated image for a different sample geometry (B2) which has a bulge which is 1000μm long and 1000μm wide. The sample geometry is shown in the lower part of the figure. The corresponding experimental image (sample B1) is shown in Fig 7.2.5B. The agreement can be seen to be very good. The fact that the experimental measurements were performed on a sample where the bulge was circular, and the simulation was for a square bulge arises mainly from the need to define the boundary conditions for the simulation, which is easier for straight lines. However, in practice this has very little effect, because the potential within the geometry tends to smooth out the sharp corners in the simulation.

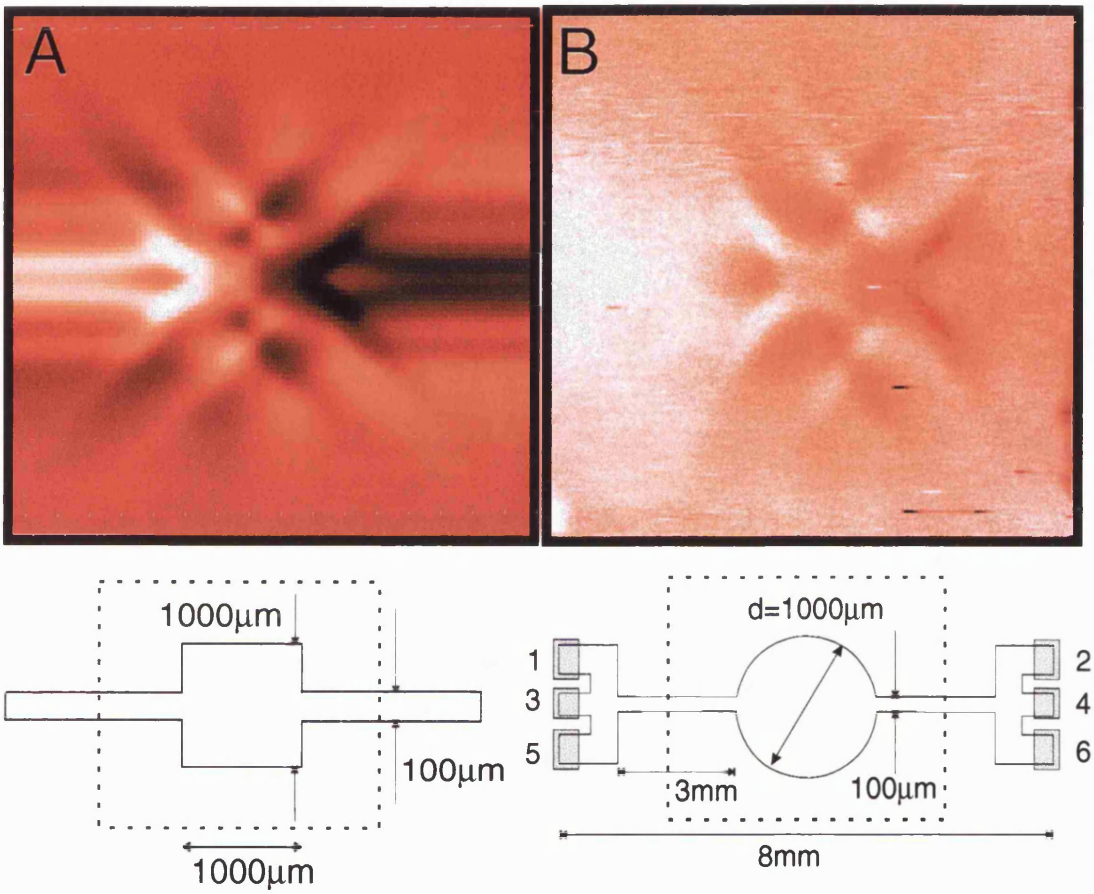

Figure 7.2.5: *A) Simulated image for the sample geometry B2. The lower part of the figure shows the sample geometry B2. B) Experimental image for the sample geometry B. The scanned area is shown by the dotted square in the lower part of the figure, which shows the sample geometry B.*

This can be seen in Fig. 7.2.6 where the response function $\Delta V_{i,j}$ is plotted as a function of charge dipole position (before convolution with the focussing structure): i.e. the coordinate gives the charge dipole position, and the colour scale gives the voltage measured between the sample ends for the charge dipole at that position, with dark regions depicting areas of large signal, and white areas regions of small signal.

As can be seen, although the bulge is defined by the boundary

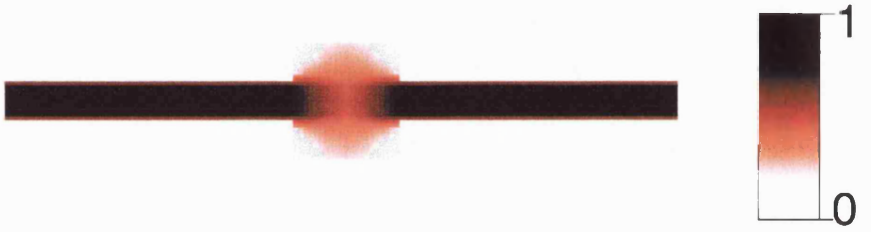

Figure 7.2.6: *Response function $\Delta V_{i,j}$ for sample B2, showing that the bulge is effectively rounded. Dark regions depict areas where the charge dipole gives rise to a large voltage signal: light areas show where the charge dipole produces only a small or zero signal. Although the geometry defined by the boundary conditions is rectangular, the response function is rounded.*

conditions to be rectangular, when the dipole is situated at the corners of the bulge, the voltage measured between sample ends is small, and contributes little to the result.

Fig. 7.2.7A shows the simulated image for a similar sample geometry (C2) with smaller dimensions, which has a bulge which is 500μm long and 500μm wide. The sample geometry is shown in the lower part

of the figure. The corresponding experimental image (sample C1) is shown in Fig. 7.2.7B. It can clearly be seen that the agreement is very

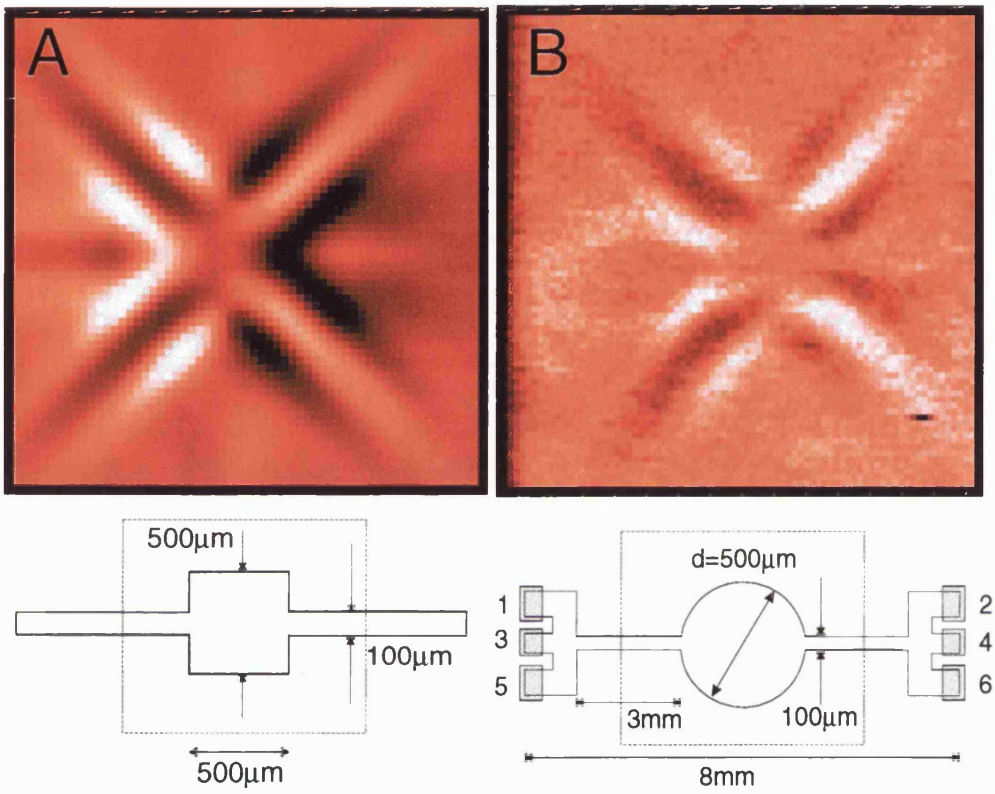

Figure 7.2.7: *A) Simulated image for the sample geometry C2. The lower part of the figure shows the sample geometry C2. B) Experimental image for the sample geometry C1. The scanned area is shown by the dotted square in the lower part of the figure, which shows the sample geometry C1.*

good.

The agreement for geometries A, B and C can be seen to be excellent. To further test the validity of the model, additional sample

geometries were both simulated and measured.

Figure 7.2.8 shows the experimental image obtained from sample D1, with the sample geometry shown in the lower part of the figure. The geometry consists of a long bulge, of length 1mm and width 0.5mm. As can be seen, there are now two focussing structures, centred around each end of the long bulge. A line-scan through one of these structures from $C - C'$ is also shown. The simulation has been carried out for a similar sample geometry (D2) and the result is shown in Fig.7.2.9, with the sample geometry illustrated. A line-scan through a single focussing structure is also shown, from $D - D'$. Comparison of the experimental and theoretical images, (Figs. 7.2.9 and 7.2.8) shows the agreement to be excellent.

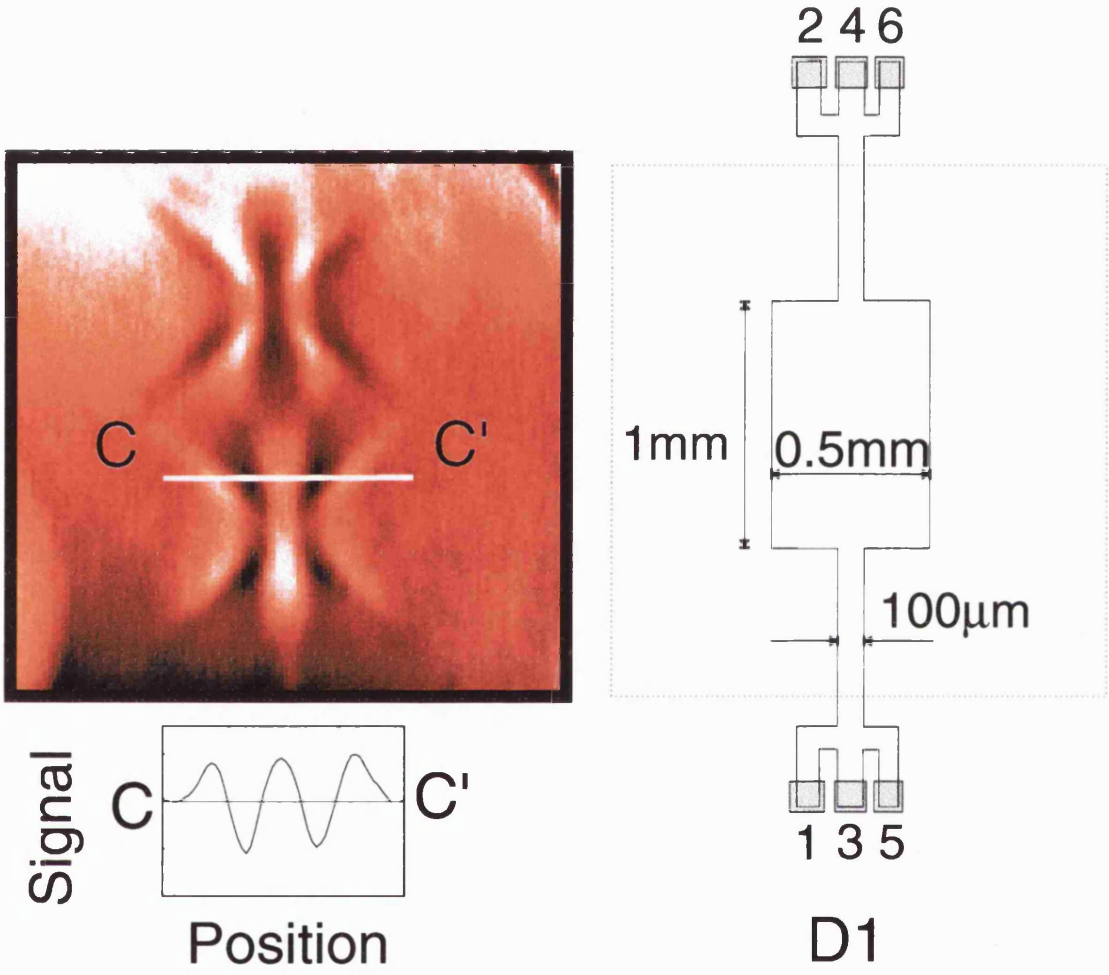

Figure 7.2.8: *Experimental image for the sample geometry D1. The signal is measured between contacts 3 and 4. The lower section shows the line-scan through the image, from points $C - C'$. The sample geometry is also shown, with the scanned area indicated by the dotted square.*

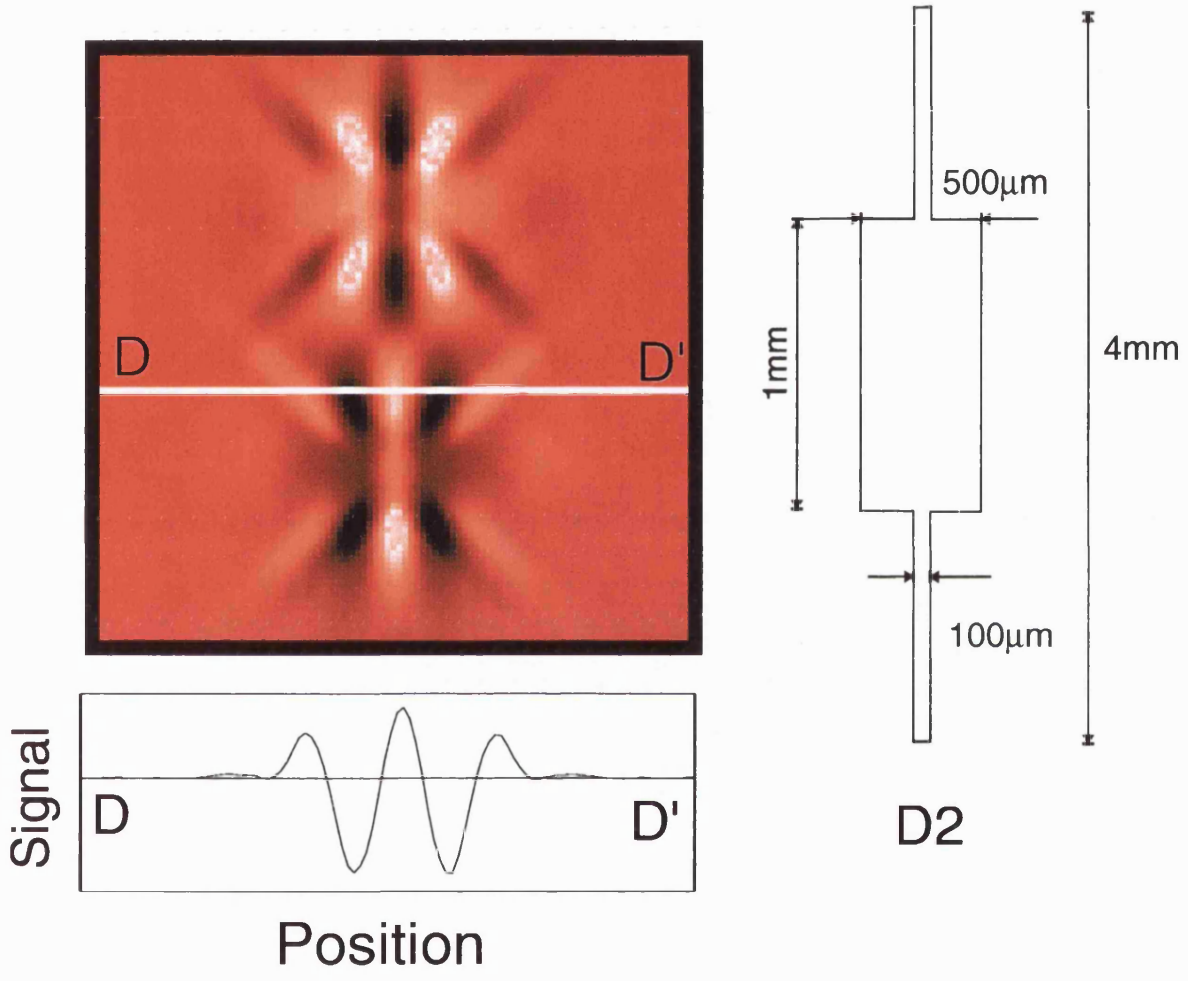

Figure 7.2.9: *Simulated image for the sample geometry D2. The lower section shows the line-scan through the image, from points $D - D'$. The simulated geometry is also shown.*

Figure 7.2.10 shows the experimental image obtained for sample E1, with the sample geometry indicated in the lower part of the figure. This image shows that it is not necessary to have large differences in the dimensions of the sample in order for spatially resolved detection to be possible.

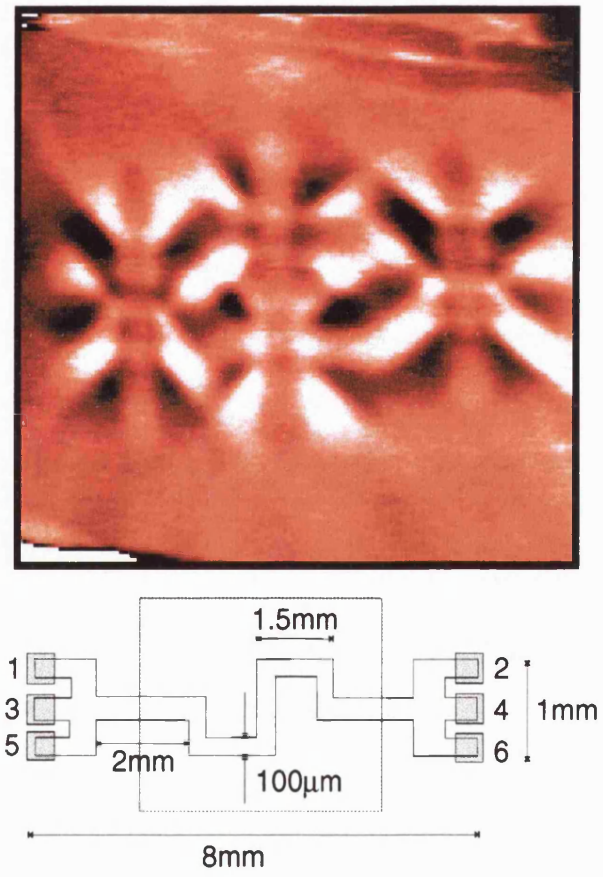

Figure 7.2.10: *Experimental image for the sample geometry E1: the geometry is shown in the lower part of the figure*

The simulated image for such a geometry is shown in Fig. 7.2.11. By comparing the two images, it can again be seen that, even for such relatively complicated geometries the agreement between simulated and experimental images is very good.

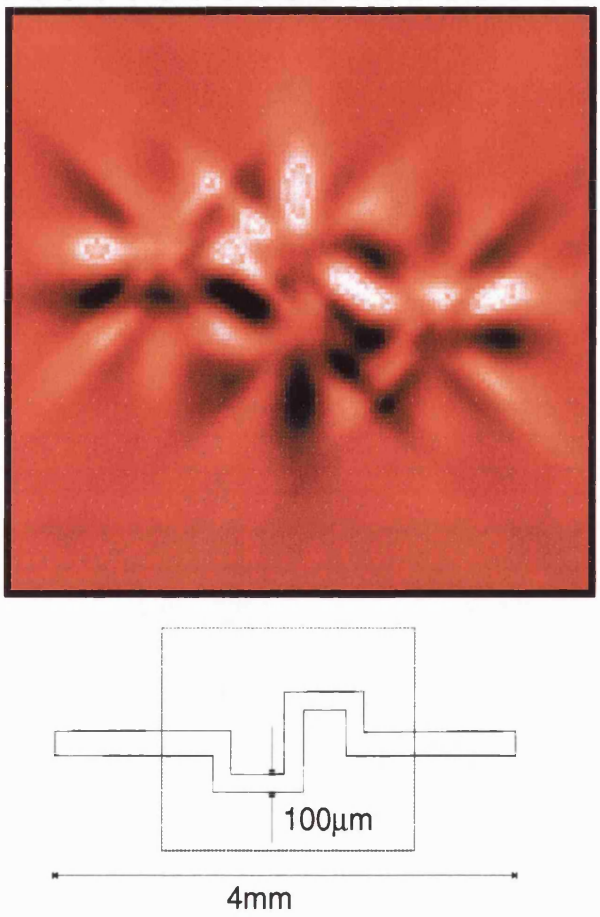

Figure 7.2.11: *Simulated image for the sample geometry E2. The geometry is shown in the lower part of the figure.*

7.3 Effects at the contacts

It is interesting to note that in both the calculations and in the experimental results, a large signal is seen at the region of the contacts: this has not been shown in all the images above, since most of them just depicted the central areas of the image. However, this can be seen in Fig. 7.3.1, which shows the whole calculated area for the sample with no constriction (G2). The geometry has a width of 0.5mm and a length of 4mm, and is shown superimposed onto the image.

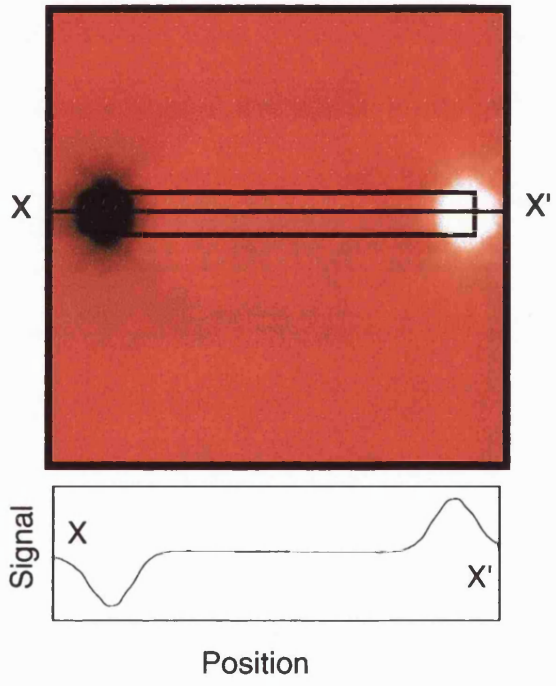

Figure 7.3.1: *Simulated image for sample with no constriction, geometry G2, showing large voltage signals at the contact areas. A line-scan is also shown through the image, from points X-X'.*

This can also be seen in all experimental images as can be seen in Fig. 7.3.2, where a similar sample without constriction (G1) was measured. In previous work, this large signal was described as being due to thermal voltages set up at the contacts [25]. These thermal voltages would arise if the material at the contacts absorbed phonons more easily than the 2DEG, and therefore became warmer. However, the fact

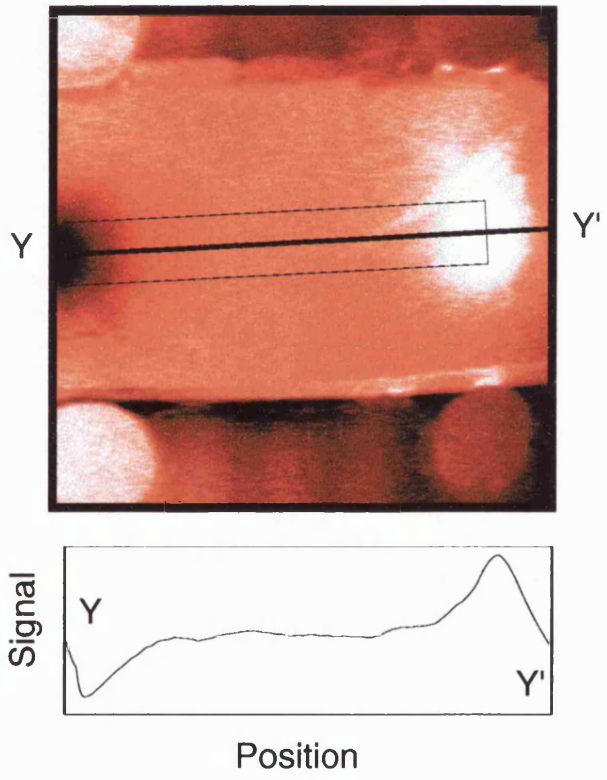

Figure 7.3.2: *Experimental image for sample with no constriction, geometry G1, showing large voltage signals at the contacts. Here a line-scan is also shown, from points Y-Y'.*

that this is also seen in the calculations, where the contacts as such

are not defined but are just given by the ends of the etched structure, shows that this phenonemon is purely due to the phonon-drag effect. This feature occurs for all the measured and simulated samples (see, for example, Fig. 5.3.2). Where the samples also have focussing structure due to changes in the sample geometry, it is possible to compare the relative intensities of the signal at the contacts with that at the focussing structures for both calculated and experimental images, and one sees that the intensity at the contacts is approximately ten times larger than that at the focussing structure, for both experimental and calculated images. This again shows that the phonon-drag effect alone explains these large features at the contacts.

7.4 Conclusions

The excellent agreement between experiment and model, over a wide range of different sample geometries shows the capability of the model to accurately describe the experimental situation. It also shows the simplicity of the whole effect, and that the phonon-drag effect can be invoked to explain all experimental results, when taking into account the finite effects of the sample geometry, and the relevant boundary conditions. The excellent agreement between the simulations and the experimental results also serves to confirm that the assumptions made in the course of the simulation are valid. It is of course possible to extend the simulations to more sample geometries, but the agreement that has so far been demonstrated indicates that the simulation is very accurate in reproducing the experimental data, and that the model used is a very accurate, and simple, description of the phonon-drag effect.

Chapter 8

Conclusions

In this thesis, the interaction between ballistic acoustic phonons and electrons in low-dimensional electronic systems has been studied, by means of the phonon-drag effect. This effect means that phonons which interact with electrons transfer their momentum to the electron system, causing a movement of the electrons, which can be measured as a voltage or a current. Frequency resolved measurements, using superconducting tunnel junctions as generators of quasi-monochromatic acoustic phonons and the two-dimensional electron gas as a detector, have shown the frequency dependence of the phonon absorption by the 2DEG. In agreement with theoretical expectations, the phonon signal rises, until a maximum value is reached, after which the signal decays. The value for this cut-off is given by the phonon frequency which corresponds to the value of $2k_F$, as predicted by theory. However, a reduction in the

phonon absorption due to the form factor, which is also predicted by the theory has not been observed. The reason for this is not clear. In addition, the occurrence of the form of the curve predicted by theory was not very common, the majority of the curves showing a different form, and the reason for this remains unclear, although it is most likely due to cross talk in the measurement circuit.

Spatially resolved measurements showed no frequency dependence, as can be seen by the measurements on the 3D systems, although theoretically a strong frequency dependence is to be expected. A difference in the images is expected, since for the 3D systems the restriction due to the form factor is not applicable. This lack of frequency dependence is assumed to be due to the broad phonon spectrum which is emitted from the excited aluminium film, and which is too broad to resolve frequency effects. Measurements performed at 4.2K also show no obvious differences to those obtained at 1.1K, indicating that the phonon spectrum generated by illuminating a superconducting film is Planckian, and not peaked around the value of the energy gap as had previously been assumed.

Further spatially resolved measurements have shown effects which cannot be explained using a simple theory of phonon focussing which assumes a point phonon source and a point phonon detector. Many images show multiple phonon-focussing structures with origins centred around areas where the sample geometry changes. These images show that the whole detector geometry must be taken into account when try-

ing to explain such images. A theoretical model was therefore developed which solves the phonon-drag effect over the whole detector geometry. The phonon-drag effect is treated as being equivalent to the setting up of a local charge dipole. The effect of this local dipole is then calculated over the total sample geometry. The results obtained show exceptional agreement with the experimental images, for a wide range of sample geometries. This excellent agreement shows the strength of the model in accurately describing the experimental situation. The model could also be used to describe other phonon-drag imaging experiments, for example using hole gases as detectors instead of electron gases. It would be expected that in the case of hole gases the signal would be larger, due to the larger phonon-hole coupling. There could also be some differences in the focussing images obtained if the hole interact more-or-less strongly with certain phonon modes.

The theoretical model also reproduces the large voltage signals at the contact areas of the device which are seen in the experimental images. The fact that these are reproduced in the model shows that the experimental signals which were previously thought to be due to thermal voltages at the contacts, can be completely explained in terms of phonon-drag. Therefore the model provides the first accurate and complete description of the phonon-drag effect between ballistic acoustic phonons and the electrons in low-dimensional electron systems, and is necessary when describing phonon-drag images where the detector is not an ideal point.

Appendix A

In order to follow the process of the theoretical simulations more thoroughly, this appendix will show some of the intermediate results that the simulation produces. In particular the potential distribution over the whole sample geometry for a local charge dipole positioned in certain areas of the sample will be shown. This will aid the understanding of how the final images are formed.

As was described in Section 3, the simulations are performed on finite element grids of 400 $\times$100 grid points. The charge dipole is set at all positions on the grid, and the potential distribution is then calculated by finding solutions to the differential equation given in eqn (3.2.1).

Figures A.0.1 a-d show the situation for a charge dipole located at the points (10,10), (40,50), (100,50), and (200,50) respectively, and

parallel to the x-axis. The situation for dipoles directed parallel to the y-axis can be seen in Fig. A.0.2 a-d. The zero of the coordinates is at the bottom left hand corner of the sample. The geometry of the sample used was 400×100 units, with a 5×5 unit constriction (see Figure 3.1.1). It can be seen that the local charge dipole has an effect over the whole area of the sample, regardless of its position, and it is only the magnitude of the effect that varies, the effect being largest when the dipole is positioned near the ends of the sample, or near the constriction.

Once the response function for a single dipole position has been computed, the voltage difference between the ends of the sample must be calculated. This has been done by taking the average value of the voltage at the left and right ends of the sample, and finding the difference. A slightly better fit to an ohmic contact could be achieved by finding the average potential value at the ends of the sample after each iteration step, and using this as the value of the potential for all points at the ends of the sample for the next iteration step. However, this would considerably increase the computer time, and was therefore not performed.

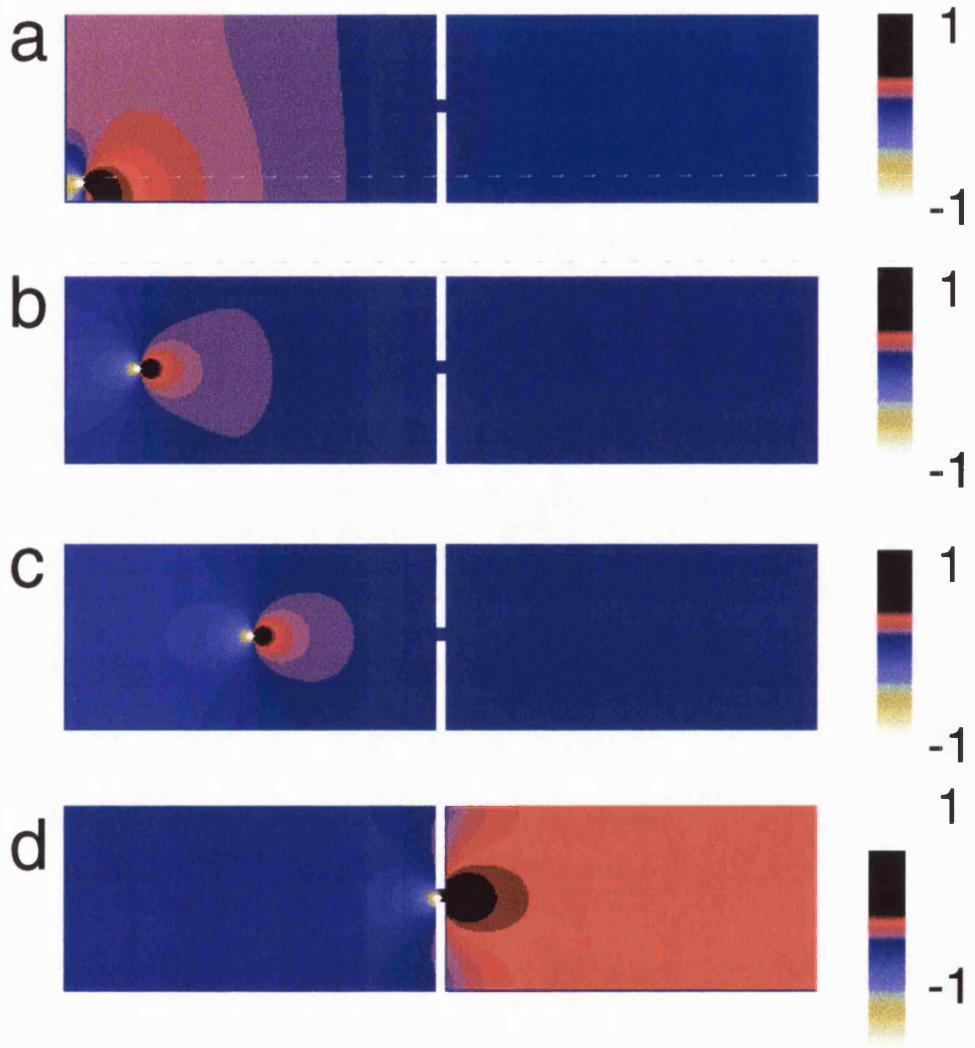

Figure A.0.1: *Potential distributions for single charge dipoles positioned at various points within the sample, and directed parallel to the x-axis. The dipoles are positioned at: a) (10,10), b) (40,50), c) (100,50), d) (200,50). The origin is at the bottom left-hand corner. The sample geometry is 400×100 units with a 5×5 unit constriction in the centre (see Fig. 3.1.1).*

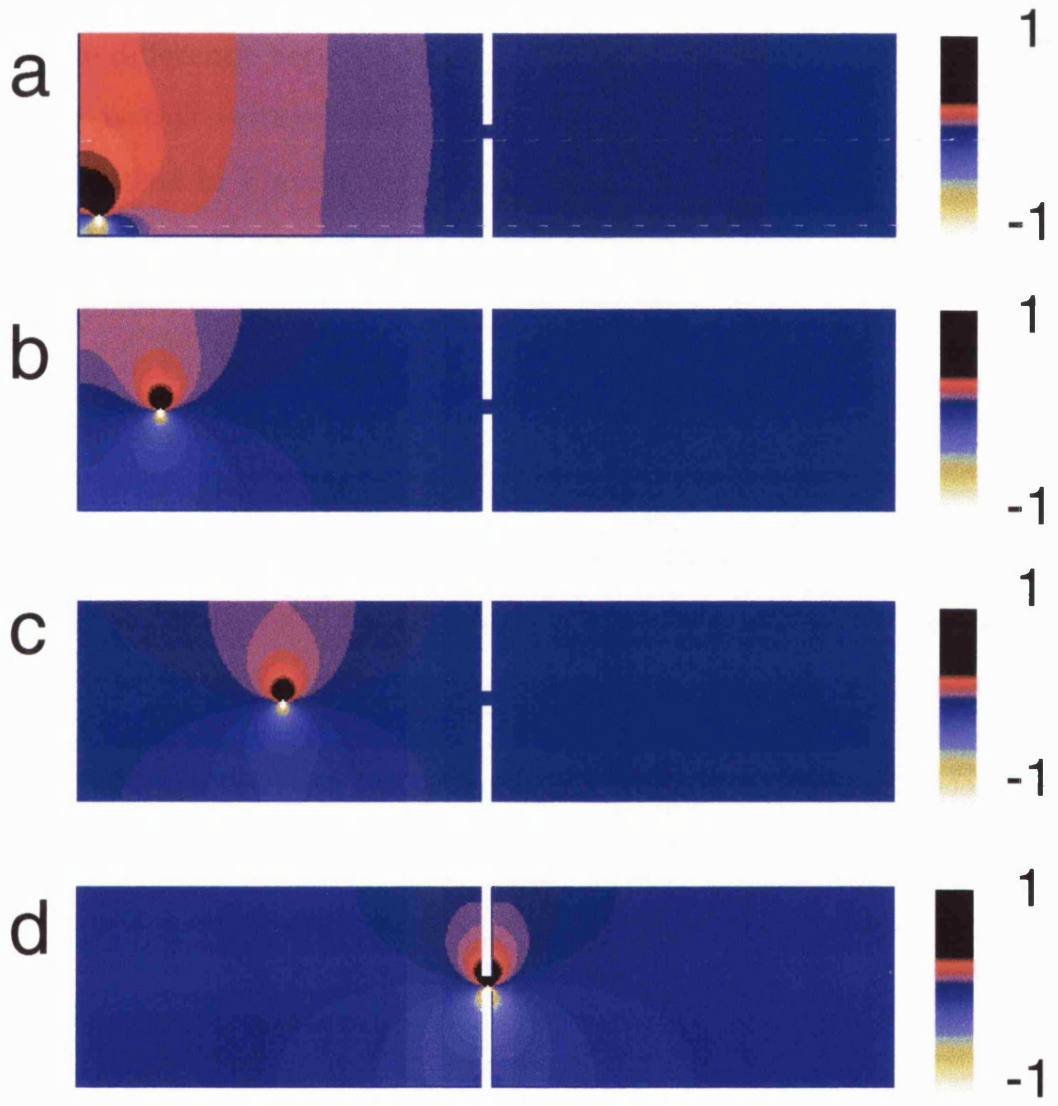

Figure A.0.2: *Potential distributions for single charge dipoles positioned at various points within the sample and directed parallel to the y-axis. The dipoles are positioned as for Figs A.0.1 a-d.*

It can be seen from the images that there is always going to be a voltage difference between the left and right hand edges of the sample, and it is this voltage difference, as a function of position which has been plotted in Figures 7.1.1 and 7.1.2, and which is shown again for ease of comparison in Figure A.0.3 and A.0.4, where the positions of the dipoles are also indicated. This voltage difference as a function of position of the local charge dipole is what was previously referred to as the response function of the system.

Figure A.0.5 shows the potential distribution for a sample

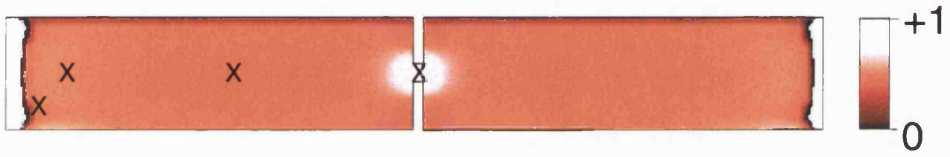

Figure A.0.3: *Response function for dipoles directed parallel to the x-axis.*

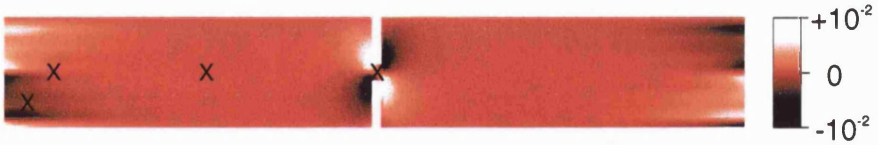

Figure A.0.4: *Response function for dipoles directed parallel to the y-axis.*

without a constriction (equivalent to the sample geometry shown in Fig. 7.3.1), where the dipole is positioned at the position (200,100).

Figure A.0.5a shows the case for the dipole parallel to the x-axis, and Fig.A.0.5b for the dipole parallel to the y-axis. Comparison of these two images with those for the sample with the constriction (Figs.A.0.1d and A.0.2d) illustrate the effect of the constriction on the signal produced.

Figure A.0.6 shows the image for the dipole set at the point

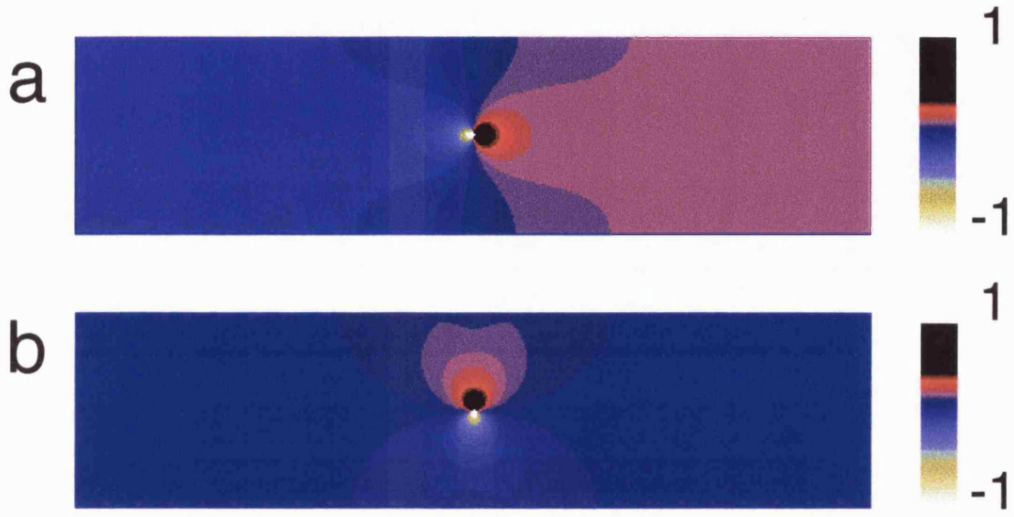

Figure A.0.5: *a) and b): Potential distributions for single charge dipoles positioned at (200,50), for the x- and y- directions respectively. The origin is at the bottom left-hand corner. The sample geometry is 400×100 units with no constriction (see Fig. 7.3.1).*

(100,50) but where the grid spacing has been halved. It can be seen that this shows no differences to the image shown in Fig. A.0.1c, and this therefore indicates that grid spacing used is sufficient to give accurate results.

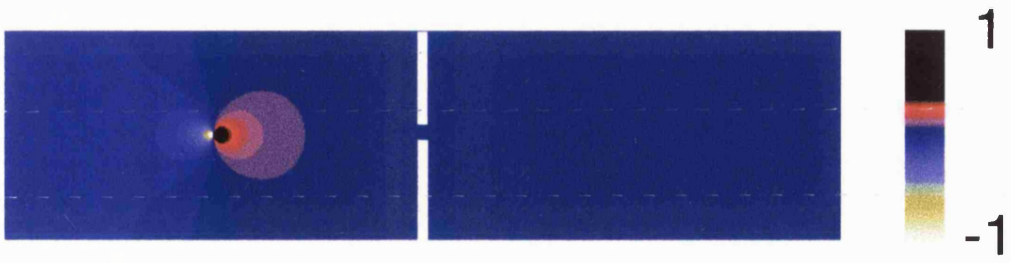

Figure A.0.6: *Potential distributions for a single charge dipole positioned (100,50), but where the grid spacing has been halved with respect to that for Fig. A.0.1d.*

Appendix B

The normal state tunnel junction (NSTJ) as a quasi-monochromatic phonon source.

In this section the situation for tunnel junctions consisting of normal metals instead of superconductors will be described. The idea of producing quasi-monochromatic phonons from normal state tunnel junctions (NSTJ) is not new [52], but until recently had not been realised experimentally. This is probably because there are a number of technological difficulties which need to be overcome. The main advantage that the NSJT has over the SCJT is that it can be used in high magnetic fields, whereas the SCTJ is limited to fields smaller than the critical field for the superconductor, H_c.

The energy density of states for a NSTJ is shown in Figure B.0.1. As can be seen, this differs from the superconducting case (shown in Fig. 2.4.2a), in that there is no energy gap, and also no singularity at

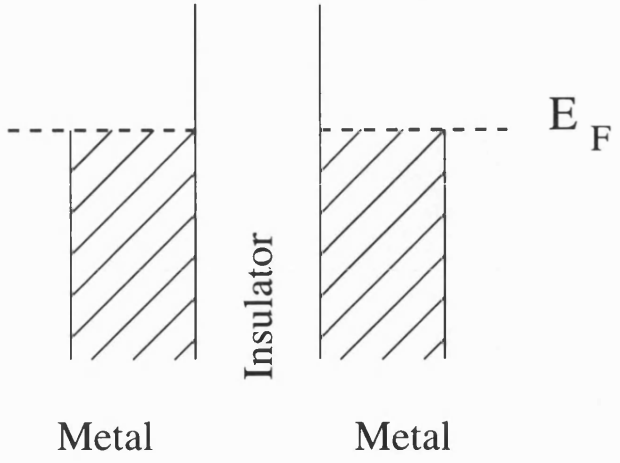

Figure B.0.1: *Energy density of states for the normal state tunnel junction.*

the Fermi surface. This leads to the phonon spectra shown in Figure B.0.2 i) (here shown for three different bias voltages). These phonon spectra do not show a sharp cut-off at $eV_0 - 2\Delta$, but instead exhibit a broad band of phonons which goes continuously to zero at the bias energy. However, when the first and second differentials of these spectra with respect to bias voltage are considered, (see Figure B.0.2 ii) and iii)), a quasi-monochromatic peak in the second differential can be seen at the frequency corresponding to the bias voltage. The quasi-monochromaticity of NSTJ has been observed in experiments using the stress-tuned splitting of boron acceptors in silicon [53]. It has also been further applied to spectroscopic measurements of 2DEGs in high magnetic fields [54]. Recent experiments have also indicated that the experimental frequency spectrum obtained is quasi-monochromatic in the

first differential, contrary to the theoretical expectations [55]. It has been tentatively suggested that this may be due to Fermi-edge singularities and an increase in tunnelling of electrons at the Fermi edge, but as yet this has not been adequately explained.

The main technological problems that needed to be overcome in

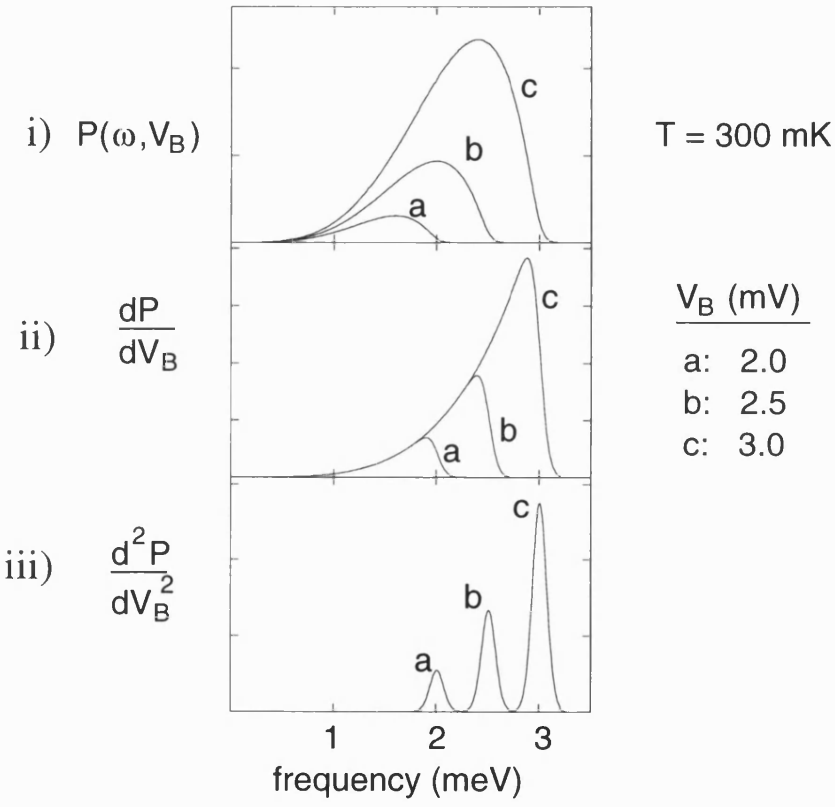

Figure B.0.2: *i) Phonon spectrum from a NSTJ. ii) and iii): first and second differentials respectively of the phonon spectra from a NSTJ, showing a quasi-monochromatic peak in the second differential with respect to bias voltage at the energy value corresponding to the bias voltage.*

these experiments were the effects of thermal emission from the films

themselves and the precise determination of the voltage drop across the films. Since the films are no longer superconducting, they have a finite resistance, which will be important. Due to ohmic heating in the films, there will be emission of thermal phonons from the metal films as well as from the junction. In the experiments performed, the detector was placed directly opposite the emitter, because the focussing is strongest in this direction, and this means that the phonons detected originate to a very large extent only from the overlap of the films, i.e. the junction area. The finite resistance also affects the determination of the applied bias, since in order to measure the potential drop due to tunneling across the junction alone, it is necessary to utilise a four point geometry. Due to the finite film resistance, there is also going to be some non-uniformity of the potential drop across the films. This is given by

$$\Delta V_B \sim \cosh\left(\sqrt{2\frac{R_f}{R_j}}X\right) \tag{B.0.1}$$

where ΔV_B is the variation in the bias voltage, and X is the position. R_f is the film resistance, and R_j is the junction (tunnelling) resistance, and typically these have values of $R_f = 0.3\Omega_\square$ and $R_j = 2\Omega_\square$ [55]. Substituting for these values of R_f and R_j, gives the curve shown in Fig. B.0.3. Here it can be seen that the variation of voltage drop over the junction area is of the order of 10% for the values of resistance assumed. This effect limits the frequency resolution of the tunnel junctions.

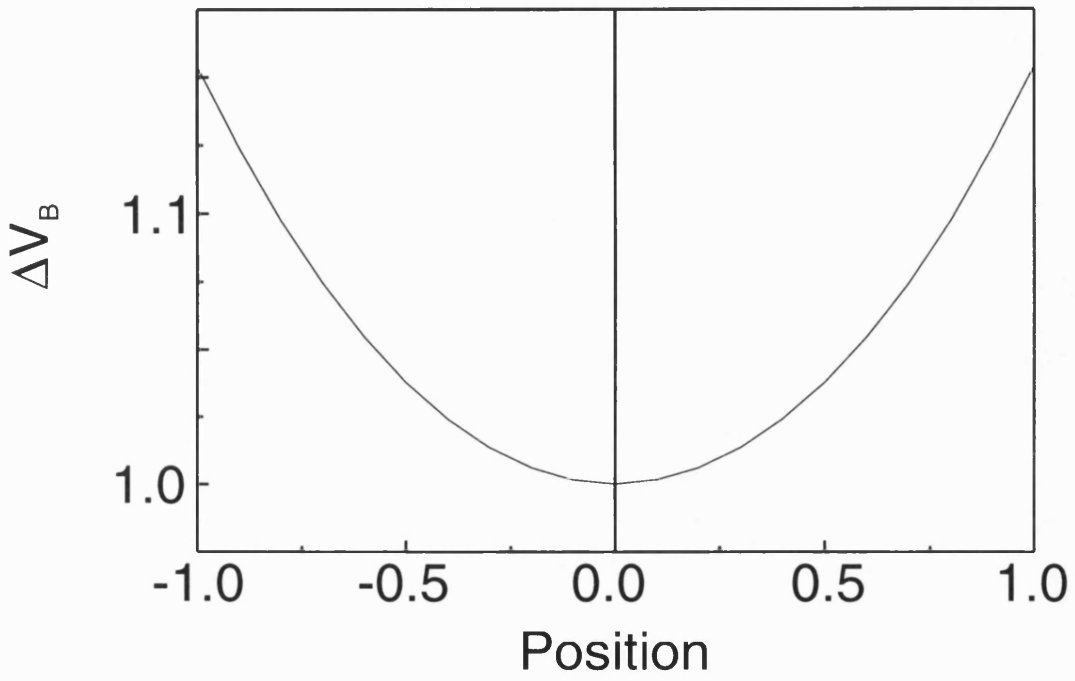

Figure B.0.3: *Variation of the applied bias across the area of the tunnel junction due to the finite film resistance, according to the formula B.0.1.* $R_f = 0.3\Omega_\square$ *and* $R_j = 2\Omega_\square$.

Bibliography

[1] J. P. Eisenstein, A. C. Gossard and V. Narayanamurti: Phys. Rev. Lett. **59**, 1341 (1987).

[2] R. J. von Gutfeld and A .N. Nethercot: Phys. Rev. Lett. **12**, 641 (1964).

[3] W. Eisenmenger and A. H. Dayem: Phys. Rev. Lett. **18**, 125 (1967).

[4] B. Taylor, H. J. Maris and C. Elbaum: Phys. Rev. Lett. **23**, 416 (1969).

[5] J. C. Hensel and R. C. Dynes: Phys. Rev. Lett. **43**, 1033 (1979).

[6] G. A. Northrop and J. P. Wolfe: Phys. Rev. Lett. **43**, 1424 (1979).

[7] W. Eisenmenger, in 'Phonon Scattering in Condensed Matter' Ed. H. J. Maris, (Plenum, New York 1980), p. 303.

[8] W. Dietsche, G. A. Northrop and J. P. Wolfe: Phys. Rev. Lett. **47**, 660 (1981).

[9] H. Karl, W. Dietsche, A. Fischer, K. Ploog: Phys. Rev. Lett **61**, 2360 (1988).

[10] A. Lega, H. Karl, W. Dietsche, A. Fischer, K. Ploog: Surf. Sci. **229**, 116 (1990).

[11] T. Ando, A. Fowler, F. Stern: Rev. Mod. Phys. **54**, 437 (1982).

[12] R. Dingle, H. L. Störmer, A. C. Gossard, W. Wiegmann: App. Phys. Lett. **33**, 665 (1978).

[13] L. N. Pfeiffer, K. W. West, H. L. Störmer, K. Baldwin: Appl. Phys. Lett. **55**, 1888 (1989).

[14] J. L. T. Waugh, G. Dolling: Phys. Rev. **132**, 2410 (1963).

[15] S. Tamura: Phys. Rev. B.**30**, 849 (1984).

[16] S. Tamura: Phys. Rev. B. **31**, 2574 (1985).

[17] E. F. Christoffel: Ann. Mat. Pura. Appl. **8**, 193 (1877) (cited from M. J. P. Musgrave: Crystal Acoustics (Holden-Day, San Francisco, 1970))

[18] P. L. Kapitza: J. Phys. (USSR) **4**, 181 (1941),(cited from [19]).

[19] W. A. Little: Can. J. Phys. **37**, 334 (1959).

[20] D. Marx, W. Eisenmenger: Z. Phys. B - Condensed Matter **48**, 227 (1982).

[21] J. Weber, W. Sandmann, W. Dietsche, H. Kinder: Phys. Rev. Lett. **40**, 1469 (1978).

[22] A. G. Every, G. L. Koos, J. P. Wolfe: Phys. Rev. **B** 29, 2190 (1984).

[23] O. Weis: Z. für Angew. Phys. **26**, 325, (1969).

[24] F. Rösch, O. Weis: Z. für Phys. B **27**, 33 (1977).

[25] F-H. Dietzel: Ph.D Thesis. Univ. of Stuttgart. (1992).

[26] J. Cooper, S. Roshko, W. Dietsche, Y. Kershaw, U. Wenschuh: Phys. Rev. B. **50**, 8352 (1994).

[27] H. Kinder: Phys. Rev. Lett., **28**, 1564 (1972).

[28] F. F. Fang and W. E. Howard: Phys. Rev. Lett. **16**, 797 (1966).

[29] J. C. Hensel, R. C. Dynes, D. C. Tsui: Phys. Rev B. **28**, 1124 (1983).

[30] H. P. R. Frederikse: Phys. Rev. **92**, 248 (1953).

[31] L. E. Gurevich, O. L. Mashkevich: Physics Reports **181**, 327 (1989).

[32] Cz. Jasiukiewicz, D. Lehmann, T. Paszkiewicz: Z. Phys. B - Condensed Matter **86**, 225 (1992).

[33] Y. M. Kershaw, S. J. Bending, W. Dietsche, K. Eberl: to be published.

[34] R. W. Rendell, S. M. Girvin: Phys. Rev. B **23**, 6610 (1981).

[35] R. Wichard: private communication.

[36] A. Y. Cho, J. R. Arthur: Prog. Solid State Chem. **10**, 157, (1975)

[37] K. Ploog: Angew. Chemie. **100**, 611 (1988) and references therein.

[38] B. A. Joyce: Rep. Prog. Phys. **48**, 1637 (1985) and references therein.

[39] F. Dietzel, W. Dietsche, K. Ploog: Physica B **165 & 166**, 877 (1990).

[40] F. Dietzel, W. Dietsche, K. Ploog: Phys. Rev. B. **48**, 4713 (1993).

[41] M. Otsubo, T. Oda, H. Kumabe, H. Miki: J. Electrochem. Soc. **123**, 676 (1976).

[42] G. A. Northrop and J. P. Wolfe: Phys. Rev. B. **22**, 6196 (1980).

[43] G. A. Northrop and J. P. Wolfe: Nonequilibrium Phonon Dynamics, ed W. E. Bron, 165 (1984).

[44] A. R. Hutson, J. H. McFee, D. L. White: Phys. Rev. Lett. **7**, 237 (1961).

[45] V. Narayanamurti, R. C. Dynes: Phys. Rev. Lett **27**, 410 (1971).

[46] B. A. Danilchenko, V. N. Poroshin, M. I. Slutskii, M. Asche: Phys. Stat. Sol. (b) **136**, 63 (1986).

[47] C. K. Campbell, R. C. Dynes, D. G. Walmsley: Can. J. Phys. **44**, 2601 (1966).

[48] U. Wiesner: private communication.

[49] W. Eisenmenger, K. Laßmann, H. J. Trumpp, R. Krauß: Appl. Phys. **12**, 163 (1977).

[50] H. J. Trumpp, W. Eisenmenger: Z. Phys. B **28**, 159 (1977).

[51] P. Berberich, M. Schwarte: Z. Phys. B - Condensed Matter **64**, 1 (1986).

[52] W. Eisenmenger, in 'Physical Acoustics' XII, edited by W. P. Mason and R. N. Thurston (Academic Press, New York, 1976), p. 79.

[53] S. Roshko, W. Dietsche: Solid State Comm. (to be published).

[54] S. Roshko, V. Zhitormirsky, J. Cooper, U. Wiesner, W. Dietsche, K. Eberl : Physica B (to be published).

[55] S. Roshko, U. Wiesner : private communication.

Acknowledgements

This work was carried out at the Max-Planck-Institut für Festkörperforschung (solid state research) in Stuttgart, Germany. I am indebted to various bodies for financial support throughout my PhD: sincere thanks in this respect go to:.

Harold Hyam Wingate Foundation

Deutsche Akademisches Austauschdienst (DAAD)

European Union Human Capital and Mobility Programme

Leverhulme Trust

I would like to express my sincere thanks to all those who have helped me in any way with this work. Particular thanks go to:

Prof. Dr. W. Dietsche, for excellent supervision throughout the duration of this work.

Dr. Simon Bending for providing the other half of the supervision at the other end of the e-mail, along with plenty of advice and encouragement, and the initial ideas for the theoretical model.

Prof. K. von Klitzing for giving me the opportunity to work within his department, and to use the facilities within the Institute.

Special thanks go to Sergej, for all his words of wisdom and encouragement during the time we spent together in the office.

Gerd for his assistance with various problems, and for company on numerous occasions in the pizzeria, as well as on the badminton court.

Rolf Menne for trying to enlighten me in the art of programming, and

for finding some of those small mistakes which are always so difficult to spot.

Ulle for his help on numerous occasions, as well as for trying to be a worthy opponent on the badminton court.

Frank Dietzel for a critical reading of the manuscript.

Ralf Wichard for developing the scanning software.

John Cooper for his assistance in the first year of my PhD.

Monika Riek for so much prompt sample processing.

Karl Eberl and the MBE group for providing the MBE samples

Frau Bauser and the liquid-phase epitaxy group for providing the LPE samples.

Frank Schartner for numerous masks, and for bonding some samples.

Werner Rauscher for technical assistance in the lab.

Herr Wendel and other members of the crystal preparation group for polishing numerous samples and preparing the ceramic sample holders.

The TTS (low temperature service) for their friendly and prompt supply of liquid helium and nitrogen.

Geoff Nash and Jürgen Müller for their support and encouragement per email from Bath.

I would also like to thank all the past and present members of the department and institute with whom I have had the pleasure of working and socialising during my time in Germany, especially (in random order):

Ulrike Waizmann, Dietrich Bertram, Gabi Ernst, Markus Dilger, Daniela

Pfannkuche, Elisabeth Vasiliadou, Ulrich Wenschuh, Holger Rubel, Claudia Lange, Andy Peck, Nick Pulsford, Martyn Chamberlain and anyone else who I've forgotten.

A special note of thanks to Herbert for all his help, advice, and encouragement.

Finally my thanks go my parents and family, for all their support and encouragement throughout my education.